ANALYSIS OF HIGH FIELD Q-SLOPE (HFQS) CAUSES AND DEVELOPMENT OF NEW CHEMICAL POLISHING ACID FOR NIOBIUM SRF CAVITIES

By

Didi Luo

A DISSERTATION

Submitted to
Michigan State University
in partial fulfillment of the requirements
for the degree of

Physics – Doctor of Philosophy

2020

ABSTRACT

ANALYSIS OF HIGH FIELD Q-SLOPE (HFQS) CAUSES AND DEVELOPMENT OF NEW CHEMICAL POLISHING ACID FOR NIOBIUM SRF CAVITIES

By

Didi Luo

Buffered Chemical Polishing (BCP) was the most conventional polishing method for superconducting radiofrequency (SRF) Niobium (Nb) cavity surface preparation before the discovery of Electropolishing (EP), which is superior to BCP in high gradient performance. The High Field Q-slope (HFQS) is entirely eliminated by taking the low-temperature bake (LTB) post EP, which guarantees high gradient performance in EP'ed cavities. The mechanism of the HFQS is well understood for EP'ed cavities. On the other hand, there is no common consensus on the HFQS with BCP, since even BCP with LTB does not always resolve the HFQS. BCP is much easier to apply and still a vital preparation technology for very complicated SRF structures like low beta cavities. Therefore, overcoming the issue of HFQS with BCP is highly beneficial to the SRF community. This thesis mines a large number of available data sets on BCP'ed cavity performance with fine grain, large grain, and even single-crystal niobium materials under different experimental settings.

We found that all existing explanations for HFQS with BCP are inconsistent with some experimental results, and propounded nitrogen contamination as a new model to explain the result. Our conclusion is made based on previously unresolved phenomena which include (1) applying multiple BCP post EP; the maximum gradient does not always agree with roughness; (2) cavity treated with EP acid adding a drop of HNO_3 started to have non-resolvable HFQS; (3) maximum field of BCP single-crystal cavities are lower than EP large grain cavities; (4) temperature map shows no high roughness area heating for a large-grain BCP cavity. We then checked that nitrogen contamination agrees with all existing data and nicely explains unresolved phenomena.

According to this result, we have started developing a new nitrogen-free chemical polishing acid. H_2O_2 with HF mixture was reported able to react with Nb, and there is no extra element contamination in it, so we replace the conventional BCP with this mixture to start our study.

We discovered that this new acid could not provide sufficient smooth finishing surface, even after we adjusted all the parameters. However, adding a copper catalyst allows this acid to provide a smooth surface similar to or even better than conventional BCP. The copper remnant can be neglected according to an EDS study on the Nb surface. We studied the reaction mechanism and deduced that several other metals that can be promising as catalysts. One of those is iron, which was later shown to have the catalyst effect; this proved the mechanism we found is right.

Further study can focus on other potential catalysts (such as Pb and Sn) and testing cavities treated by these acids. Pb is superconducting under operation temperature, may reduce potential harm to cavity performance, and Sn may react with Nb and generate Nb_3Sn on its surface, which is another promising material for SRF cavities. These studies will offer more possibilities for SRF material.

To my family

ACKNOWLEDGEMENTS

First of all, I would like to express my sincere gratitude to my advisor Prof. Kenji Saito for the continuous support of my Ph.D study and related research, for his enthusiasm, motivation, and immense knowledge. His guidance helped me in all the time of research and writing of this thesis.

Besides my advisor, I would like to thank the rest of my thesis committee: Prof. Steven Lund, Prof. Johannes Pollanen, Prof. Jie Wei, and Prof. Yoshishige Yamazaki, for their insightful comments and encouragement, but also for the questions which incented me to widen my research from various perspectives.

My sincere thanks also goes to Ting Xu, Laura Popielarski, John Popielarski, Chris Compton in FRIB and Reza Loloee in Department of Physics and Astronomy for who provided me opportunities to take related training, and who gave access to the laboratory and research facilities. Without their precious support it would not be possible to conduct this research.

I would also like to thank Ethan Metzgar and George Simpson in FRIB for the help during my Nb chemical etching experiments; Walter Hartung, Sang-hoon Kim, Mengxin Xu, Cong Zhang, Zhihong (Winter) Zheng in FRIB for the training and help during cavity vertical tests and solenoid tests; Tasha Summers for the tutorial and help of CS-studio scan-file developing; Baokang Bi in Keck Microfabrication Facility of the MSU Department of Physics and Astronomy for the training of facilities; Xudong Fan in MSU Center For Advanced Microscopy for the Transmission Electron Microscopy (TEM) training and services. I also thank US Particle Accelerator School for the invaluable learning opportunities and social interactions that have been immensely beneficial to my thesis research and my growth in the field of accelerator science.

I thank Daniel Alt, Michael Balcewicz, Crispin Contreras, Robert Hipple, Bryan Isherwood, Andrew LaJoie, Kellen McGee, Derek Neben, Christopher Richard, Safwan Shanab, and Chun Yan Jonathan Wong for their questions and feedback during the discussion of our regular meeting consists of MSU graduate students in accelerator physics. I am also grateful to Jian Gao, Yue Hao, Alfonse Pham, Haitao Ren and Qiang Zhao who provided their astute comments and career advice.

I appreciate the assistance from Kim Crosslan at the Department of Physics and Astronomy that allowed me to meander through all kinds of paperwork unscathed.

Last but not the least, I would like to thank my family and all my friends for supporting me spiritually throughout writing this thesis and my life in general.

TABLE OF CONTENTS

LIST OF TABLES

LIST OF FIGURES

CHAPTER 1

INTRODUCTION

This chapter overviews particle accelerators' history and applications, introduces superconducting RF (SRF) accelerator facilities, and then the Facility for Rare Isotope Beams (FRIB) at Michigan State University. There is no difference in the principle of beam acceleration between superconducting RF accelerators and normal conducting ones. However, it will be essential to show the electrodynamics to understand the beam acceleration principle. At first, electromagnetics related to RF cavity design will be described, then superconductivity theory and its application to the accelerator will be reviewed. At the end of this chapter, design strategy, fabrication and processing will be introduced.

1.1 Particle Accelerators

1.1.1 History and Application of Accelerators

It has been 100 years since E. Rutherford first succeeded to collide alpha particles with a 0.0004 cm metal foil target [1]. At that time particle accelerator was not yet developed, he used a natural radiating source for this a breakthrough in nuclear science in 1919. He discovered the atom nucleus structure (Rutherford model) by analyzing the diffraction pattern made on a Zinc sulfide fluorescent screen placed behind the target. This inspired nuclear scientists to achieve particles with higher energy to work as "bullet".

In 1932, J. D. Cockcroft and E. T. Walton invented the first DC accelerator to more precisely probe the nuclear: the Cockcroft-Walton Accelerator [2]. The high DC voltage to accelerate charged particles is generated from low voltage AC or a pulsing DC input. The generator is made out of a voltage multiplier ladder network from capacitors and diodes. They succeeded in creating the first artificial nuclear disintegration in history using their accelerator. In 1951, they were awarded the Nobel Prize in Physics for "Transmutation of atomic nuclei by artificially accelerated atomic particles".

In the year of 1933, R. J. Van de Graaff invented a DC accelerator powered by another kind of high voltage generator: Van de Graaff generator [3]. This generator is using the triboelectric effect and accumulates charges by using an insulated belt to transfer electrons onto one metal comb connected with a metal sphere and another metal comb grounded.

The breakdown voltage limits both DC accelerators (the Cockcroft-Walton Accelerator and the Van de Graff DC accelerator), and particles' final energy is at most $\sim$ 10 MeV [4].

By applying a high-frequency voltage to drift tubes, G. Ising in 1924 [5], and E. Wideroe in 1928 [6] independently invented another linear accelerator. This RF approach allows bypass of breakdown voltage limits. Due to the limitations of high-frequency technology at that time, such accelerators could only accelerate potassium ions to 50 keV energy, which was of little practical significance. However, inspired by this principle, E. O. Lawrence invented the cyclotron in 1932 [7] and used it for artificial radioisotope productions. For this achievement, he won the Nobel Prize in physics in 1939.

Due to the restriction of the mass and energy of the accelerated particles, a conventional cyclotron can only accelerate the protons to about 25 MeV. However, if the intensity of the accelerator's magnetic field is designed to increase synchronously along the radius with the particle energy, it can accelerate the protons to hundreds of MeV. Such a machine is called isochronous cyclotron.

The angular frequency the particle $\omega = qB/m$ in a cyclotron depends on the particle mass, which has relativistic effect that $m_{rel} = m_{rest}/\sqrt{1 - v^2/c^2}$. When the velocity of the particle approaching the speed of light, the mass increases and seriously changes the angular frequency, to deviate from the original cyclotron frequency. This causes the particle to get progressively more out of step with the accelerating voltage as its speed increases. This problem is solved in the synchrocyclotron by varying the frequency of the accelerating voltage to track the relativistic effects (increase in effective mass with energy).

In order to further explore the structure of the nucleus and generate new elementary particles, it is necessary to study the principle of building higher energy particle accelerators. In 1945,

Figure 1.1: Phase stability schematic: point S is the ideal case. point E arrives early, experiences a smaller field; point L arrives later, experiences a larger field than S; point U is too far from point S and is in the unstable phase.[10]

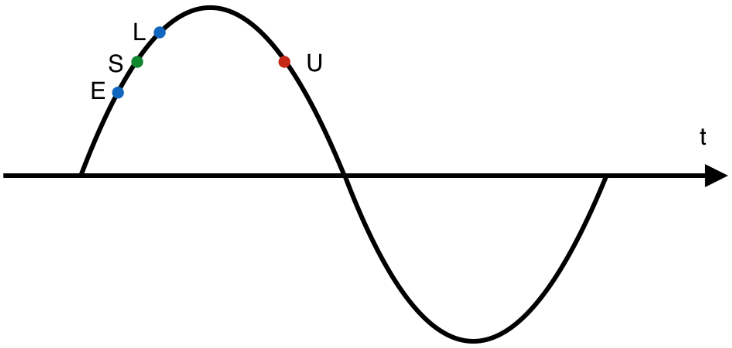

scientists V. I. Veksler of the former Soviet Union [8] and E. M. Mcmillan of the United States [9] independently discovered the principle of automatic phase stabilization.

The principle of automatic phase stabilization, or Phase Stability, refers to in some resonance accelerators, the motion of ideal particles (stable phase, point S in Fig. 1.1) accelerated in a specific equilibrium phase can be completely synchronized with the high-frequency RF electric field, and the energy will continuously increase. In contrast, the non-ideal particles which deviate from the ideal particles in a specific range of phase and energy (stable phase, point E and point L in Fig. 1.1) will have stable phase oscillation around the ideal particles. Then a spread of particles are accelerated together tracking the ideal energy case to their final energy on target. Point U is in the unstable phase, the distance between it and the point S will increase during the acceleration process, and it eventually get lost.

The discovery of phase stability detection is a significant revolution in the history of the development of accelerator; it led a series of breakthrough to the new high energy accelerators:

- Synchrocyclotron which decreases the RF frequency of the electric field according to the increased particle energy, and keeps the synchronization between RF frequency and particle energy.

- Synchrotron which is a kind of circular accelerator; by controlling the frequency of the magnetic field and the accelerating electric field in accordance with the acceleration of the particles, acceleration is performed while keeping the orbital radius of the accelerating particles constant.

- Modern proton LINAC and other accelerators.

These strategies also give more efficient focus strength per field onset.

Since then, accelerators have been built to address the theoretical limitations, but increasing the electric power and the bending and focusing strength has been economically limited. With the increase in accelerating energy, the weight and cost of the magnets used in cyclotrons and synchrotrons rose sharply, and the accelerating energy was limited to less than 1 GeV. For example, the size of the vacuum aperture in the Synchrotron ring must be large due to the poor transverse focusing force. As a result, the magnetic pole gap of the magnet is large, which still requires a very heavy and large magnet. It would be impossible to use such huge magnets to accelerate protons above 10 GeV (the magnet used in the 10-GeV proton synchrotron of the USSR Academy of Sciences has a mass of 36,000 t [11, 12]).

In particle accelerators, when charged particles pass through a uniform magnetic field, due to the Lorentz force, weak focusing will appear in the particle accelerator. Due to circular motion, the orbits of two particles with slightly different positions may approximate or even cross each other. Due to divergence, a beam of particles with a position change will focus in a magnetic field. Each rotating beam is focused on one spot rather than one point, and it only intersects once per revolution. This oscillations in accelerators were theoretically studied by D. W. Kerst and R. Serber for the first time in electronic induction accelerator (also called betatron) in 1940 [13].

In 1952, E. D. Courant, M. S. Livingston and H. S. Schneider published a paper on the principle of strong focusing (or alternating gradient focusing)[14], according to which the construction of a strong focusing accelerator can significantly reduce the size of the vacuum aperture and the cost of the magnets, making it possible for the accelerator to achieve higher energy. This is another revolution in the history of accelerators. Since then, the principle of strong focusing has been widely used in a ring and linear accelerators.

In contrast with weak focusing's uniform magnetic field, strong focusing refers to the principle that when the net effect of alternating electric field gradient acting on a bundle of charged particles, both the vertical and horizontal focusing of protons could be made strong at the same time, by correlation of orbit with kicks provided. This allows tight control of proton paths in the machine and increases beam intensity while reducing the overall construction cost of a more powerful accelerator. For comparison, a 6.2 GeV weakly focused proton synchrotron with a total magnet weight of 10,000 tons was built at Lawrence national laboratory in 1954. While, Brookhaven national laboratory's 33 GeV strong-focused proton synchrotron has a total weight of just 4,000 tons. This illustrates the tremendous practical significance of the principle of strong focusing [12].

For relativistic particles accelerating in a straight orbit, radiation of particles is not a severe effect since their speed increase is minimal as they gain further energy and approach c. However, particles in a circular orbit experience an acceleration that increases as they acquire high kinetic energies. In a circular accelerator that keeps the particle at constant radius, the energy lost of a relativistic electron to synchrotron radiation per turn is

$$U_0 = \frac{4\pi r_e}{3(m_0c^2)^3} \cdot \frac{E^4}{\rho} = \frac{e^2}{3\varepsilon_0} \cdot \frac{\gamma^4}{\rho}, \tag{1.1}$$

where $\gamma = E/(m_0c^2)$, ρ is the radius of the circular accelerator, ε_0 is the permittivity of free space and

$$r_e = \frac{1}{4\pi\varepsilon_0}\frac{e^2}{m_ec^2}, \tag{1.2}$$

in Eq. 1.1 is the classical electron radius [15]. Note that since $\gamma = E/(m_0c^2)$, electrons lose energy about 10^{13} times faster than protons. This is one main reason of the strategy that LHC protons are travelling not electrons, and most electron accelerators are LINACs. Practically, synchrotron radiation is emitted in a well-defined narrow radiation cone with an aperture angle inversely proportional to γ.

Furthermore, under certain conditions, synchrotron radiation can be produced coherent. Such devices are known as free-electron lasers (FEL) that until recently have existed as the only useful sources of coherent far-infrared and THz radiation. FELs are becoming increasingly appealing as sources for coherent x-ray radiation, two examples are the x-ray FEL at DESY [16] and the Linac Coherent Light Source (LCLS) at SLAC [17].

The ultra-high energy also dramatically increases the magnetic field strength demand of the bending magnet, which promotes the research and application of superconducting magnets. They can generate magnetic fields that are up to ten times stronger than those generated by ordinary ferromagnetic-core electromagnets, which are limited to fields of around 2 T to avoid saturation. The field of an SC magnet is generally more stable, and can be smaller, since they do not need a large yoke. Most importantly, for large magnets, they can consume much less power. One of the most challenging uses of SC magnets is in the LHC particle accelerator. The niobium-titanium (Nb-Ti) magnets safely operate at 1.9 K at 8.3 T [12].

Electron synchrotrons use electromagnetic fields to provide the acceleration energy, allowing for even more significant radiation losses, with a limit of about 10 GeV. Electron linear accelerators, use electromagnetic fields to accelerate electrons to higher energies with limits being largely economically driven.

Increasing the acceleration energy to such a level exposes new problems from an experimental point of view. In nuclear and early high energy physics experiments, accelerators are generally used to bombard the nuclei in the stationary target with accelerated particles, and then the momentum, direction, charge and quantity of the secondary particles generated are studied. The actual useful energy of the accelerated particles to participate in high energy reactions is limited. If two charged particles with the identical mass collide each other, the accelerated particle energy can be fully used for high-energy reactions or the generation of new particles. The principle was first proposed by an Italian scientist, B. Taouschek in 1960, and the ADA collider with a diameter of about 1 meter was built at Italy's Frascati national laboratory to verify the principle. Their success has opened a new era in accelerator development. Modern high-energy accelerators are basically in the form of colliders. The collider has been able to increase the equivalent energy of high-energy reactions from 1 TeV to 10-1000 TeV, which is another fundamental leap in the development history

Figure 1.2: Example of LHC design, here k = 2808, $N_1 = N_2 = N = 1.15 \times 10^{11}$, f = 11.25 kHz, A = $\pi\sigma_x^*\sigma_y^*$, $\sigma_{x,y}^*$ = 16.7 μm, and peak luminosity per IP is 1×10^{34} cm^{-2}s^{-1}.[18]

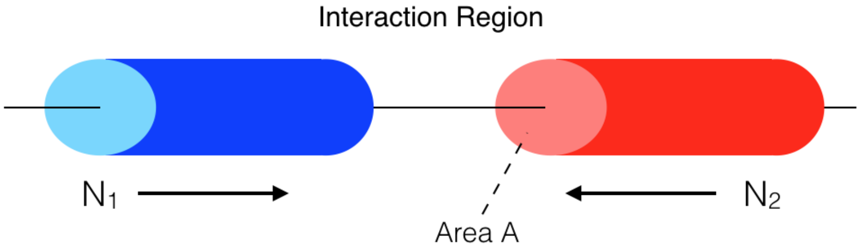

of accelerator energy [12].

The important figure of merit of the accelerator parameter of the collider is the Luminosity (L), which is defined as follows:

$$Y = L\sigma. \tag{1.3}$$

Here, Y is the event rate, σ is a cross-section of a physical l process, and L is the Luminosity of the collider. Higher L can produce a higher yield of phycics events. The Luminosity is given by

$$L = \frac{kN^2 f}{4\pi\sigma_x^*\sigma_y^*} = \frac{kN^2 f\gamma}{4\pi\beta^*\varepsilon}. \tag{1.4}$$

Here k is the number of bunches, N is the number of protons per bunch, f is the revolution frequency, and σ_x^* and σ_y^* are the rms beam sizes at the collision point. An example of LHC design value is shown in Fig. 1.2.

In the 90 years since the world's first accelerators were built, their energy has increased by roughly nine orders of magnitude as shown in the Livingston Plot [19] (see Fig. 1.3, plot stops 2010), while the cost per unit of energy has fallen by about four orders of magnitude. Another breakthrough of the accelerator technology is the application of the SRF technology [20], first succeeded in the TRISTAN accelerator in 1989. Thus, accelerator performance, especially the luminosity, is much improved since the 1970s. Fig. 1.4 shows the Luminosity improved in high-intensity ion accelerators.

Figure 1.3: Livingston Plot shows the history of particle beam energy increasing [19].

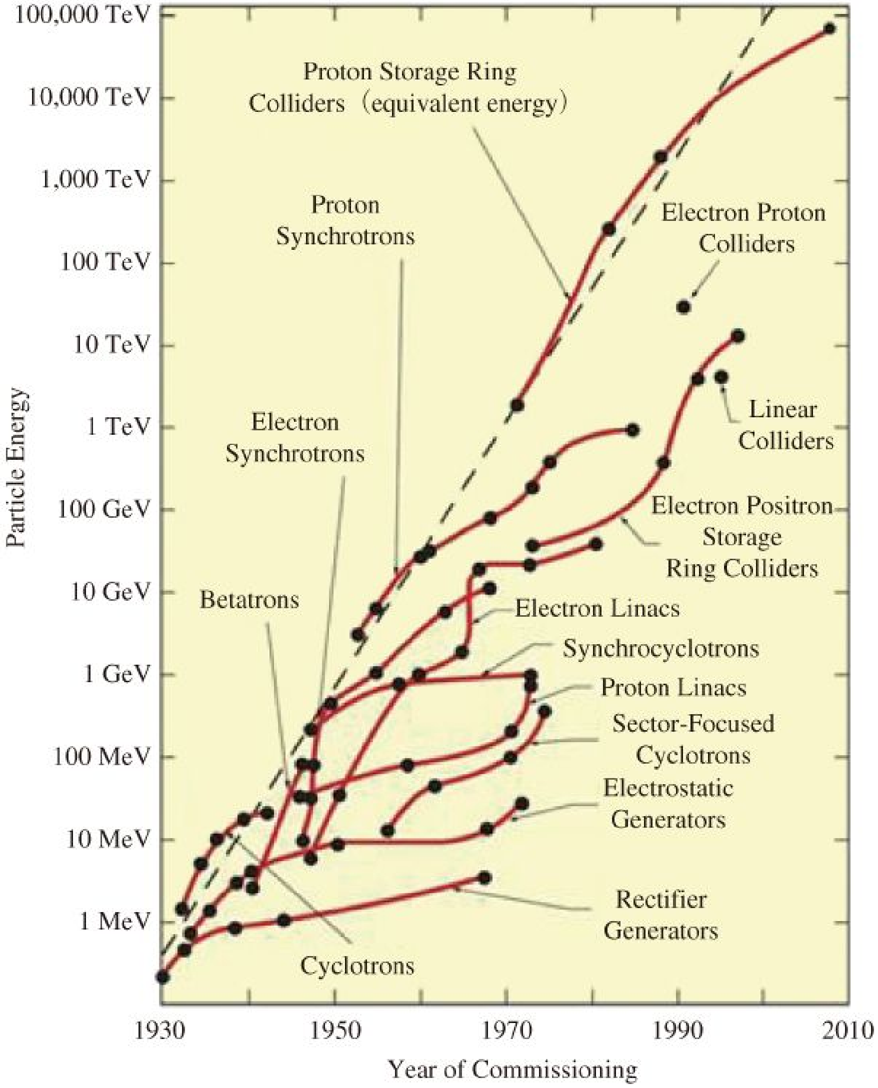

1.1.2 History of SRF Accelerators

With the continuous development of high-energy physics, the requirements of accelerated particle energy are higher and higher. By the 1970s, many accelerator laboratories planned to use superconducting technology to build accelerators in order to increase the energy and reduce the size of accelerators. Detailed introductions and summaries can be found in Ref. [22, 23].

Some examples of SRF accelerators include:

- Proton machine: SNS, ESS, CADS, MYRRHA, Project-X;

Figure 1.4: Improvement of the luminosity (particle/particle colliding performance), for past, present and possible future colliders [21].

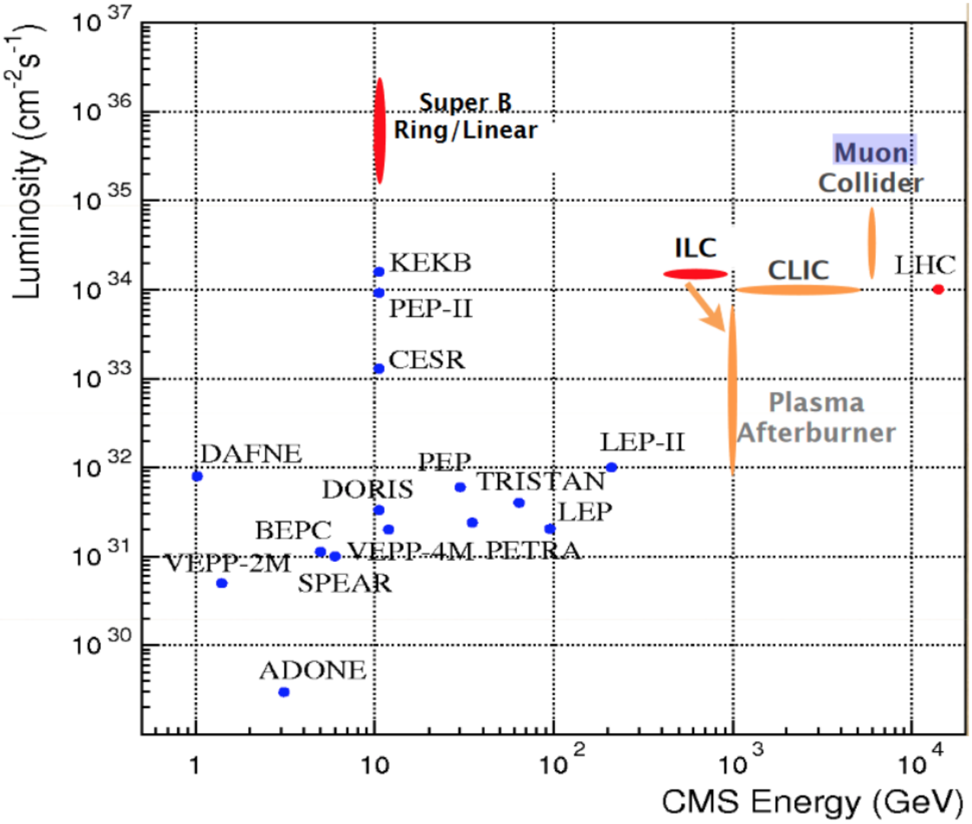

- heavy-ion machine: FRIB, IFMIF, EURISOL, ATLAS;
- electron machine: E-XFEL, KEKB, LCLS-II, ILC.

1.1.2.1 History of SRF and Several SRF Machines

The first successful application of SRF for particle acceleration was achieved in 1965 when electrons were accelerated in an SC lead-plated cavity at SLAC. This was a result of a series of developments in the early 1960's. In 1961, A. P. Banford and G. H. Stafford proposed and calculated the possibility of building a superconducting proton linear accelerator [24]. In 1962, Fairbank, Schwettman and Wilson Turneaure conducted pioneering studies on small scale TE011 and TM010 cavities and obtained a Q of 1 $\times 10^{10}$ at 1.7 K [25]. The accelerating fields in the cavities were close to the theoretical limit of 30 MV/m. At the 1963 International Conference on High Energy Accelerators in Dubna, the Stanford group published a very preliminary design of a 20 GeV, 10% duty cycle superconducting accelerator. This was at a time when no real cavity had ever been built. Robert Hofstadter made plans to build a 2 GeV superconducting accelerator in a tunnel on the HEPL site with a gradient of about 13 MeV/m. They obtained a gradient of only 2-3 MeV/m in full-scale accelerator structures at 1.3 GHz due to parasitic electron multipactor effects [22].

In the 1970's, R&D on niobium superconducting cavities started earnestly at many institutes including Stanford, Karlsruhe, CERN, Argonne, Cornell, KEK, U. Illinois, DESY [25]. The Superconducting Acceleration program at Stanford coincided with the invention of free electron laser. In 1968, Pantell from Stanford University added mirrors at both ends of the wiggler magnet through which the beam of electron LINAC passed, which improved the performance of millimeter wave spontaneous emission [26]. In 1975, J. Madey used the beam of a 24 MeV superconducting LINAC to obtain the free-electron laser (FEL) in the infrared band for the first time, which opened up a new scientific and technological field [27, 28].

Large-scale construction of SRF machines began in the mid-1980s. In those days, the interest of the high energy physics community was to discover the top quark, the last member of the six flavors of quarks, and the weak bosons (Z^0 and $W^{\pm}$). For this experiment, colliding electrons and positrons continuously at the same energy was the best way to increase luminosity. SRF cavities was the best choice for such a continuous wave (CW) machine due to their higher operating gradient ($\sim$ 5 MV/m) which brought economic benefits. Electron/positron ring colliders were designed for this purpose and R&D on large-scale application of SRF began in earnest. Four major developments took place in the 1980s: 1) elliptical cavities were invented to address the multipacting issues at DESY; 2) high-quality niobium material became commercially available from vendor production; 3) very reliable and reproducible surface treatment was developed, especially electropolishing (EP) at KEK; and 4) niobium film coated copper cavity at CERN. These advancements in R&D enabled the construction of large-scale SRF machines, which started in energy upgrade programs for ring colliders at TRISTAN at KEK, HERA at DESY, LEP-II at CREN, and CEBAF at JLab (this is not a collider but for a machine for quark nuclear physics) [25]. These projects are described in more detail below to demonstrate the use of SRF technology in accelerators.

The use of superconducting magnets in accelerators also occurred at the same time as the development of SRF technology. In 1983, Fermilab created a superconducting proton synchrotron [12]. After using superconducting magnets, the energy of the 400 GeV proton synchrotron with a diameter of 2 km was increased to 1 TeV. In 1991, the electron proton collider HERA was successfully built by DESY of Germany[29]. Its proton energy is 820 GeV, and its orbit length is only 6.3 km. These developments show that superconducting technology has been successfully applied to accelerators, which brings a good prospect for the construction of the accelerators. Accelerator experts from all over the world are encouraged to choose superconducting magnet technology to design accelerators with higher energy. In the LEP orbit of the existing large-scale Positron Collider (LEP), CERN has designed and built a 7 TEV proton collider LHC using a superconducting magnet with a high magnetic field (working temperature 1.9 K, magnetic field strength 8.33 T), and plans to accelerate the LHC to 1150 TEV (2.76 TEV/U) after stripping all the outer electrons of lead [22].

1.1.2.2 TRISTAN and KEKB

Since 1973, a storage ring complex, TRISTAN (Transposable Ring Intersecting Storage Accelerators in Nippon) planned a colliding beam scheme with electrons (or positrons) at 17 GeV and protons at 180 GeV. However, the design was finally changed to an electron/positron ring collider with beam energy of 28 GeV using normal conducting cavities (colliding energy of 56 GeV at center of mass), to explore the top quark. This is a circular collider, but it also consists of an octagonal tunnel connected with a straight accelerator to perform electron-positron impact experiments. The positron production accelerator and electron-positron linear accelerator have a length of 400 meters, an incident storage ring of about 370 meters, the main ring length of 3 kilometers and a depth of 11 meters underground. In the course of a linear accelerator, there is a facility for storing experimental equipment. The electron beam rotates clockwise, and the positron beam rotates counterclockwise to collide at interaction points. The octagonal ring shape is to reduce the curvature of the bent portion in which electrons and positrons lose energy by synchrotron radiation [22].

TRISTAN was energy upgraded by installing superconducting cryomodules. This project was the world's first application of SRF cavities on a large scale. By this upgrade project, TRISTAN colliding energy was boosted from 56 GeV to 64 (beam energy from 28 GeV to 32 GeV); 32 508MHz 5-cell bulk niobium cavities assembled into 16 cryomodules were installed and operated at 4.3 K. They used spherical shape for the structure to mitigate multipacting. This construction started in 1986, the first 8 cryomodules were completed in 1989, followed by the completion of the last 8 cryomodules in 1990. The specifications for the spherical shape cavities were: gradient $E_{acc} > 5$ MV/m and Q-value $Q_0 > 1 \times 10^9$ at 5 MV/m. TRISTAN SRF cavity performance was better than the spec by a factor two in many cavities; they achieved $Q_0 = 2.5 \times 10^9$ at 5 MV/m, and maximum gradient 10 MV/m [30]. Unfortunately, TRISTAN did not succeed in discovering the top quark (TEVATRON at FNAL discovered this quark at 173 GeV in 1995), but succeeded in demonstrating large-scale SRF application to the world. TRISTAN's other main contributions to the SRF community are: 1) made high purity niobium sheet with RRR 200 commercially available from niobium production companies (for example Tokyo Denkai); and 2) developed very reliable electropolishing (EP) method.

TRISTAN was closed in 1994. KEK switched to constriction of KEKB. This is an asymmetric electron (8.0 GeV) positron (3.5 GeV) colliding ring machine to discover CP violation. This is an intensity frontier machine, which needs to accelerate a beam current > 1A. They used single cell cavities and built 8 cryomodules which installed one 508 MHz cavity per cryomodule. The cavity performance was similar to TRISTAN ($\sim$ 5 MV/m at $Q_0 = 2 \times 10^9$, at 4.3K). The main R&D issues were high power input coupler ($\sim$ 1 MW at CW) and higher order absorber. KEKB applied TRISTAN SRF coaxial coupler, adding bias functionality on the inner conductor. KEK developed HIP bonded Ferrite ring inside copper cylindrical beam pipe. Higher-order mode (HOM) damper successfully worked and could damp HOM powers up to 16 kW (KEKB). KEKB upgraded the luminosity installing SRF carb cavities. Finally KEKB reached the Luminosity > 2.1×10^{34}. The major contributions to SRF community were: 1) development of extremely high beam load SRF system; and 2) development of crab cavity. KEKB has contributed to the establishment of the CP violation theory by Kobayashi and Masukawa. They received the Nobel Prize in Physics 2011.

1.1.2.3 HERA

HERA (Hadron-Electron Ring Accelerator) was a particle accelerator at DESY in Hamburg that began energy up operation in 1992 [29, 31]. At HERA, the only lepton-proton collider in the world during its operation, 27.5 GeV electrons or positrons collided with 820 GeV protons to provide a unique window on high energy physics. Protons and leptons were stored in two independent rings that were overlaid upon each other. The rings had four straight sections that constituted interaction regions. As a first in Europe, HERA used superconducting magnets for the entire proton ring [22]. After 15 years of data taking, HERA switched off in 2007.

HERA successfully demonstrated large-scale application of SRF cavities in 1991. Sixteen 500 MHz 4-cell cavities were fabricated using high RRR (300) niobium sheet materials. They also applied the spherical shaped cavities. HERA SRF cavity specification was: E_{acc} = 5 MV/m and $Q_0 = 1 \times 10^9$ at 5 MV/m at 4.3K. They used the buffered chemical polishing for their cavity processing. Their cavity performance was also better than their specifications, they achieved $Q_0 \sim 2 \times 10^9$, maximum gradient ~ 8 MV/m in the vertical test (certification).

1.1.2.4 CEBAF

The Continuous Electron Beam Accelerator Facility (CEBAF), founded in 1984, is a machine for nuclear physics. It is located in JLab in Newport News, Virginia, in USA. The machine appears like a racetrack with four distinct arcs on each end. Each of the two straight sections of the track consists of a superdoncuting linacs, whereas each arc section contains steering magnets matched with a different beam energy. In this novel design, the electron beam is recirculated through the linacs five times with increasing energy, and the beam bends in a different arc in each passing [32, 33]. CEBAF produced 4 GeV electrons in 1995, and has since undergone energy upgrades to reach 12 GeV.

To oeprate the SRF linacs in CEBAF, JLab houses the largest liquid helium refrigerator in the world [25]. CEBAF SRF system consists of 42 cryomodules and one quarter cryomodule, in which 338 1.5 GHz 5-cell niobium cavities were installed. All cavities were fabricated from high RRR niobium sheets. One cryomodule consists of four helium tanks, where each tank installs a pair of 5-cell cavities. The cavity adopted an elliptical shape to provide better mechanical stiffness and stability compared to the spherical cross section. The cavities were individually treated by BCP and rinsed with ultra-pure water. No hydrogen degassing was done. Two cavities were assembled in class 100 clean room into hermetically sealed pairs using indium gaskets. The performance of each cavity pair was measured prior to installation into the cryomodule. The specification of the CEBAF cavities are: $E_{acc} > 5$ MV/m and $Q_0 > 2.4 \times 10^9$ at 5 MV/m at 2 K. CEBAF cavity performance satisfied their specifications with a good margin.

1.1.2.5 TESLA

Since 1990, the great successes mentioned above directed the SRF community to an energy frontier machine to discover the Higgs particle (in those days, Higgs was not yet discovered but CERN discovered it in 2012 at the energy 125 GeV, since then, the goal changed to a Higgs factory to investigate the precise properties of Higgs in more detail) or other new elementary particles. The proposed machine is a linear collider with a colliding energy of 500 GeV (250 GeV + 250 GeV) at center of mass. TESLA (TeV Energy Superconducting Linear Accelerator) international collaboration started in 1990 aiming to develop a superconducting linear collider as the central lab of development at DESY. Electrons/positrons are accelerated only once in a long linac (15 km each) in this scheme. To reach such a high colliding energy, high gradient operation (originally 23.5 MV/m for TESLA but increased to 31.5 MeV for ILC) was required. In such a high gradient operation, the RF dynamic load is too heavy for cryogenics in CW operation, so the RF duty was reduced to several % instead. However, the pulse operation brings some difficulty in the SRF cavity operation (microphonics issue). The mechanical or PIEZO tuner development is another important R&D item. TESLA chose 1.3 GHz 9-cell niobium bulk cavities. TESLA R&D was focused on high gradient cavity performance, cost-effective cavity fabrication, cure for pulse operation, and cost-effective cryomodule production. In the high gradient cavity R&D, the high field Q-slope (HFQS), which is the main theme in this PhD program, limited the gradient below 20 MV/m. However, it was discovered that KEK recipe developed in TRISTAN R&D, i.e. EP + low temperature bake (LTB), could mitigate the HFQS perfectly. The gradient was pushed up to > 30 MV/m by this technology. However, in BCP'ed cavity case, LTB can not mitigate the HFQS. Many studies took place to understand this issue but it is still no conclusive result after more than two decades.

Superconducting and normal conducting linear collider developments were being completed in parallel until the early 2000s. International Committee for Future Accelerator (ICFA) selected SRF for the future linear collider in 2004. After 2004, TESLA changed its name to ILC (International Linear Collider) and the R&D was continued in many institutes including KEK, DESY, FNAL, Jlab, Cornell and Saclay. The aim was to start construction in mid-2020s. These research programs have improved SRF cavities and cryomodule system in reliability and cost-effective production. Now many institutes apply these result for the X-FEL machines in DESY, ICLS-II, Shanghai XFEL, etc. One example is shown below.

1.1.2.6 LCLS-II

The wide application of synchrotron radiation and the requirements from users to improve light source performance generates urgent demand for high brightness and ultra-short pulse light source. Hence the fourth generation of synchrotron radiation light source has been put on the agenda, and light source based on the free-electron laser is the primary way to realize the fourth generation light source. At the end of the 20th century, the Stanford Linear Accelerator Center (SLAC) started preliminary research on the linac coherent light source (LCLS), an X-ray free-electron laser based on electron LINAC. LCLS, which started lasing in 2009, uses the last third of SLAC's original 3 km normal-conducting LINAC. The success of LCLS motivated the LCLS-II project which will add a superconducting accelerator that occupies another one-third of SLAC's original 3 km linear accelerator tunnel. LCLS-II will generate an almost CW short pulse X-ray laser beam whose high repetition-rate greatly enhances the capabilities of the light source [12, 17].

LCLS-II employs 300 TESLA-type 1.3 GHz 9-cell cavities. The cryomodule is based on TESLA design but the return gas pipe is made much bigger for CW operation. The feature of LCLS-II cavity is in the high Q performance. LCLS-II cavity specification is $Q_0 > 2.7 \times 10^{10}$ at operation gradient 16 MV/m at 2 K. FNAL developed Nitrogen diffusion method to push up the Q_0 from 1-2 $\times 10^{10}$ in TESLA cavity to $> 3 \times 10^{10}$. LCLS-II applied this method. They already completed the production and are now installing cryomodules in the SLAC tunnel. They successfully achieved such a high Q cavity in industrial production. The maximum gradient is limited below 20-25 MV/m by this method due to HFQS. They are developing more high Q and high gradient cavity for LCSL-II HE.

With the continuous improvement of accelerator energy, scientific understanding of the microscopic material world is gradually deepened, and great achievements have been made in particle physics research. Nowadays, accelerators are used far beyond basic research. Accelerators are employed for materials science, solid-state physics, molecular biology, chemistry, geology and archaeology. There are also industrial applications in isotope production for the diagnosis and treatment of tumor, radiation sterilization, radiation breeding, food preservation, ion implantation, the radiation modification of materials, plum trace analysis, simulation of space radiation, nuclear radiation simulation and other applications. These applied accelerators have low energy but often require high intensity. They usually employ individual process devices that are convenient for specific applications. Therefore, there are also particular research and optimization directions.

1.1.2.7 ATLAS

The use of SRF in heavy ion accelerators is also undergoing intense development. One of the pioneers is ATLAS at Argonne National Laboratory. In 1998, the Argonne cascade LINAC system ATLAS used a 9 MV tandem electrostatic accelerator as the injection system, followed by a post accelerator composed of 46 and 97.0 MHz superconducting separation ring cavities. The RF power of the ATLAS is 6 kW. Four of the cavities are used for beam recombination and both.

Subsequently, a 48.5 MHz and 72.7 MHz 18 section superconducting quarter-wavelength cavity injector was built to improve the performance. The superconducting cavities are made of niobium and operate at 4.2 K low temperature. The phase of each superconducting cavity can be adjusted independently to operate under CW, so it can accelerate all kinds of ions from Li to U, with the energy of 5 - 17 MeV/u and beam intensity of 50 - 500 nA [34, 35].

1.1.3 Current Facilities

Accelerators in high energy physics or nuclear physics have two trends: High Energy Frontier (discovery machines) and intensity frontier machines. The typical example of a high energy frontier machine is the LHC mentioned above. An example of an intensity frontier machine is KEKB, which accelerates high current electron/positron beams with larger than 1 A current. In nuclear physics, the intensity frontier machine is key since very high energies are not necessary for relevant processes [22].

A summary of high-intensity ion accelerators operating or being planned around the globe is shown in Fig. 1.5. They serve a variety of purposes, including:

1. Nuclear physics (e.g. FRIB, USA; RIKEN, Japan; RISP, Korea; FAIR, Germany; HIAF, China).
2. The intensity frontier of high energy physics (e.g. PIP-II, USA; J-PARC, Japan).
3. Spallation neutron production (e.g. SNS, USA; ISIS, UK; ESS, Sweden).
4. ADS for nuclear waste transmutation and subcritical power generation (e.g. CADS, China; MYRRHA, Belgium).
5. Plasma physics with a beam-driven warm dense matter or high-energy-density physics (e.g. FAIR, Germany; HIAF, China).

A comprehensive overview as of 2014 can be found in Ref. [36]. A standard metric of high-intensity ion accelerators is the average beam power on target defined by (maximum beam energy

Figure 1.5: High intensity ion accelerators (Image courtesy of Prof. Jie Wei at FRIB) [36]

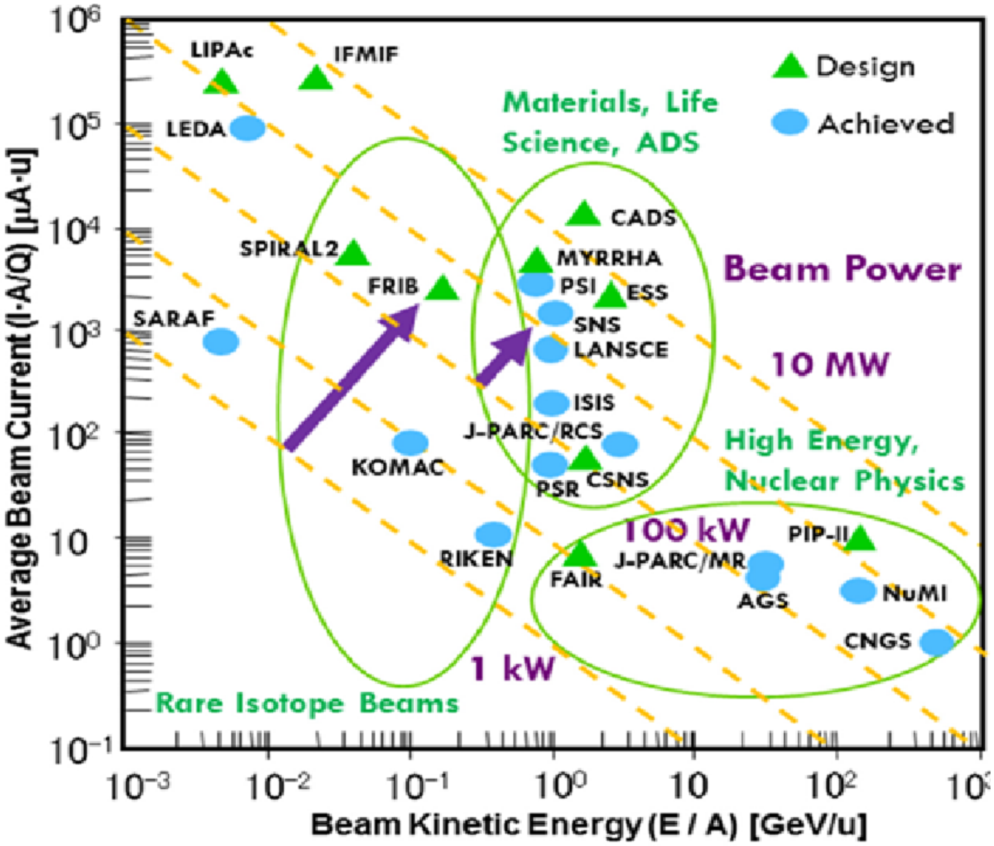

× average beam current). Proton accelerators have already achieved beam power above 1 MW, and multiple MW to >10 MW facilities are presently under construction. For heavy-ion accelerators, FRIB is set to advance the continuous-wave (CW) power frontier by two orders of magnitude when it reaches full operating specifications at 400 kW [37].

1.1.4 Facility for Rare Isotope Beams (FRIB)

The Facility for Rare Isotope Beams (FRIB) is under construction on the campus of Michigan State University. Fig. 1.6 shows the projected rare isotope fast-beam rates available at FRIB. The designed rates are several orders of magnitude higher than currently available rates and include thousands of undiscovered isotopes.

FRIB driver accelerator is designed to accelerate all stable ions (from proton to uranium) to energies above 200 MeV/u with beam power on the target up to 400 kW (Table 1.1). After

Figure 1.6: Chart of nuclides showing projected fast rare-isotope beam rates provided by FRIB in particles per second (pps). For reference, stable nuclides (black squares), the traditional closed nuclear shells (dashed lines), estimates of the astrophysical r and rp-process paths (solid black lines), and possible nucleon drip lines (solid grey lines) are depicted [38].

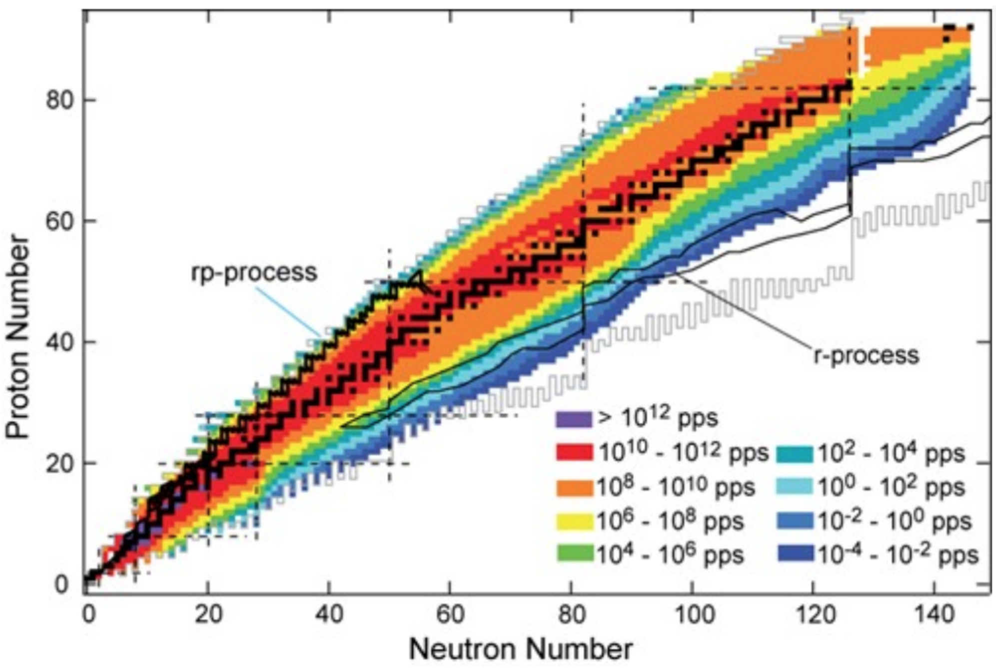

Figure 1.7: Layout of FRIB driver accelerator [36].

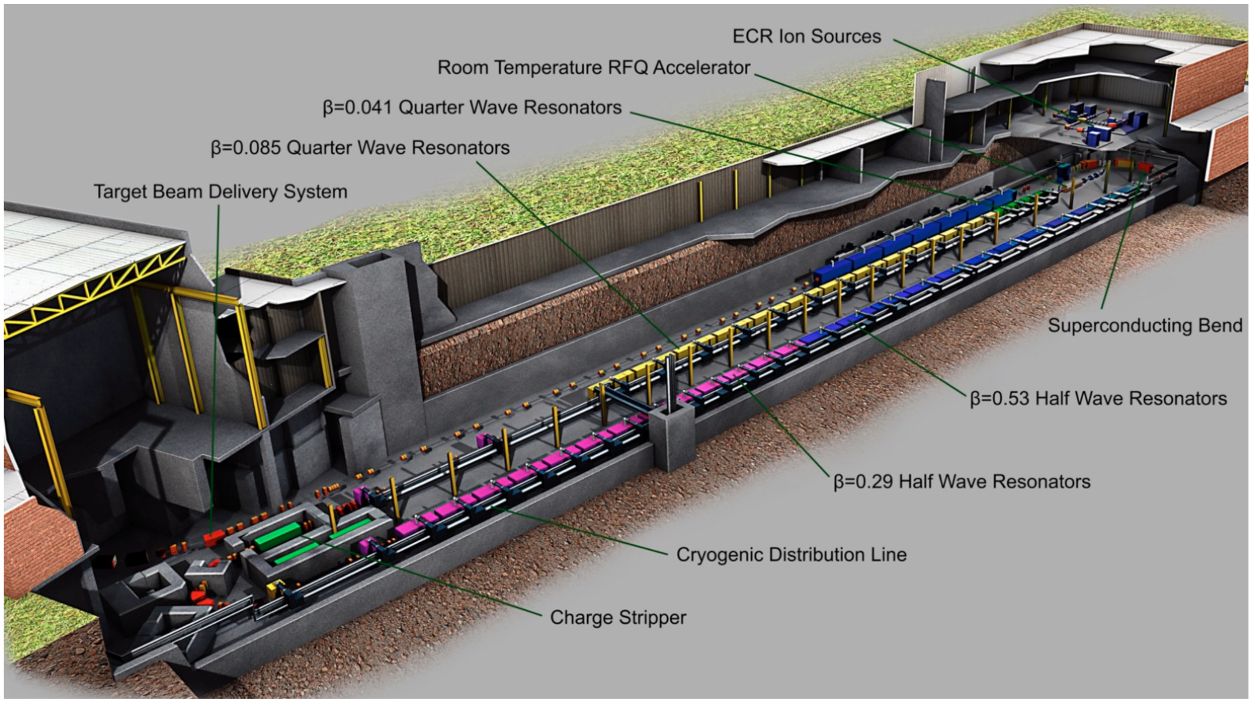

Table 1.1: FRIB driver accelerator primary parameters [36].

Parameter	Value	Unit
Primary beam ion species	H to ^{238}U	
Beam kinetic energy on target	> 200	MeV/u
Maximum beam power on target	400	kW
Macropulse duty factor	100	%
Beam current on target (^{238}U)	0.7	emA
Beam radius on target (90%)	0.5	mm
Driver LINAC beam-path length	517	m
Average uncontrolled beam loss	< 1	W/m

production and fragment separation, the rare isotope beams can also be stopped, or stopped and then reaccelerated. The fast, stopped, and reaccelerated rare isotope beams serve a vast range of scientific users in the fields of nuclear physics and applications.

As shown in Fig. 1.7, the driver accelerator is folded into three segments to optimize the use of space. It consists of:

- Electron Cyclotron Resonance (ECR) ion sources;
- a low energy beam transport containing a pre-buncher and electrostatic deflectors for machine protection;
- a Radiofrequency Quadrupole (RFQ) LINAC: LINAC segment 1 (with Quarter-wave Resonators (QWR) of $\beta = 0.041$ and 0.085) accelerating the beam up to 20 MeV/u where the beam is stripped to higher charge states, LINAC segments 2 and 3 (with Half-wave Resonators (HWR) of $\beta = 0.29$ and 0.53) accelerating the beam above 200 MeV/u;
- folding segments to confine the footprint and facilitate beam collimation;
- a beam delivery system to transport to the target a tightly focused beam.

The reaccelerator (ReA) consists of similar $\beta = 0.041$ and 0.085 accelerating structures. More cavities performances information can be found in Ref. [39].

FRIB produce more than 350 cavities: 16 $\beta = 0.041$ QWRs, 104 0.085 QWRs, 72 0.29 HWRs, 148 0.53 HWRs. One 0.041 cryomodule includes four QWRs, 0.085 cryomodule includes eight

Table 1.2: FRIB Cavities Performance 2 K [39]

Cavity	Gradient	Q_0
0.041 QWR	> 5.1 MV/m	1×10^9
0.085 QWR	> 5.6 MV/m	1×10^9
0.29 HWR	> 7.6 MV/m	5.6×10^9
0.53 HWR	> 8.1 MV/m	7.6×10^9

QWRs, 0.29 cryomodule includes 6 HWRs, 0.053 cryomodule includes 8 HWRs. There are totally 44 accelerating cryomodules, and two beam maching modules. All cryomodules were completed and installed in the FRIB tunnel. Now phased beam commissioning is underway, in order segment 1, 2, and 3. The cavity performance in vertical Dewar is shown in Fig.1.8 and Fig. 1.9.

The specifications are shown in Table 1.2.

All the cavities met the FRIB specification. FRIB cavities were treated by BCP, High pressure water rinsing, and assembled in class 10 clean room. Low Temperature Baking was not taken. Many of the cavities were limited by field emission. About 30% of cavities gradient were limited by High Field Q slope, which we will discuss in next chapter. If we succeed to resolve the HFQS issue with BCP'ed cavities, FRIB cryomodules operation will be pushed up to > 10 MV/m. This is one motivation of this project.

1.1.5 Accelerator Facility Components

Particle Accelerators are sophisticated devices, and generally consists of four essential parts and associated auxiliary systems.

1. Particle sources are used to provide the particles needed to accelerate, including electrons, positrons, protons, antiprotons, heavy ions...

2. The vacuum acceleration system has some form of accelerating electric field, and the whole system is placed in a vacuum chamber with high vacuum in order to accelerate the particles from being affected by the scattering of molecules in the air.

Figure 1.8: : Dewar test results for $\beta_m = 0.043$ QWRs: (a) Q_0 at 4.3 K; (b) Q_0 at 2 K; (c) X-rays at 2 K. [39].

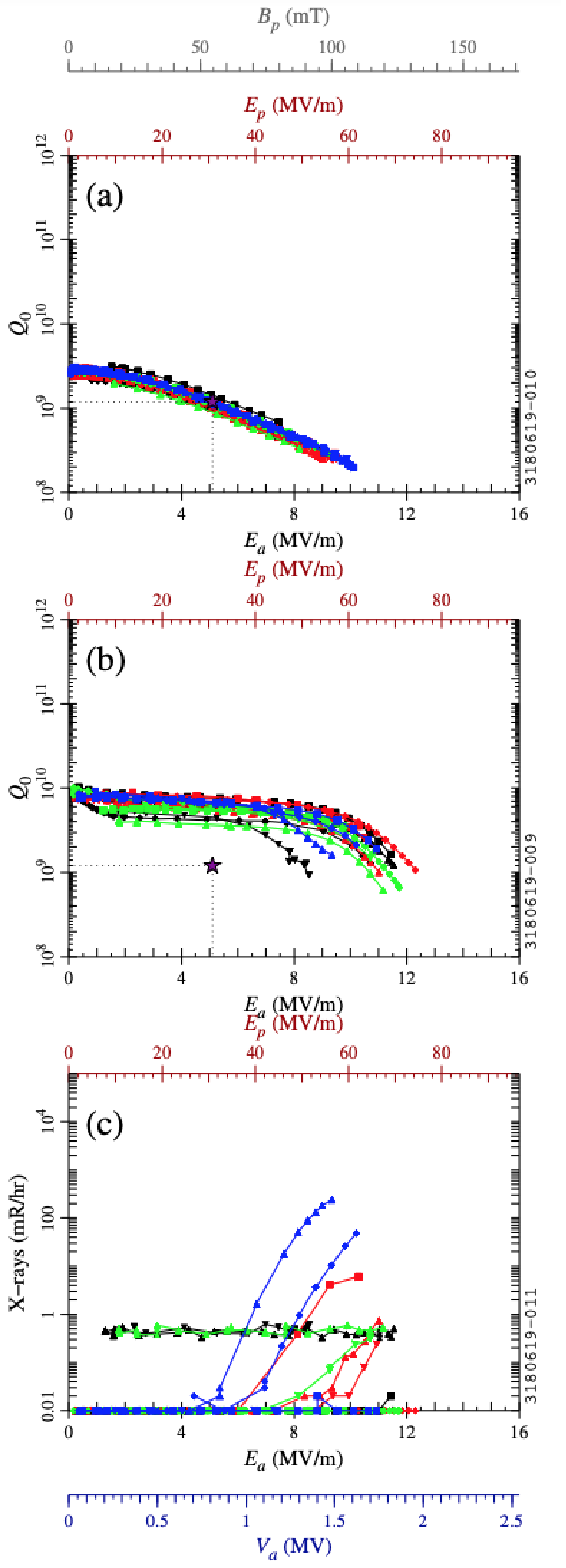

Figure 1.9: Dewar test results for β_m = 0.086 QWRs: (a) Q_0 at 4.3 K; (b) Q_0 at 2 K; (c) X-rays at 2 K. [39].

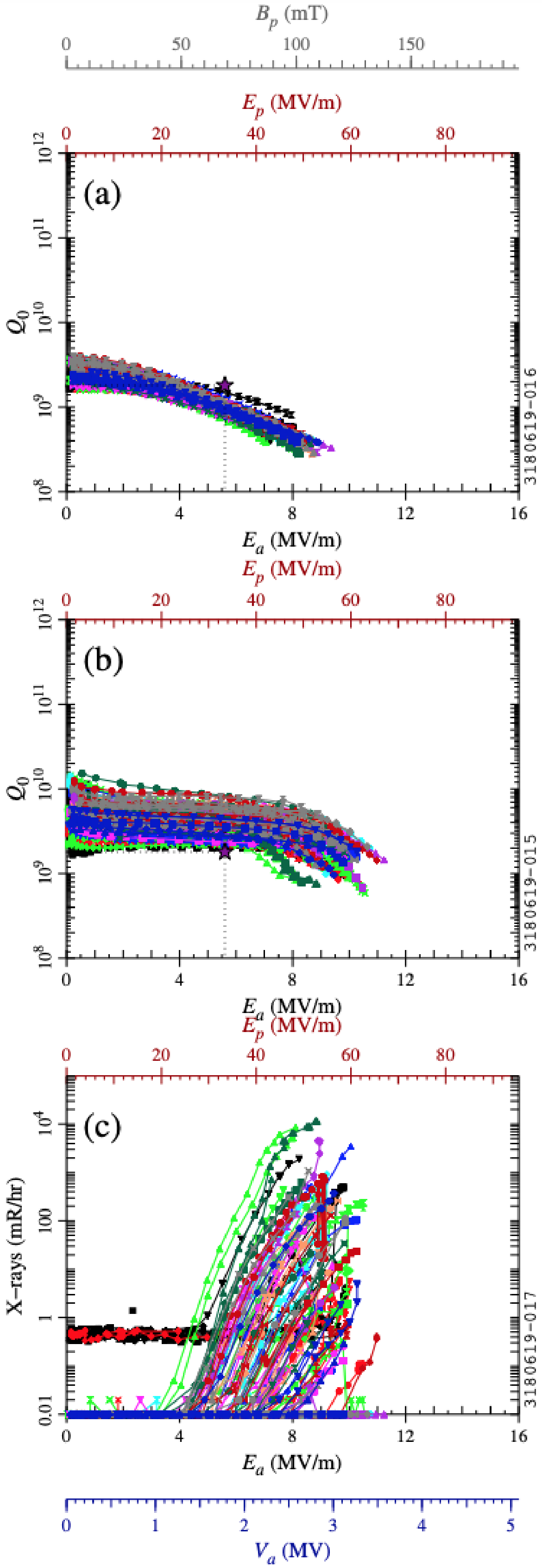

3. The guiding and focusing system uses a particular form of an electromagnetic field to guide and constrain the accelerated particle beam so that it receives the acceleration of the electric field along a predetermined orbit. All of these require the integration of precise and sophisticated technologies.

4. Beam transport and analysis system is composed of electromagnetic field lenses, bending magnets and electromagnetic field analyzer. It is used to transport and analyze charged particle beam between particle source and accelerator or between accelerator and target chamber.

1.1.6 Acceleration Field

To generate the accelerating electric field, one can choose DC or AC field. For accelerator using DC field, it needs a high voltage generator, for example, Van de Graaff generator (10 MV voltage). The advantage of DC acceleration is that it can accelerate any charged particles and can smoothly adjust the final energy. However, the voltage of DC acceleration is limited to 35 MV, by voltage breakdown, or vacuum breakdown (one possible explanation is field emission, see Ref.[12].). The examples of DC accelerator was discussed in Section 1.1.1.

Figure 1.10: LC circuit model of an accelerating cavity[40].

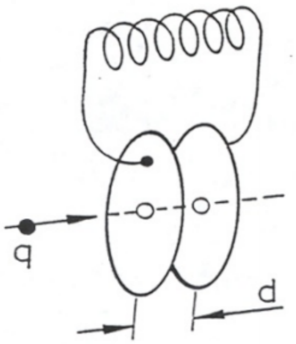

For acceleration using AC field, it can reach much higher accelerating gradient (several MV/m) and increase the space accelerating efficiency. A straightforward instrument that generates AC is an LC circuit (Fig. 1.10) with one capacitor (C) and one inductor (L), where the resonant frequency of the system is $\omega_0^2 = 1/LC$. By controlling the entering time and considering the charged particle's initial velocity, the particles can be accelerated or decelerated by the field between the capacitor's plates. The most applied AC field frequency falls into the radio frequency (RF) region (several 10 MHz to 3 GHz) because the resonant size at that region is more applicable.

1.2 RF Acceleration

An RF cavity is the essential acceleration element in an accelerator; it adopts RF resonant travelling wave or standing wave to generate a resonantly oscillating electric field to accelerate charged particles. (Travelling wave is applied normal conducting LINAC, while SRF cavity applies the standing wave.)

1.2.1 RF Resonant and Frequency

A simple LC circuit can evolve to an accelerating cavity resonator (Fig. 1.11), which encloses electromagnetic waves and prevents them from being radiated and associated power loss. Specific sizes are chosen to get a stably resonant standing wave and get acceleration field. Therefore the requirements of the size are related to the particle velocity, and some examples are shown in Table 1.3.

Figure 1.11: LC circuit evolving to a resonant cavity[40].

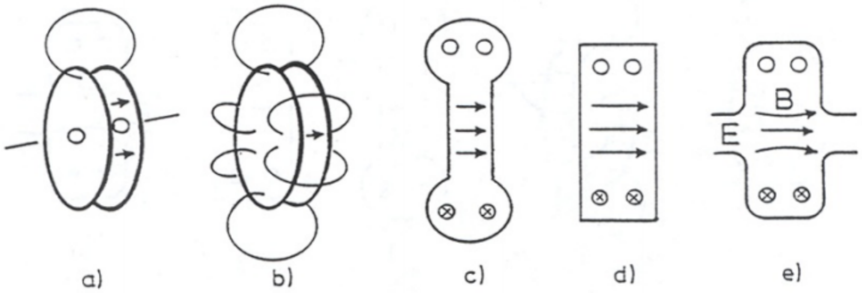

In order to accelerate the particle efficiently, the particle transit time should be less or equal to half period of RF wave:

$$\frac{d_{cavity}}{v_{particle}} \leq \frac{1}{2f_0}, \tag{1.5}$$

Table 1.3: Example of Cavity shape VS. β for different particles. Γ is the geometry factor that only relates to cavity shape [40].

Electron Accelerators	Proton Accelerators	Ion Accelerators
$\beta \approx 1$	$\beta \approx 0.5$	$0.05 \leq \beta \leq 0.2$
350 MHz ≤ f ≤ 3 GHz	500 MHz ≤ f ≤ 1.5 GHz	50 MHz ≤ f ≤ 150 MHz
$\Gamma \approx 270\ \Omega$	$\Gamma \approx 170\ \Omega$	$\Gamma \approx 20\ \Omega$
d ≈ 35 cm (f = 350 MHz)	d ≈ 20 cm (f = 350 MHz)	d ≈ 15 cm (f = 100 MHz)

where d_{cavity} is the length of the cavity and $f_0 = \omega_0/(2\pi)$ is the RF frequency. This equation is equivalent to:

$$2d_{cavity}f_0 \leq \beta c, \tag{1.6}$$

where $\beta = v_{particle}/c$ and c is the speed of light.

The final speeds highly depend on the particle mass due to relativity; thus the size and shape of the cavity depending on β also. Table 1.3 shows some examples of the sizes for different particles. Fig. 1.12 also shows some cavity examples of different frequency and β.

Figure 1.12: Cavity shape examples for different frequency and β [41].

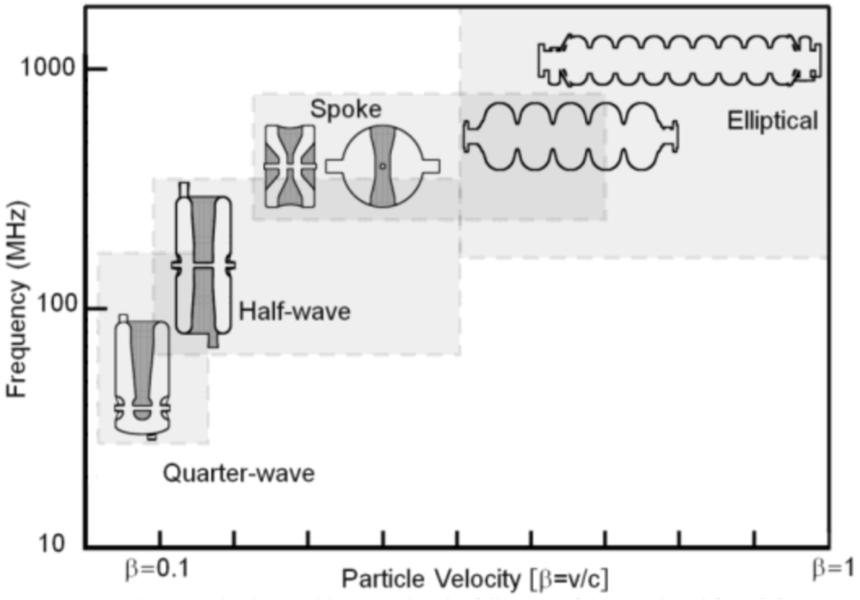

There are a lot of considerations in size and shape for optical cavity design, including the beam aperture, the frequency-based performance, the cavity surface processing difficulty, the material cost and the construction difficulty. These will be overviewed in the following sections.

1.2.2 Power loss and the Quality Factor

The power loss of a cavity is an essential index of cavity performance, it is not only the sign of electricity consumption but also influence the limit (for example thermal breakdown of a cavity) for the cavity. For an accelerator cavity, its power loss can be defined by current and resistance.

According to Ohm's Law, there exist a current density J near the surface of the conductor:

$$\mathbf{J} = \sigma \mathbf{E}_c = \frac{1}{\delta}(1-i)\mathbf{n} \times \mathbf{H}_c. \tag{1.7}$$

Where σ is the electric conductivity and E is the electric field. The average Power Loss P_{loss} per surface area S relates with J by:

$$\frac{dP_{loss}}{dS} = \frac{1}{2\sigma}|J|^2 = \frac{1}{2\sigma\delta}|H|^2 = \frac{1}{2}R_S|H|^2. \tag{1.8}$$

Here $R_S = 1/(\delta\sigma)$ is the surface resistance. Eq.1.8 can then be integrated over the cavity surface:

$$P_{loss} = \frac{1}{2}R_S \int |H|^2 dS, \tag{1.9}$$

To show that the power loss is related to the cavity surface resistance R_S and the applied field H over the surface. On the other hand, considering the energy U stored in the conductor, Stored Energy U:

$$P_{loss} = -\frac{dU}{dt}. \tag{1.10}$$

The Quality Factor Q of the cavity, which indicates the measure of the sharpness of the response of the cavity is defined as $2 \times \Phi$ times the ratio of the time-averaged energy stored in the cavity to the energy loss per cycle:

$$Q = \omega_0 \frac{U}{P_{loss}}. \tag{1.11}$$

By conservation of energy, so the power dissipated in Ohmic losses is the negative of the time rate of change of stored energy U. We can write U as the function of time:

$$\frac{dU}{dt} = -\frac{\omega_0}{Q}U, \tag{1.12}$$

with solution ($U(t{=}0) = U_0$):

$$U(t) = U_0 e^{-i\omega_0 t/Q}. \tag{1.13}$$

Compare to Eq.1.9 and Eq.1.10, we can get

$$P_{loss} = \frac{\omega_0 U}{Q}. \tag{1.14}$$

Combine with $U = \frac{1}{2}\varepsilon_0|E|^2 = \frac{1}{2}\mu_0|H|^2$, so that

$$Q = \frac{\omega_0 U}{P_{loss}} = \frac{constant}{R_S} = \frac{\Gamma}{R_S}. \tag{1.15}$$

Here the Γ is the Geometrical Factor that mentioned in Table 1.3 and can be calculated by:

$$\Gamma = R_S \cdot Q_0 = R_S \cdot \frac{\omega_0 U}{\frac{1}{2}R_S \int_S |H|^2 dS} = \omega_0\mu \cdot \frac{\int_V |H|^2 dV}{\int_S |H|^2 dS}. \tag{1.16}$$

In Eq. 1.15, Γ is only related to the cavity geometry designed and R_S is only related to the material properties.

1.2.3 Field in a Cavity

In Section 1.2.2, we mentioned the P_{loss} is determined by the surface resistance and applied field H. For the field in an RF accelerator cavity, the electric field is used to accelerate the charged particles, and the magnetic field generates heat and power loss.

The RF cavity can be treated as a waveguide. The electric field and magnetic field inside the waveguide can be derived from Maxwell's equations. Derivation details are shown in Appendix A. A detailed explanation can be found in Ref. [42–45].

The expressions for TM_{010} mode fields in a cylinder pillbox cavity that are commonly used for RF acceleration is:

$$E_z = E_0 J_0(\frac{2.045\rho}{R})e^{-i\omega t}, \tag{1.17}$$

$$H_\psi = -i\sqrt{\frac{\varepsilon}{mu}}E_0 J_1(\frac{2.045\rho}{R})e^{-i\omega t}, \tag{1.18}$$

where ρ is the r direction position, R is the radius of the cavity, ψ is the azimuthal angle, E_0 is the electric field in the center, $J_\alpha(x)$ is the ordinary Bessel Function of the first kind of order α. This groups of the function show the electric field and magnetic field value in every position with time variance.

1.2.4 Skin Depth

In a conductor, Ohm's law relates the electric field to the current density and so to the magnetic field via Ampere equation, the relevant equations are

$$\nabla \times \mathbf{H} = \mathbf{J}, \quad \nabla \cdot \mathbf{B} = 0, \quad \nabla \times \mathbf{E} + \frac{\partial \mathbf{B}}{\partial t} = 0, \quad \mathbf{J} = \sigma \mathbf{E}. \tag{1.19}$$

With $\mathbf{B} = \nabla \times \mathbf{A}$, Faraday's law shows that the curl of $\mathbf{E} + \partial \mathbf{A}/\partial t$ vanishes. As a result, we can write $\mathbf{E} = -\partial \mathbf{A}/\partial t - \nabla \mathbf{\Phi}$. With the assumption of negligible free charge and the time-varying B as the sole source of the electric field, we may set the scalar potential $\mathbf{\Phi} = 0$ and have $\mathbf{E} = -\partial \mathbf{A}/\partial t$. Note that we have the subsidiary conditions, $\nabla \cdot \mathbf{E} = 0$ and $\nabla \cdot \mathbf{A} = 0$. For a media of uniform, frequency-independent permerability μ, Ampere's law can be written $\nabla \times \mathbf{B} = \mu \mathbf{J} = \mu \sigma \mathbf{E}$. Elimination of B and E in favor of A and use of the vector identity, $\nabla \times \nabla \times \mathbf{A} = \nabla(\nabla \cdot \mathbf{A}) - \nabla^2 \mathbf{A}$, yields the diffusion equation for the vector potential,

$$\nabla^2 \mathbf{A} = \mu \sigma \frac{\partial \mathbf{A}}{\partial t}. \tag{1.20}$$

If we look at Eq.1.20, we may find out that this also holds for E. If the conductivity is constant in space, it follows that the B and J also satisfy the same diffusion equation.

We can estimate the time τ for decay of an initial configuration of fields with typical spatial variation defined by the length L. We put $\nabla^2 \mathbf{A} = O(\mathbf{A}/L^2)$and $\partial \mathbf{A}/\partial t = O(\mathbf{A}/\tau)$. Then

$$\tau = O(\mu \sigma L^2). \tag{1.21}$$

We can also estimate the distance L over which fields exist in a conductor subjected externally to fields with harmonic variation at frequency $\nu = 1/\tau$,

$$L = O(\frac{1}{\sqrt{\mu \sigma \nu}}). \tag{1.22}$$

For a field described by Eq.1.20, an example is showed in Fig. 1.13: A semi-infinite conductor of uniform conductivity σ and permeability μ occupies the space z > 0. The surface at $z = 0^-$ is subjected to a spatially constant, but time-varying, magnetic field in the x direction, $H_x(t) = H_0 \cos(\omega t)$. At $z = 0^+$ and the half space z > 0, the magnetic field still has only x component

Figure 1.13: Skin Depth

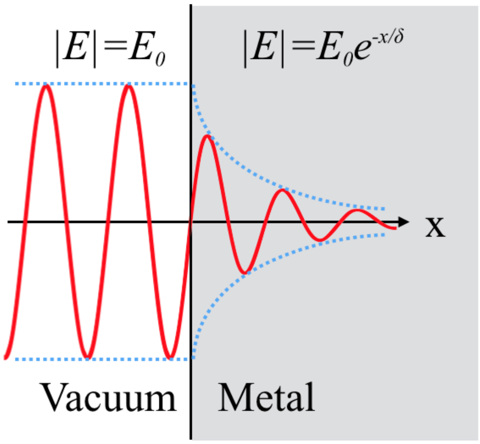

that $H_x(t) = H_0\cos(\omega t)$ because of the continuity of the tangential component of H, the normal component of B across z = 0 and the linearity of Eq.1.20.

The steady-state solution for $H_x(z,t)$ can be written as $H_x(z,t) = h(z)e^{-i\omega t}$, where from Eq.1.20, $h(z)$ satisfies

$$(\frac{d^2}{dz^2} + i\mu\sigma\omega)h(z) = 0. \tag{1.23}$$

A trial solution of the form, $h(z) = e^{ikz}$ leads to the condition

$$k^2 = i\mu\sigma\omega, \tag{1.24}$$

or

$$k = \pm(1+i)\sqrt{\frac{\mu\sigma\omega}{2}}. \tag{1.25}$$

Comparing with this result Eq.1.22, the square root has the dimensions of an inverse length characteristic of the medium and the frequency. The length is defined as the Skin Depth δ:

$$\delta = \sqrt{\frac{2}{\mu\sigma\omega}}. \tag{1.26}$$

So that $h(z) = e^{i\pm(1-i)\frac{z}{\delta}}$, the solution for H$_x$ is the real part of

$$H_x(z,t) = Ae^{-z/\delta}e^{i(z/\delta-\omega t)} + Be^{z/\delta}e^{i(-z/\delta+\omega t)}. \tag{1.27}$$

B must equals to zero, for the whole value not go to infinity as $z \to \infty$. Compare the solution to the boundary value, $H_x(0^+, t) = H_0 e^{-i\omega t}$, shows that $A = H_0$, so that the solution is

$$H_x(z,t) = H_0 e^{-z/\delta} e^{iz/\delta - i\omega t}. \tag{1.28}$$

From Ampere's and Ohm's laws, and knowing the fact that only $\mathrm{H}_x(z,t)$ exist for H_t ($H_t = H_x$) in this case, we know that there is only a tangential component of E_t, given by

$$E_t = |E_y| = |\frac{1}{\sigma}\frac{dH_x}{dz}| = \frac{1-i}{\sigma\delta} H_0 e^{iz/\delta - i\omega t}. \tag{1.29}$$

Define Surface Impedance Z, and

$$Z \equiv \frac{E_t}{H_t} = R_S + iX_S = \frac{1-i}{\sigma\delta} = (1-i)\sqrt{\frac{\mu\omega}{2\sigma}}. \tag{1.30}$$

So that the real part of Z,

$$Re(Z) = R_S = \sqrt{\frac{\mu\omega}{2\sigma}} = \frac{1}{\delta\sigma}, \tag{1.31}$$

R_S is Surface Resistance. This case can be easily applied to other directions of H. A detailed explanation can be found in Ref. [42–44].

1.2.5 Accelerating Voltage

We all know $V = Ed$ for a uniform E field across a gap d. By analogy, we take the Accelerator Voltage is:

$$V_{acc} \equiv \left|\int_0^d E_{acc} dz\right| = \left|\int_0^d E_z(\rho = 0, z) e^{i(kz+\phi)} dz\right| = \left|\int_0^d E_z(\rho = 0, z) e^{ikz} dz\right|. \tag{1.32}$$

We used $k = \omega/c$ here. For TM_{010}, $\mathrm{E}_z(\rho = 0, z) = E_0$, therefore:

$$V_{acc} = E_0 \left|\int_0^d e^{ikz} dz\right| = E_0 \left|\frac{ic}{\omega}(1 - e^{i\frac{\omega d}{c}})\right| = E_0 d \left|\frac{sin\frac{\omega d}{2c}}{\frac{\omega d}{2c}}\right|. \tag{1.33}$$

For half-pillbox, $\omega d/2c = \pi/2$, therefore

$$V_{acc} = \frac{E_0 d}{\pi/2}. \tag{1.34}$$

Another important property is the Transit Time Factor T, which takes into account the time-variation of the field during particle transit through the accelerating gap, for TM_{010}:

$$T = \frac{V_c}{|\int_0^d E_0 dz|} = \frac{V_c}{E_0 d} = \frac{2}{\pi} = 0.637. \tag{1.35}$$

A detailed explanation can be found in Ref. [42, 45].

1.2.6 Shunt Impedance, R/Q, E_p/E_{acc} and B_p/E_{acc}

The Shunt Impedance R_{SH} is defined as:

$$R_{SH} = \frac{V^2}{P_{loss}}. \tag{1.36}$$

It is a measure of the strength with which an eigenmode of a resonant radio frequency structure interacts with charged particles on a given straight line, typically along the axis of rotational symmetry. It indicates how efficiently energy is consumed for beam acceleration.

R/Q is a critical cavity parameter that is defined as follow:

$$\frac{R}{Q} = \frac{R_{SH}}{Q} = \frac{V^2}{\omega_0 U}. \tag{1.37}$$

R_{SH} depends on the surface resistance, so it depends on the materials. R/Q does not depend on the materials. R/Q means how strongly the acceleration energy is concentrated on the beam axis of the cavity, i.e. a measure of the goodness of the cavity shape.

A pillbox cavity has no beam pipe. The real cavity needs the beam aperture to let beam transit the cavity. This is out of the Pillbox cavity design. Computer codes are needed to design the cavity having an aperture. Here, the detail is not shown, but only the result is discussed. The RF surface electric field is strongest at the cavity bore aperture (iris). If the surface electric field is too strong, electrons will be field emitted from cavity surface (field emission, FE) by tunneling effect. If the work function of the metal surface is the smaller, the field emission becomes the more serious, i.e. exponentially increases due to tunneling effect. The contamination decreases the work function value and makes field emission easier. Speaking technical, one has to make clean this area to suppress the field emission.

Table 1.4: A comparison of superconductor (SC) cavity (Nb at 4.2 K) and normal conducting (NC) cavity [40].

	SC Cavity	NC Cavity
Q_0	2×10^9	2×10^4
R_a/Q_0	330	900
Dissipated power [kW/m] (for E_{acc} = 1 MV/m)	0.0015	56
Total AC power [kW/m] (for E_{acc} = 1 MV/m)	0.36	112

On the other hand, the smaller E_p/E_{acc} is better against FE. Therefore, in cavity design, E_p/E_{acc} is made smaller as much as possible. However, another parameter optimization interferes, for instance, the diameter of the bore. As a result, the realistic cavity design E_p/E_{acc} is about 2 for SRF cavities. This optimization is especially crucial for SRF cavities because their performance is susceptible to FE.

B_p/E_{acc} is not an issue with the normal conducting cavity (for example copper cavity), however, it is very important for Superconducting RF cavity design. Superconductivity collapses at a critical magnetic field (H_c for type-I, H_{c1}, H_{c2} for type-II). The candidate of the RF critical field is H_{c1}, H_{c2}, or H_c for the type-II superconductors. However, for SRF cavities, the real critical field is considered as the superheating field, which is about 180 - 200mT for niobium material. The magnetic quench happens at the high surface magnetic field area where locates around the equator of the cavity. In the SRF cavity design, B_p/E_{acc} is as small as possible. However, other factors, like beam bore radius interferes. The real SRF cavity optimization B_p/E_{acc} typically gives 3.5 - 4.5 mT/(MV/m). A detailed explanation can be found in Ref. [45].

1.3 Superconductivity

Superconducting RF cavities have some merits over normal conducting RF cavities because their small surface resistance below T_c and R_s of the superconductor is $\sim 10^5$ magnitudes smaller than the normal conductor, so that:

- Nearly all RF power goes to the beam, save the RF power budget, even considering the cooling cost.

- The continue-wave (CW) operation becomes applicable, in normal conductor copper case, the power dissipation of CW could melt the metal and break the cavity.

- The low electrical loss in an SRF cavity allows their geometry to have large beam pipe apertures while still maintaining a high accelerating field along the beam axis.

A comparison of a typical superconductor cavity and normal conductor cavity is shown in Table 1.4. The theory of superconductivity is not fully understood, much is still under investigation. Several models have strong supporting evidence — the two-fluid model and BCS theory — that will be introduced in this chapter.

1.3.1 Phenomena: T_c, Meissner effect and H_c

In 1908, Onnes succeeded in liquefying helium and then began to study the metal resistivity in this temperature region, finding that at 4.2 K, Hg's resistance mutated to a zero DC resistance state. For a long time after that, people regarded the superconducting state as the "ideal conductor" with zero DC resistance [46].

But that assumption has run into difficulties. In an ideal conductor, $\rho = 0$, so $\sigma \to \infty$, by $j = \sigma E$, has E= 0 in the conductor. We can get from Faraday's law, that in a conductor

$$\nabla \times E = -\frac{\partial B}{\partial t}, \tag{1.38}$$

and if we assume $\mu = 1$ as most metal is, we can get

$$B = \mu_0 H = \mu_0 H_a, \tag{1.39}$$

where H_a is the applying magnetic field before the resistance drop to zero. Therefore, when there is no resistance in the conductor, the magnetic field in the conductor remains the same no matter how the external magnetic field changes.

Thence, the ideal conductor first cooled to T$_c$ and then added the external magnetic field, and then added the external magnetic field and then cooled to T$_c$, and then removed the external magnetic field, the two order of the conductor internal magnetic field is not the same: the first is equal to zero, the second is equal to the external magnetic field.

However, in 1933, Meissner and Ochsenfeld found that the magnetic field inside a superconductor was always zero, regardless of the order applied. Even if a superconductor is cooled to a superconducting state with an external magnetic field, it will never have an internal magnetic field. This effect is called the Meissner effect [46, 47].

When Onnes discovered the superconductor, he immediately thought of making a non-dissipated magnet. However, when he added the magnetic field to the superconductor, the superconductor recovered its resistance and returned to the normal state when the magnetic field reached a certain value [48]. This field is called the critical magnetic field H$_c$. It is observed from experiments that most superconductor follows the relation:

$$H_c = H_c(0)[1 - (\frac{T}{T_c})^2], \tag{1.40}$$

where T$_c$ is the critical temperature, T is the real temperature, and H$_c(0)$ is the critical field at 0 K.

1.3.2 Explanation and Two Fluid Model

The physics of superconductors is exciting and encouraging. Even before the discovery of the Meissner effect in 1924, Keesom had been trying to apply thermodynamics to superconducting phase transitions [48, 49]. Even though he regards as that superconductors were still considered ideal conductors and superconducting transitions were considered non-equilibrium processes, which contradicted thermodynamics, which was based on reversible phase transitions. However, a series of thermodynamics formulas for the superconducting phase transition established by Keesom based on thermodynamic premise is consistent with a large number of experiments. Gorter proposed in 1933 that the success of Keesom's thermodynamic treatment means that superconducting phase transition should be reversible [50].

Another logical thought is about electrons. If all the electrons become superconducting electrons below T_c, then H_c should be temperature independent. In real, H_c has temperature dependence. Therefore the superconducting electrons are a part of the total number of electrons, and the other part is normal electrons. The ratio of the two must be temperature-dependent.

In 1934, Gorter and Casimir proposed a two-fluid model [48, 51]:

- When the conductor is in the superconducting state, the free electrons are divided into two parts: one is the superconducting electrons n_s, accounting for $\omega = n_s/n$ of the total; the other is the normal electrons n_n, accounting for $1 - \omega = n_n/n$ of the total. $n = n_s + n_n$. Two parts of electrons occupy the same volume, penetrate each other in space and move independently of each other. The relative number ω and $1 - \omega$ of two kinds of electrons are functions of temperature.

- n_s superconducting electrons condense in a low energy state.

- The n_n normal electrons are scattered by the conductor lattice and move randomly, which contributes to the entropy.

- The superconducting phase transition is a second-order phase transition, and the superconducting state is an ordered state.

This model can explain the superconducting state with zero resistance: when the temperature is lower than T_c, the motion of the superfluid electrons is unimpeded. If there is current in the conductor, it is all caused by the motion of the superfluid electrons. After the superfluid electrons appear, there is no electric field in the conductor, so the normal electrons do not load current, so there is zero resistance effect. Later we will calculate the SRF surface resistance based on this two-fluid model. One can see that this model can derive a very close formula to the BCS Surface resistance.

Figure 1.14: Specific heat Vs. T for Sn in superconducting state and normal conducting state [52].

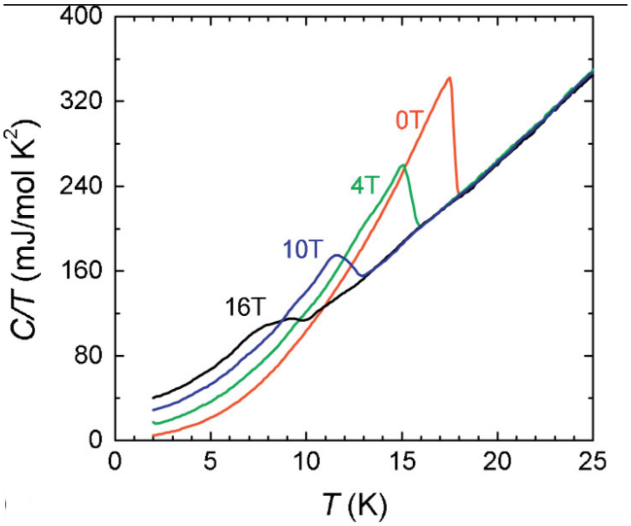

1.3.3 Thermodynamic Study of Superconductor

There are some inferences about the properties of superconductivity, which we will briefly introduce here but will not derive. The stable state of any system is the state with the lowest free energy. When the sample is cooled below T$_c$, it becomes a superconducting state. Therefore, when T < T$_c$, the free energy of the superconducting state must be less than the normal state. Besides, the superconducting state has a higher degree of order than the normal state, and the entropy of the superconducting state is also lower than the normal state. Moreover, since the phase transition process of superconducting state and the normal state does not change the latent heat, the phase transition at T = T$_c$ is a second-order phase transition in the case of zero magnetic field [48].

As with normal metals, the specific heat capacity of a superconductor consists of contributions c_g from the lattice and c_e from electrons. An experiment measured the specific heat of both superconducting and normal conducting Sn is shown in Fig. 1.14. The normal state below T$_c$ is achieved by applying different values of a magnetic field to Sn. Overall the superconducting specific heat is higher than the normal conducting state. There exists a leap around the T$_c$ for different values of applying field; the leap shifts to lower temperature when the applying field increases.

This extra specific heat capacity is mainly contributed by the superconducting electrons, which is also the conclusion of the experiment. Keesom [53] made X-ray diffraction images to study the lattice change of Pb before and after the superconducting phase transition in 1924; and Wilkinson made neutron scattering of Pb and Nb [54], before and after the superconducting phase transition in 1955. Both of which found no change in the lattice, indicating that the normal to superconducting phase transition only involved changes in the electronic turntable, independent of the lattice.

The two-fluid model can explain the change of specific heat capacity of superconductor near T_c: if the temperature of a superconductor is increased by ΔT, the first step is to destroy a_s ($a_s < n_s$) ordered superconductor electrons with n_s heat, and make them a_n ($a_n = a_s$) normal electrons, and then $n_n + a_n$ normal electrons get heat to do irregular thermal movement to increase the temperature of the system.

The thermal conductance of pure metals at low temperatures comes mainly from the thermal conductance of electrons. For superconductors, superconducting electrons carry no heat, so the thermal conductance in the superconducting state is still decided by the number of normal electrons. In the superconducting state, the number of normal electrons is decreased exponentially with distressing temperature. Therefore the thermal conductivity in the superconducting state is inferior compared to that in the normal conducting state (Fig. 1.15). It is an issue in SRF application if the thermal conductivity is too low. When RF is loaded into the SRF cavity, the imperfections on the SRF surface is RF heated, the temperature increases easily over the Tc, as the result quench happens (thermal instability) [55].

1.3.4 Type II Superconductor & GL Theory

When applying a low magnetic field, Type-II superconductors do not show complete Meissner effect (like Type I superconductor) but have a mixed state of superconductivity and normal conductivity (called as vortices state).

It occurs above a certain critical field H_{c1} (lower critical magnetic field). The vortex density increases with increasing field strength until superconductivity is destroyed at a higher critical field H_{c2}. The relation is shown in Fig. 1.16.

Figure 1.15: The dots curve shows the experiment result of the thermal conductivity ratio change with temperature for Nb, the solid line curve and the dashed line curve shows two theoretical predictions, where κ_s is the thermal conductivity in Superconducting state and κ_n is the thermal conductivity in the normal conducting state [56].

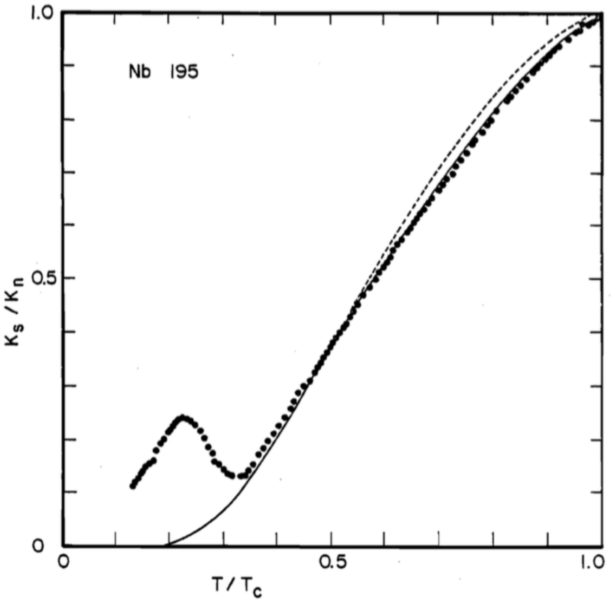

There was long confusing in these two types of superconductors until Abrikosov theory (1957) [57, 58] has been established. People regarded that the type-II was due to the low purity of the superconductor material.

In addition to experimental observations, the two superconductors can also be theoretically distinguished by the positive and negative interfacial energies. The Ginzburg-Landau theory [59–61] and Abrikosov gave the method of judging the interface energy by introducing a Ginzburg-Landau parameter κ:

$$\kappa = \frac{\lambda_L}{\xi_0}. \tag{1.41}$$

When $\kappa < 1/\sqrt{2}$, the interface energy is positive, and it is type I superconductor; when $\kappa > 1/\sqrt{2}$, the interface energy is negative, and it is type II superconductor. In the κ definition equation:

$$\lambda_L = \sqrt{\frac{m}{\mu_0 e^2 n_s}}, \tag{1.42}$$

is the London penetration depth. When a superconductor is placed in a magnetic field B_a, its

Figure 1.16: Type I and Type II superconductor H_c and T relation. There is a new vortex state for type II superconductor.

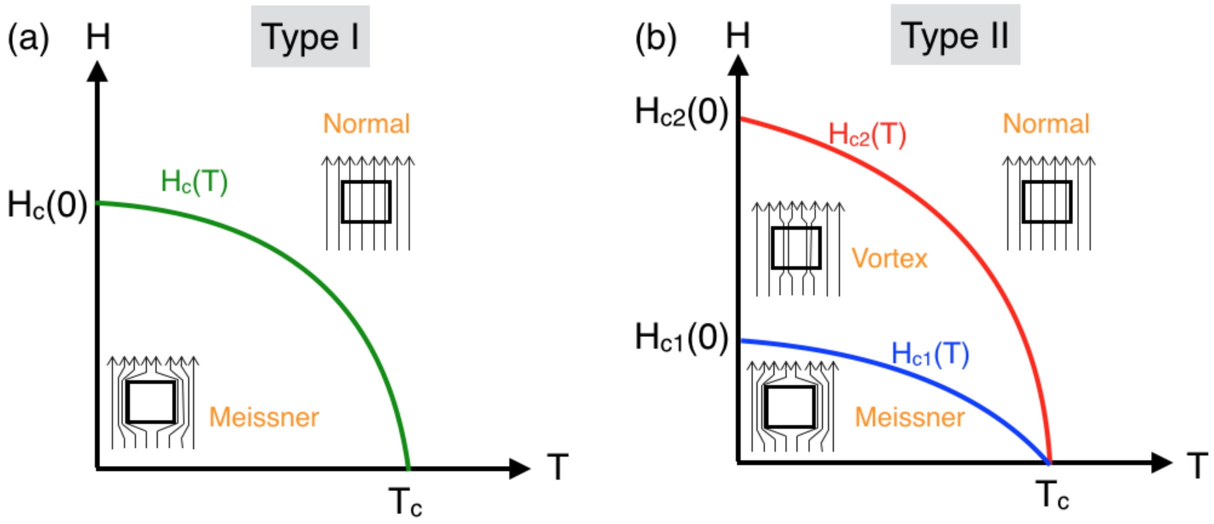

internal magnetic field near the surface decays exponentially with depth x.

$$B(x) = B_a(-\frac{x}{\sqrt{\alpha}}). \tag{1.43}$$

The London penetration depth $\lambda_L = \sqrt{\alpha}$ is the depth at which the magnetic field decays to $1/e$ of B_a. It is derived from London equations:

$$\frac{\partial}{\partial t} j_s = \frac{n_s e^2}{m} E, \tag{1.44}$$

for superconductor zero resistance and

$$B = -\frac{m}{n_s e^2} \nabla \times j_s, \tag{1.45}$$

for superconductor Meissner Effect.

Another parameter in 1.41 is the coherence length in the superconducting phase

$$\xi_0 = \frac{\hbar v_F}{k_B T_c}, \tag{1.46}$$

and it is the spatial extent of a Cooper pair introduced in Bardeen–Cooper–Schrieffer theory (BCS Theory) [48, 62].

Figure 1.17: Periodic arrangement of vortices in a type-II superconductor in an external applied magnetic field. Each vortex has a normal core, where the superconducting order parameter $|\psi|^2$ (blue line) drops to zero on the scale of ξ while the magnetic field profile (red line) exponentially decays on the scale of λ [63].

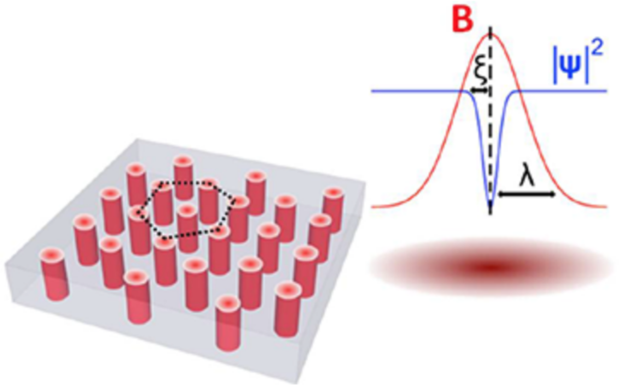

$$\kappa = \frac{\lambda_0(T)}{\xi(T)} = \frac{\sqrt{2}\mu_0 e}{\hbar}\lambda_0^2(T)H_c(T), \tag{1.47}$$

so that

$$\kappa = \frac{\mu_0 e}{2\sqrt{2}\hbar}\left|\frac{dH_c}{dT}\right|_{T=T_c}\lambda_0^2(0)T_c, \tag{1.48}$$

is the Ginzburg–Landau parameter, it is a constant for each superconductor and will not change with temperature.

In the Abrikosov theory, one can find two impotent formulas which relate to the easily measured parameters H$_c$, H$_{c2}$ [48] and ϕ_0:

$$H_c = \frac{\kappa}{\lambda^2}\frac{\hbar c}{\sqrt{2}e*} = \frac{\kappa}{\lambda^2}\frac{hc/2e}{2\pi\sqrt{2}} = \frac{\phi_0}{2\pi\sqrt{2}\lambda\xi}, \tag{1.49}$$

$$H_{c2} = \sqrt{2}\frac{\lambda}{\xi}\frac{\phi_0}{2\pi\sqrt{2}\lambda\xi} = \frac{\phi_0}{2\pi\phi^2}, \tag{1.50}$$

$$\phi_0 = \frac{hc}{2e} = 2.0678\times 10^{-15} \quad T\cdot m^2. \tag{1.51}$$

Fig. 1.17 shows the vortex state diagram and the model for a type II superconductor.

1.3.5 BCS Theory: Formation of Superconductivity

After expounding the experimental proof that superconductivity is caused by electrons and has nothing to do with the lattice, Corak made more accurate measurements of the specific heat capacity of superconductors with the change of temperature in 1956, and found that the specific heat capacity of superconductors and temperature is exponential [64]. The relationship between the number of electrons crossing the energy gap and the temperature is similar in a single electron system with an energy gap. In 1960, P. l. Richards and M. Tinkham experimentally measured the energy gaps of some superconductors [65].

The proof of the existence of an energy gap leads to the thermodynamic study of superconductivity in which electrons condense below an energy gap to form a stable state. Besides, to reduce the energy of the system, the electrons must have an attraction other than the Coulomb repulsion, which is due to the electron-phonon interaction.

E. Maxwell discovered in 1950 that the critical temperature of the Hg isotope's T$_c$ had a relationship with its mass of $T_c M^\alpha$ = Constant, revealing the effect of the lattice on electron behavior in the superconducting state [66]. In 1950 Fr$\ddot{o}$hlich proposed a physical model: electron-phonon interactions could couple electrons together as if they were interacting with each other [67]. The presence of a lattice can help shield electrons from Coulomb repulsion, from $\varepsilon_0 e^2/r^2$ to

$$\frac{1}{r}e^{-r/\lambda_D}, \tag{1.52}$$

and from Coulomb forces over long distances to short-range forces of $\lambda_D \sim 10\mathring{A}$, which is the Debye shielding length.

The model of superconductivity produced by electron-phonon interaction can explain why superconductors are all bad conductors: for example, the critical temperature of Pb is very high, so the electron-phonon interaction is very strong, so they are bad conductors at room temperature; and good conductors such as Cu, Au and Ag at room temperature have very weak electron-phonon interaction, and there is no superconductivity at very low temperature.

It is assumed that the energy transition of an electron causes the fluctuation of charge density in the conductor to $\delta\rho^e$, which affects the simple harmonic vibration of the lattice and causes a forced oscillation. We know that in the process of undamped forced oscillation, only when the frequency of the forced force is less than the natural frequency, the motion and the forced force can be in phase, and only in phase can bring attraction. This requires

$$\frac{1}{\hbar}|\varepsilon(\boldsymbol{p}_1) - \varepsilon(\boldsymbol{p}_1')| < \omega_D, \tag{1.53}$$

where ω_D is the Debye frequency and is the average frequency of the crystal lattice; $\varepsilon(\boldsymbol{p}_1)$ and $\varepsilon(\boldsymbol{p}_1')$ are the energy of the electron before and after the transition.

According to Pauli's incompatibility principle, there are only two electrons with an opposite spin in each energy state at absolute zero degrees. The distribution of electron state is Fermi distribution, and Fermi energy E_F is the maximum value of energy. Because the maximum frequency or average frequency of lattice vibration is far less than E_F, only the electronic transition near Fermi surface can make the formula hold, and the energy difference of electronic transition deep in Fermi surface is acceptable must be higher than $\hbar\omega_D$.

For the two electrons in this state, if their momentum is $\boldsymbol{p}_1$ and $\boldsymbol{p}_2$, the total momentum before and after the transition should be conserved as $\boldsymbol{p} = \boldsymbol{p}_1 + \boldsymbol{p}_2 = \boldsymbol{p}_1' + \boldsymbol{p}_2'$, and the respective momentum after the transition should be about equal to $\boldsymbol{p}_F$, then the two electrons before and after the transition are limited to the shadow of the intersection of the two spherical shells. When $\boldsymbol{p} = 0$, the momentum direction of the two electrons is opposite, and the magnitude is the same, the volume of the intersecting part of the sphere shell reaches a sharp maximum, then the probability of the electron transition through the attraction reaches the maximum. Therefore, two electrons with opposite momentum near the Fermi surface have the strongest attraction. The bound state of the two electrons is called the Cooper pair. Also, because the Pauli principle forbids the electron with the same spin being close to each other, Cooper pair requires the opposite spin beside the opposite momentum near Fermi surface ($\mathrm{E}_F \pm \hbar\omega_D$ range).

The above is the explanation at $0K$. At $T \neq 0K$, some states near Fermi surface are occupied by thermally excited electrons, which affect the formation of Cooper pair, reduce the transition of electron pair, and gradually weaken the effective attraction. At a specific limit temperature,

Table 1.5: $2\Delta(0)/k_B T_c$ value of some superconductors measured by tunnelling method [48].

Superconductor	T_c	$2\Delta(0)/k_B T_c$
In	3.41 K	3.63 ± 0.1
Nb	9.22 K	3.84 ± 0.06
Pb	7.20 K	4.29 ± 0.04
Sn	3.72 K	3.46 ± 0.1

the attraction will be reduced to a level that is not enough to shield the Coulomb force, or the states that a pair of electrons may transition are all occupied by thermally excited electrons, and the superconducting state disappears. This temperature is the critical temperature, and its size is related to the attraction strength of electrons at absolute zero. More information can be found in Ref. [48].

This theory can also explain the isotopic phenomenon: when the lattice ion mass becomes larger, the frequency of phonon ω_D decreases, the number of states of a pair of electrons forming Cooper pair decreases, the attraction decreases, and the T_c also decreases.

$$k_B T_c = 1.14\hbar\omega_D e^{-1/N(0)V}, \tag{1.54}$$

is the famous BCS T_c equation [48, 68]. Another essential parameter for superconductor is the energy gap:

$$\Delta = \frac{\hbar\omega_D}{sh\frac{1}{N(0)V}} \approx 2\hbar\omega_D e^{-\frac{1}{N(0)}V}, \tag{1.55}$$

and it has a relation with the critical temperature:

$$2\Delta(0) = 3.53 k_B T_c. \tag{1.56}$$

Both the energy gap and the critical temperature can be measured in experiments, and they agree with Eq. 1.56.

1.4 The Reason of Choosing Nb

There is much consideration for choosing the material to fabricate superconducting RF cavity. Among those superconductor materials, Nb is selected for most facilities based on the below reasons:

Table 1.6: H_c, H_{c1}, H_{c2} and Ginzburg–Landau factor κ value for some superconductors. $\kappa > 1/\sqrt{2}$ is type II superconductor. The values also depend on material purity. This table is adopting pure bulk Nb value [48, 69].

Superconductor	$H_c(10^{-1}T)$	$H_{c1}(10^{-1}T)$	$H_{c2}(10^{-1}T)$	κ
Nb	1.95	1.70	2.4	0.9
Nb_3Sn	5.4		245	45
Sn	0.309			0.2
In	0.29			
Pb	0.80			0.3

- Most high-temperature superconductors are ceramic (in the class of copper oxides) that are hard to do machining. Nb is a single element metal; it is soft to do shaping and easy to weld. Nb_3Sn (18.3 K) with higher T_C is another material well used to fabricate SRF cavity or magnets. It is extremely brittle, so the manufacturing of the Nb_3Sn SRF cavity is adding a vapor diffusion process to a formed Nb cavity.

- Metal superconductors also have better thermal conductivity than ceramic ones, which is important for keeping cavity surface on the superconducting state.

- The transition temperature of Nb is relatively high (9.22 K, as shown in Table 1.5) compare to other superconducting metal. This makes the superconducting state of Nb easy to reach and keep, which makes the system more reliable and saves cryogenic power.

- Nb has no serious pollution to the environment. Pb with T_C = 7.2 K was also used to product SRF cavities but was discontinued because it is harmful to human health and environment.

- Nb is Type II superconductor with H_{c2} = 240 mT (Table 1.6), is relatively high compared to other conductors, which makes its superconducting state easier to keep. Several additional surface treatments are necessary to avoid overwhelming heat in the vortex state.

1.5 Superconducting RF

We have discussed some of the analyses about normal conductors in an alternating electromagnetic field (Subsec: 1.2.4). In a superconductor, some relations are going to change since the resistance of the conductor becomes zero.

For normal conductors, the Skin Depth δ is defined as AC fields penetrate thickness where the current density falls to $1/e$ of the surface that $\delta = \sqrt{2/\mu_0 \sigma \omega}$. The Surface Impedance $Z_s = (1 - i)\sqrt{\mu\omega/2\sigma}$, and the real part of Z_s is the Surface Resistance $R_S = \sqrt{\mu\omega/2\sigma} = 1/\delta\sigma$.

For superconductors, the two-fluid model defines the London Penetration Depth λ_L as the H field penetrate to the superconductor and falls to $1/e$ of the surface.

$$\lambda_L^2 = \frac{m}{n_s e^2 \mu_0}, \tag{1.57}$$

where m and e are the mass and the charge of the electron, n_s is the number of superconducting state electrons (in the two-fluid model), μ_0 is the permeability of a vacuum. And the impedance

$$Z_s = \sqrt{\frac{i\omega\mu_0}{\sigma_n - i\sigma_s}} = R_S + iX_S. \tag{1.58}$$

So the surface resistance becomes

$$R_S = \frac{1}{2}\sigma_n \omega^2 \mu_0^2 \lambda_L^3, \tag{1.59}$$

where ω is the frequency of the field, and

$$\sigma_n = \frac{n_n e^2 \tau}{m}, \tag{1.60}$$

is the conductance, n_n is the number of unpaired electrons, τ is the mean free time.

For BCS theory, we already know that the number of unpaired electrons is proportional to exp(-Δ(0)/k$_B$T) when T < T$_c$, they form the normal current which flows parallel with the supercurrent that forms from the cooper pairs. This supercurrent carries the whole current due to its zero resistance. Cooper pairs only get scattered when the energy gain from the lattice vibration or the electric field exceeds the energy gap $2\Delta(0)$. These two conditions lead to the existence of a critical temperature T$_c$ (thermal lattice vibration limit) as shown in Eq. 1.56 and critical current density J$_c$ (electric field limit).

For RF currents, the cooper pairs do not screen the applied field perfectly due to (mass and momentum) inertia; a time-varying electric field is induced from the time-varying magnetic surface field in the skin layer. The electric field E_{int} is proportional to dH/dt, which is proportional to ωH, so that the internal current j_{int} is proportional to $n_{normal}\omega$H, and we know the $P_{diss} \propto E_{int} \cdot j_{int}$, so that

$$P_{diss} \propto n_{normal}\omega^2 H^2 \propto \exp(-\frac{\Delta(0)}{k_B T})\omega^2 H^2. \tag{1.61}$$

Compare with

$$P_{diss} = \frac{1}{2} R_S H^2, \tag{1.62}$$

we can get

$$R_s = A_s \omega^2 \exp(-\frac{\Delta(0)}{k_B T}). \tag{1.63}$$

A_s in Eq. 1.63 depends on the material parameters, such as the Fermi velocity v_F, the London Penetration depth λ_L, the coherence length ξ_0, the mean free path l, and the temperature T [45]. Separate the surface resistance by two parts by temperature dependence, we have $R_s = R_0 + R_{BCS}$ with R_0 is the residue resistance, and R_{BCS} is the BCS resistance. A simplified expression that fit experiment well (for T < T_c/2, f in GHz, and f« 2Δ/h ≈ 10^{12} Hz) is:

$$R_{BCS}(\Omega) = 2 \times 10^{-4} \frac{1}{T} (\frac{f}{1.5})^2 \exp(-\frac{17.67}{T}). \tag{1.64}$$

For superconducting Nb (T_c = 9.2 K), at T = 4.2 K, f = 100 MHz, $R_{BCS} = 2.5 \times 10^{-9}$ Ω, $R_0 = 1 \times 10^{-9}$ Ω, $H_c(0) = 1.59 \times 10^5$ (A/m); while for normal conducting Copper, R_s is ~ 10^{-4} Ω [45].

1.6 Frequency Selection for SRF Cavities

As we shown in Appen. A, the frequency is related to the size of a cavity. For example, for TM_{010} mode, a pillbox cavity radius R = $2.405c/(2\pi f)$ (as in Eq. A.47) and length d = $c/(2f)$ (as in Eg. A.48), both equations indicate lower frequency cavities have a larger size, and this makes the cavities have some properties:

- High diameter aperture is needed for high beam density, and it is only possible when the cavity size is big enough.
- Large cavities are hard to fabricate or do surface processing; it need more material and more cooling liquid, which increase the expense.

Figure 1.18: Cavity size comparison for different frequencies [70].

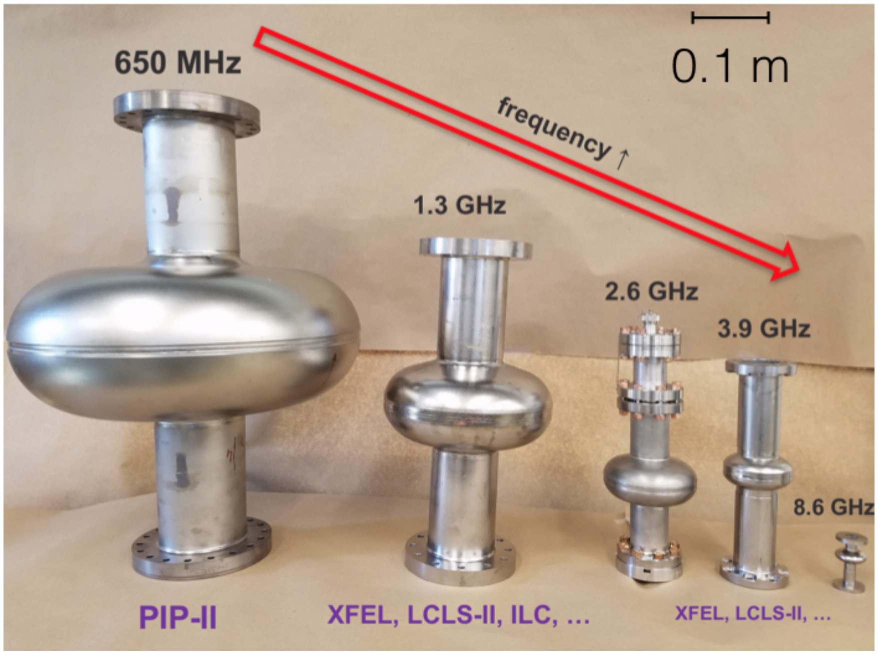

- Large cavities have more possibility of defects; the Nb type II superconductor may more normal conducting core, makes its performance not reliable enough.

Fig. 1.18 shows a comparison of cavities with different sizes. In the meantime, surface resistance of SRF cavity is $R_S = \frac{1}{2} \cdot (\sigma_n \omega^2 \mu_0^2 \lambda_L^3)$ (as in Eq. 1.59). This indicates that lower frequency cavities have lower surface resistance, and this sharply lowers the power usage of the facility and makes the system more stable. Some study shows that single-crystal Nb cavity has much better performance. However, the size of a piece of single-crystal is extremely hard to increase, so it can only fabricate high-frequency cavities. All these parameters need to be considered when selecting the cavity frequency.

1.7 Cavity Performance Limitation and Solution

Nb is Type II superconductor as introduced in section 1.3.4 and it has normal cores in vortex state when the magnetic field is between H_{c1} and H_{c2}. Surface defects, impurities and contamination could trap the magnetic field and cause extra heating in the normal cores, increase the size of them, and increase the risk of cavity quench. There are several potential cavity degradation parameters, the corresponding processing and some method that can improve the performance [71]:

- Centrifugal barrel polishing can effectively remove the surface layer that rich in large mechanical defects and contamination.
- Chemical Treatment, Electric Polishing (EP) and Buffered Chemical Polishing (BCP), can give the surface a clean and smooth surface with extra polishing with $\sim 100\ \mu$m removals.
- High-Pressure Water Rinsing (HPR) can wash away the acid residue and remove contamination particles, effectively reduce multipacting and field emission.
- Ultrasonic rinsing in H_2O_2 can remove sulfur surface contamination from EP acid.
- Post-purification and increase RRR and the thermal conductivity by using Ti gas getter to absorb oxygen, nitrogen carbon and other contamination elements.
- Low-Temperature Baking (LTB, at 120 °C) can diffuse the oxygen to deeper crystal structure and recover (totally for EP, partially for BCP) High Field Q slope (details in Chap. 2).

1.8 EP & BCP

As we mentioned earlier, surface processing is necessary to obtain a good RF surface. About 100 microns thick chemically etching (polishing) is a common step. This can remove the mechanically damaged layer or contamination [71].

Two kinds of chemical polishing are frequently used: Electric Polishing (EP) and Buffered Chemical Polishing (BCP). EP applies positive electrode to Nb metal cavity (anode) and adding a cathode made of aluminum, filled cavity half full with a mixed solution of sulfuric acid and hydrofluoric acid with a volume ratio of 1: 10, with a chemical equation

$$2\,\mathrm{Nb} + 10\,\mathrm{HF} + 5\,\mathrm{H_2SO_4} \xrightarrow{\mathrm{e^-}} 2\,\mathrm{NbF_5} + 10\,\mathrm{H_2O} + 5\,\mathrm{SO_2}\uparrow . \tag{1.65}$$

EP originally performed vertically, and it encountered difficulties that the roughness of Nb surface is high. After a while, Saito invented horizontal EP with an optimized current density

Figure 1.19: EP mechanism: current concentrates on the peaks and lead to more reaction on the peak area; this reduces the height difference between peak and valley, thus reduces the roughness of Nb surface [72].

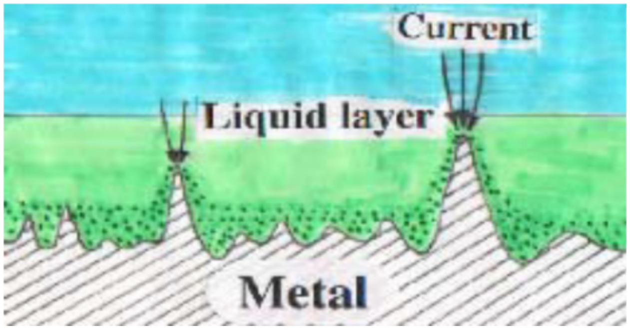

Figure 1.20: EP equipment Single-cell cavity setup at KEK [72].

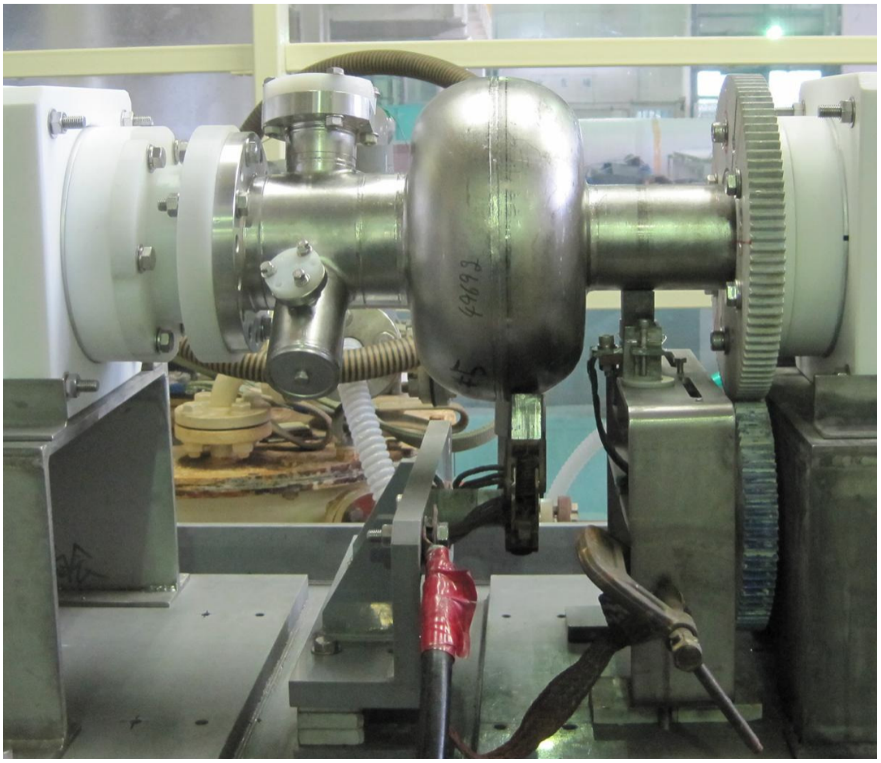

Figure 1.21: An example of a BCP system for a large cavity: acid is filled in and pumped out of the cavity by the pipe, then ultra-pure water is filled in to wash away the acid. Cooling water is spilled on the outside of the cavity [71].

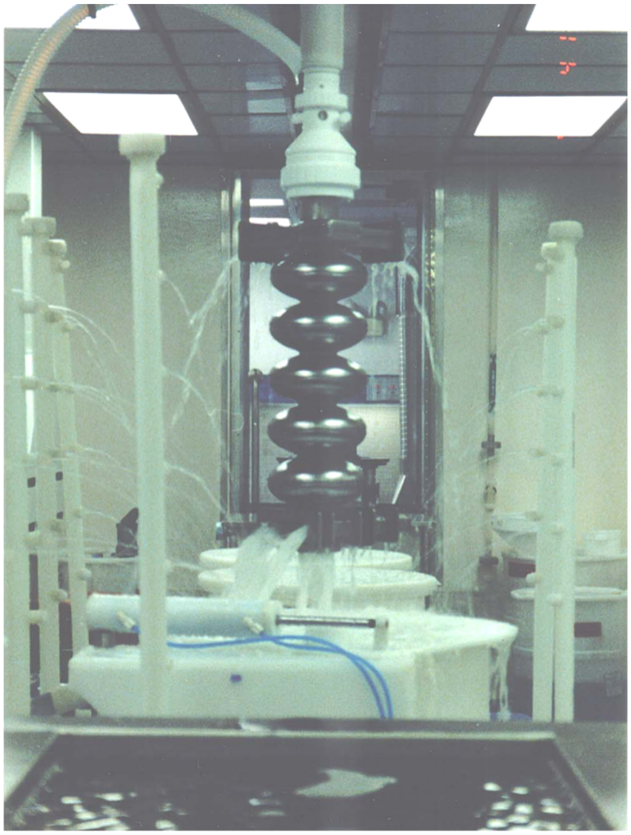

50 mA/cm^2 at 25 V, 30 °C with a rotation speed of 0.4 to 1 rpm. This EP generates a smooth mirror-like finishing surface because the current concentrate more at peaks than bottoms lead to more reaction of the peak area, and reduce the height difference and thus reduce high roughness. The schematic diagram is shown in Fig. 1.19, and one example is shown in Fig. 1.20.

While BCP is directly etching with nitric acid, hydrofluoric acid and phosphoric acid solution with a volume ratio of, 1: 1: X (where X is the number between 1 and 4 that regulates the rate of reaction), and the chemical equation for BCP is:

$$2\,\mathrm{Nb} + 10\,\mathrm{HF} + 2\,\mathrm{HNO_3} \longrightarrow 2\,\mathrm{NbF_5} + 2\,\mathrm{NO_2}\uparrow + 6\,\mathrm{H_2O}. \tag{1.66}$$

There are two ways of etching Nb parts with BCP: one is directly immersing them completely in the acid bath, this is very easy to apply and will etch the outside a bit which could consume some Nb and lead to less than requirement thickness. The other way is filling the acid to the large Nb structures (cavities) and cool the acid by cooling the outside of the cavity using cold water. The acid is pumped into the cavity and then drain out, then the system switches to ultra-pure water to rinse the cavity inside. In this case, the system is more complicated but safer, consuming less acid, and waste less Nb. Fig. 1.21 shows a system for Nb cavity etching.

EP is popular for simple shape cavities with high β; while BCP is cheap and easy to apply, and is popular for complicated shape cavities with low β.

CHAPTER 2

HIGH FIELD Q SLOPE

This chapter shows overviews of High Fields Q-Slope (HFQS) issue for buffered chemical polished (BCP) SRF niobium cavities, which is remained unresolved for 20 years. The main goal of this thesis is to discover the cause of the HFQS and develop the cure. Here, we will discover the cause of HFQS by mining past many efforts.

2.1 Discovery of HFQS

High Field Q slope (HFQS) is a phenomenon where Q_0 (unloaded Q) performance of the SRF cavity begins to exponentially drop with increasing gradient around 15 - 25 MV/m (ILC cavities) due to heating at RF high magnetic field region (equator area) on the SRF surface [73, 74], and it finally limits the acceleration gradient to around 30 MV/m. It happens to all cavities that adopt EP or BCP as a surface processing method. HFQS severely degrades the SRF cavity high gradient performance, thus limiting the final energy of the accelerated particles.

This problem was later neglected after the international linear collider (ILC) chose EP as the baseline surface preparation technology, which was developed in 1985 for KEK TRISTAN 508 MHz 5-cell SRF cavities [72], because EP'ed cavities can completely recover from HFQS via 120 °C bake for 48 hours [73]. Fig. 2.1 shows the Q_0 vs E_{acc} (accelerating gradient) of an EP'ed cavity before and after the Low-Temperature Baking (LTB). However, BCP'ed cavities still suffer from HFQS even after the LTB (see Fig. 2.2).

FRIB is an example of a heavy-ion accelerator project whose cavities suffer from HFQS. All FRIB cavities are treated with BCP. Statistically, the performance of $\sim 35\%$ of the cavities at FRIB is limited by pure HFQS (HFQS without X-rays) [76]. An example is shown in Fig. 2.5, the FRIB cavities experience Q_0 drop starting from $B_p \sim 85$ mT in $\beta = 0.041$ Quarter Wave Resonators (QWRs).

Figure 2.1: An example of High Field Q (HFQS) on EP Nb cavities, before and after baking. HFQS started at 28 MV/m for this cavity. [73]

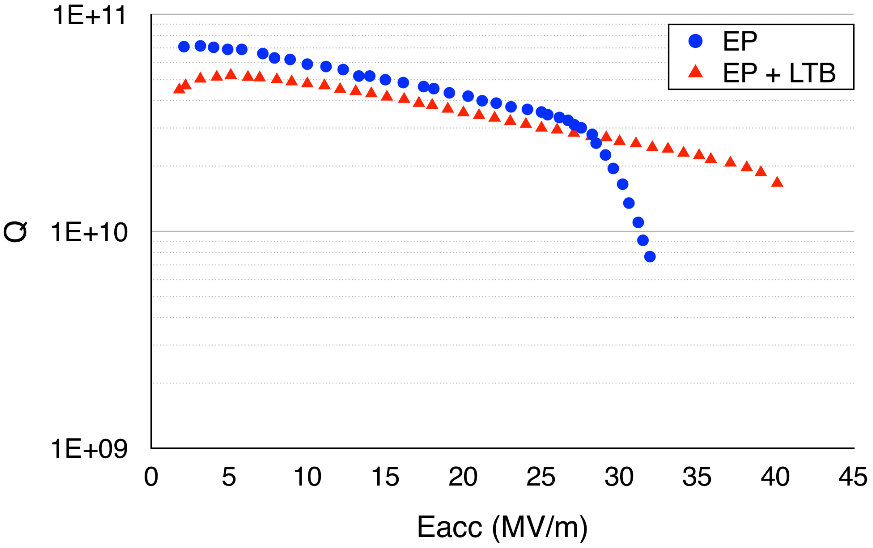

Figure 2.2: HFQS on BCP Nb cavities, before and after baking. (Courtesy of CEA-Saclay) [74]

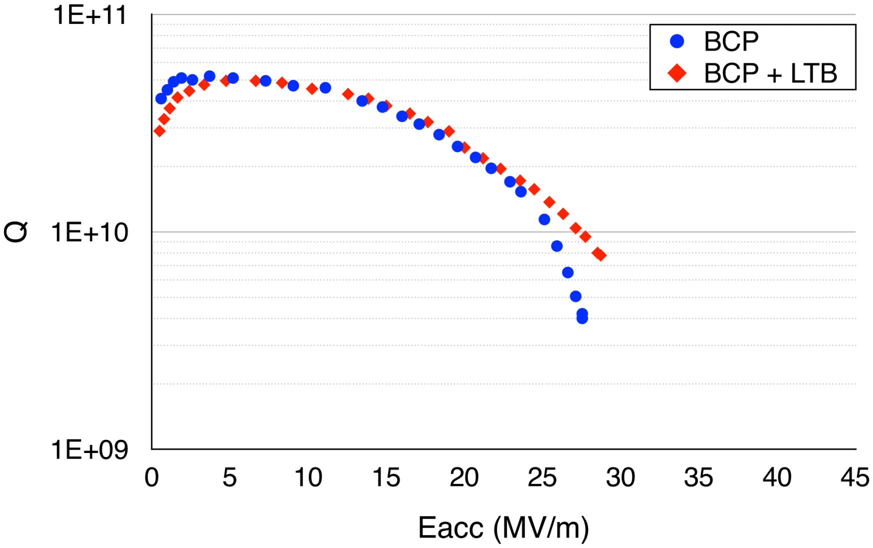

Figure 2.3: Variation of the surface roughness by EP for fine-grain Nb. [75]

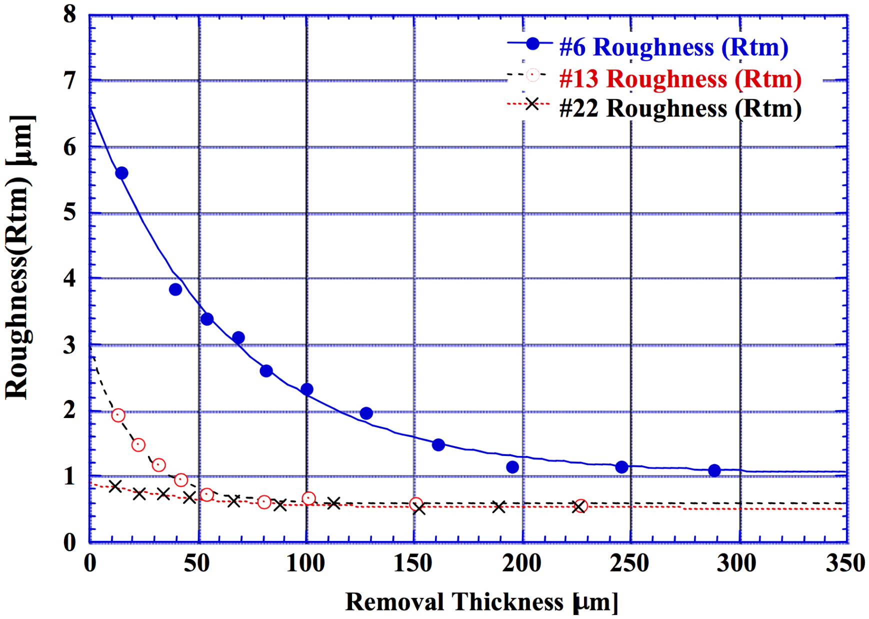

Figure 2.4: Variation of the surface roughness by BCP for fine-grain Nb. [75]

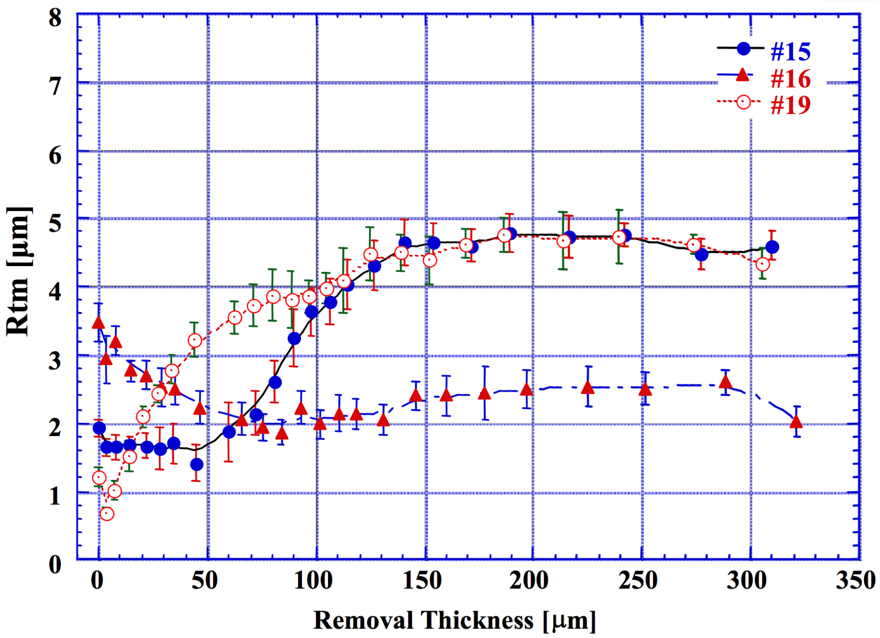

Figure 2.5: FRIB cavity performance at 2 K in Vertical Test, β = 0.041 QWRs, B_p/E_{acc} = 10.71 mT/(MV/m)

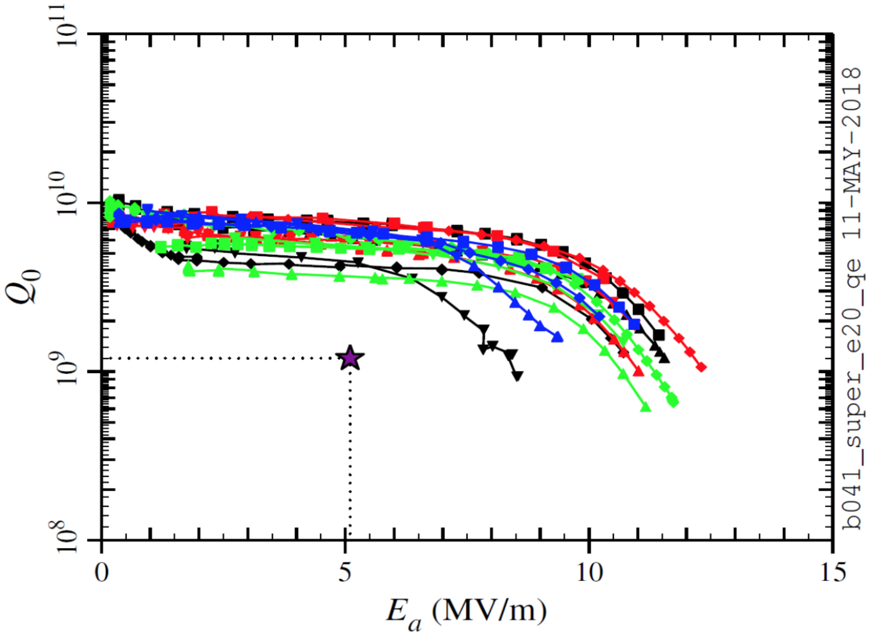

2.2 Low T Baking and the Role of Oxygen

There is an interesting history behind the LTB for EP'ed cavities. The superiority of EP over BCP with high gradient performance was discovered in 1996 at KEK [77]. They called the high field limitation with BCP'ed cavities as "European headache" (nowadays called HFQS) because European and US SRF institutes were mainly using BCP and having this problem.

KEK's preparation recipe included the LTB post EP. Its purpose was to improve high vacuum quality to evaporate absorbed water on the SRF surface. They did not yet recognize the critical role of LTB for the high gradient cavity performance at that time. KEK transferred their EP method to DESY in 1998, but the first EP'ed cavity at DESY suffered from HFQS. They revisited the KEK recipe and noticed they were missing the baking process. They applied the baking process and finally got high gradient cavity performance [78]. Since then, a very intensive study started to understand the HFQS in many SRF institutes in the world.

Among those studies, researches on niobium samples indicate that baking at progressively higher temperatures causes a conversion of the external Nb_2O_5 layer to metallic sub-oxides NbO,

NbO_2 and an overall reduction of the oxide layer thickness. This oxygen diffusion theory shows strong evidence because the diffusion effect matches the cavity performance [74, 79–81]:

1. At the effective baking temperature 80 - 120 °C, only oxygen and hydrogen sufficiently diffuse dipper to London Penetration Depth ($\lambda \sim 40$ nm) [79].
2. The LTB benefit increases and saturates at a certain limit at less than 200 °C, while hydrogen diffuse enough on a much lower temperature (less than 100 °C).
3. The saturation of cavity improvement matches the oxygen diffusion reaching the maximum, where the diffusion distance x reaches more than the London Penetration Depth.
4. According to oxygen diffusion simulation, 145 °C for 3 hours has similar diffusion depth to 110 °C for 60 hours, while the baking effect for these two conditions is also similar [80, 82].

Halbritter proposed a Taylor series of the surface resistance that obtained from the Ginzburg-Landau theory [83]:

$$R_s = R_{s0}[1 + \gamma(B_{peak}/B_c)^2 + O(B_{peak}^4)] \tag{2.1}$$

Where R_{s0} (equals to $R_{res} + R_{BCS}$) and γ are fitting parameters, and

$$\gamma = R_{BCS}(T_0)B_c^2\Delta/(2kT_0^2)(d/\kappa + R_k), \tag{2.2}$$

where κ is the thermal conductivity, R_k is the Kapitza resistance, d is the wall thickness, T_0 is the helium bath temperature, and B_c is the critical field $B_c(0) \sim 200$ mT. He explains the medium filed Q slope using this equation: the helium bath influences the heating of the inner surface of the cavity due to low thermal conductivity and Kapitza resistance of niobium. $\kappa_{Nb} \sim 6$ - 20 W/(m·K) for different purity niobium samples [84], the Kapitza resistance between Nb and helium is 1.25×10^{-4} (m^2K)/W. For Nb_2O_5, the thermal conductivity is 1 - 2 W/(m·K) [85], only 10% of the Nb metal and the Kapitza resistance is 0.05 (m^2K)/W [86].

2.3 Others' Study

There exists a lot of other models for the HFQS: thermal feedback [87], Oxygen contamination [74, 79–81], field enhancement at grain-boundary steps (or macro surface roughness, in this thesis we are mostly talking about this roughness) [88], field enhancement induced by surface roughness in the grain (or micro surface roughness) [89], interface tunneling exchange [90], Hydrogen trapping [91], and flux trapping [92]. A good summary is shown in the reference [93]. Among these models, the Oxygen contamination model can sufficiently explain HFQS in the LTB effect with EP'ed cavities [74]; however, it cannot explain why LTB fails to remove the HFQS for BCP'ed cavities. An entirely consistent model of HFQS with BCP'ed cavities does not exist even now. Recently, a new model based on Josephson Effect that weak superconducting cores increase exponentially with the field that generates the exponential power loss thus induces HFQS is built by K. Saito [94] which will not be discussed in this thesis.

As mentioned above, in the early 2000s HFQS studies with BCP'ed cavities were mostly for fine-grain niobium cavities. Discussion of the results focuses around the topography of niobium surface treated by BCP, as a natural consequence of the effects of surface roughness (Rtm, the height difference between the third-highest peak to the third-lowest minimum), grain-boundaries, defect and dislocation were the main concerns. Fig. 2.3 and 2.4 show the polishing characteristics of EP and BCP respectively [75]. EP makes the surface smoother exponentially with increased material removal. In contrast, BCP makes the surface smooth in the early stage but gradually rougher with increased material removal due to the preferential etching at grain-boundary areas, and the roughness saturates around 3 - 5 μm depending on the grain size of the niobium material. The experiments in the early 2000s established the following facts:

1. The LTB does not sufficiently improve BCP'ed cavity HFQS, the Q-drop is somehow mitigated, but the gradient limit sees little improvement (Fig. 2.2).
2. Sometimes the Q-drop is eliminated by the LTB, but the field limitation still does not change, unlike EP, especially in large-grain or single-crystal cavities.

Figure 2.6: Q vs E results for 6 different polishing treatments, all cavities are tested after HPR and baking in KEK. [71]

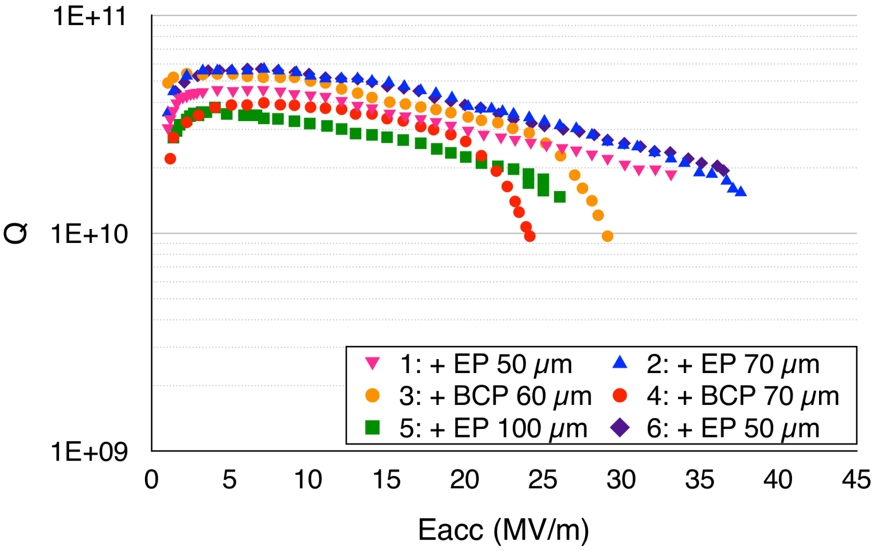

3. BCP after EP lowers the onset field of the HFQS. Successive BCP makes the HFQS (Fig. 2.6) worse.

4. The degraded HFQS is entirely recovered by EP plus LTB with a rather heavy material removal (150 μm, see Fig. 2.6). The RF field enhancement might explain the degradation of BCP HFQS on the rougher surface.

These experimental facts seem to support the field enhanced model on the rough surface [89] or grain-boundary steps [88]. However, more detailed analysis does not support these models for BCP HFQS as shown below.

2.4 Our Analysis

2.4.1 Reanalysis of Multiple BCP Post EP with Fine-grain Cavity

The cavity inner surface roughness in the experiments of Fig. 2.6 can be estimated from the surface polishing characteristics in Fig. 2.3 and 2.4. Table 2.1 shows the results. The calculation assumed

Figure 2.7: Roughness vs $E_{acc,max}$ results for 6 steps of the polishing treatment (each with HPR and baking) in KEK multiple EP and BCP experiment. Each result is marked with the respective number in Fig. 2.6. The roughness information is from Table 2.1. [71]

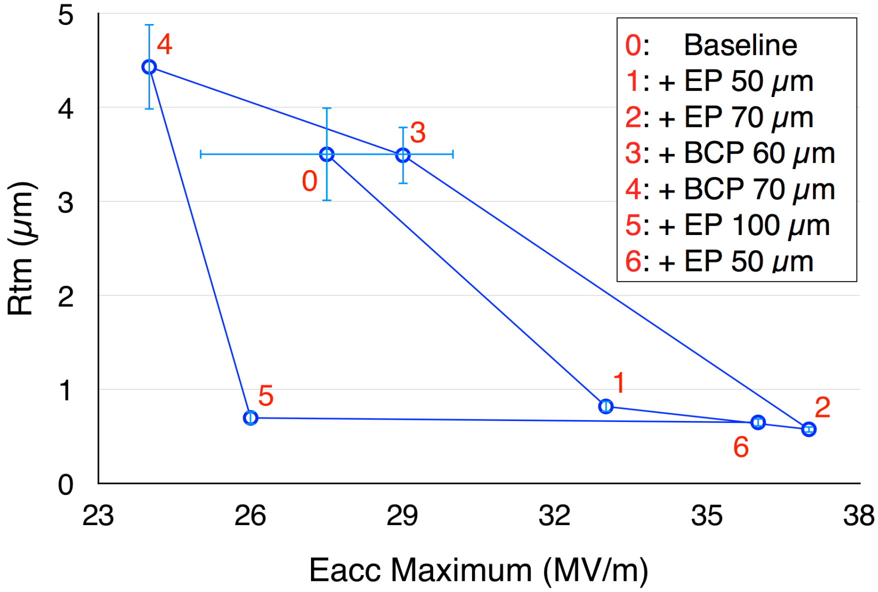

Table 2.1: Estimation of roughness during KEK multiple EP and BCP process.

Process	Rtm (μm)	Uncertainty (μm)
Baseline	3.50	0.50
+ EP 50 μm + baking	0.82	0.06
+ EP 70 μm + baking	0.57	0.04
+ BCP 60 μm + baking	3.49	0.31
+ BCP 70 μm + baking	4.43	0.46
+ EP 100 μm + baking	0.70	0.07
+ EP 50 μm + baking	0.65	0.05

initial surface roughness is 3.5 μm. Fig. 2.7 also shows the surface roughness vs. the limiting field in the experiment. It has a hysteresis: the EP 100 μm at step 5 should improve the roughness to less than 1 μm for most assumptions of the initial roughness, which is enough to reach a high gradient $>$ 30 MV/m but in reality, the gradient is still limited $<$ 30 MV/m. It is apparent that from step 4 to 5, the roughness improves a lot by EP, while the maximum field does not improve so much; from step 5 to 6, the roughness does not change much while the maximum gradient increases from 26 MV/m to about 36 MV/m. This fact suggests there is something in addition to surface roughness that is causing BCP'ed cavity HQFS.

When getting a little ahead, the improvement from step 5 to step 6 can be explained if the cause of HFQS is nitrogen contamination by the nitric acid in the BCP acid, as will be shown later in detail. The contamination was accumulating (primarily through grain-boundaries) during multiple BCP, and 100 μm EP in step 5 is not enough to remove them all.

2.4.2 HFQS of BCP'ed Large-grain Cavity

BCP has preferential etching on grain-boundary steps. During the BCP process, surface inside the grain is getting smoother while the gain boundary step difference is getting larger. The grain size of fine-grain cavities is $\sim$ 50 μm [95]. Surface roughness is usually measured by a needle scanning a 0.8 mm width, so the measured surface roughness with fine-grain Nb materials combines topography in the grain and on grain-boundary step.

To date, large-grain niobium sheets are available by directly slicing large-grain Nb ingot. The grain size is on several cm scales. The measured BCP finishing surface roughness is $\sim$ 0.1 μm, it is very smooth (lower than EP $\sim$ 0.5 μm) and even mirror-like. Measurements of large-grain surface roughness count the roughness in the grain only, because the grain size is beyond measurement range.

Considering the BCP polishing property, the smoothness of large-grain niobium is because there are much fewer grain-boundaries, while the roughness in the grain doesn't change much.

Fig. 2.8 shows a comparison of the cavity performance between BCP fine-grain and large-grain

Figure 2.8: Comparison of quality factor behaviors at high gradients between the Large-grain (LG) and Fine-grain (FG) cavities by BCP with baking. [96]

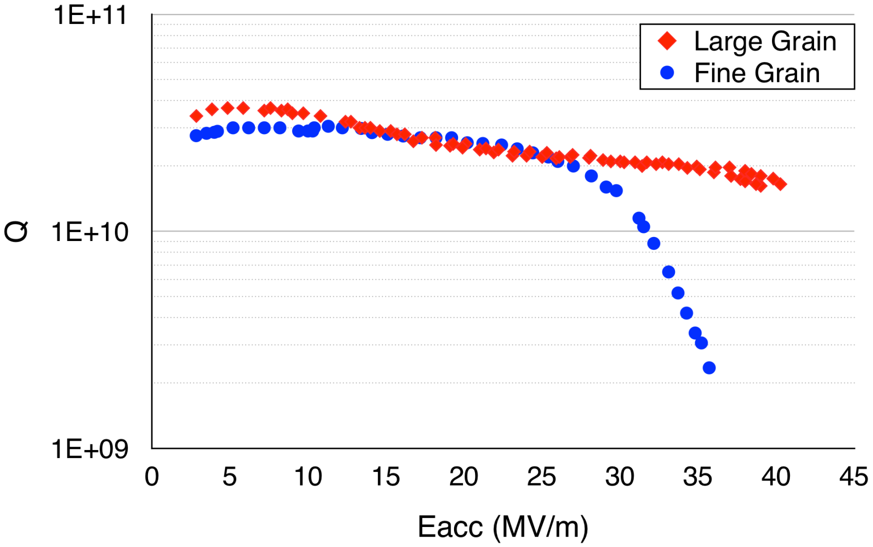

cavities [96]. The onset of BCP HFQS is pushed up to > 40 MV/m, higher than that of fine-grain cavities. This is a rare case with BCP'ed large-grain cavity, even large-grain cavities mostly the gradient is limited lower than 40 MV/m with flat Q_0 (see Fig. 2.9). The gradient is limited by flat Q is different from fine-grain cavities. The fine-grain cavity is limited Q-drop, as seen in Fig. 2.8. This experiment shows less grain-boundary steps give much better performance, or more grain-boundary steps give a worse performance, thus indicating the grain-boundary is firstly responsible for the BCP HQFS. The surface roughness in the grain (micro-roughness) is ruled out as a cause of BCP HFQS by this experimental result.

2.4.3 BCP after EP with Large-grain Cavity

DESY investigated the BCP impact post EP for large-grain cavity [97]. Fig. 2.9 shows the result. BCP (50 μm removal) degrades the high gradient performance remarkably and is similar to the BCP fine-grain cavities. In the Fig. 2.8, the LBT post-BCP could perfectly eliminate the HFQS. So we emphasized the first responsibility of the HFQS with BCP'ed cavities could be in grain-

Figure 2.9: Q vs E of DESY large-grain TESLA (ILC shape, B_p/E_{acc} = 4.26 mT/[MV/m]) cavity treated with EP and an additional 50 μm of BCP. Both results are after baking. (Courtesy of DESY & JLab) [97]

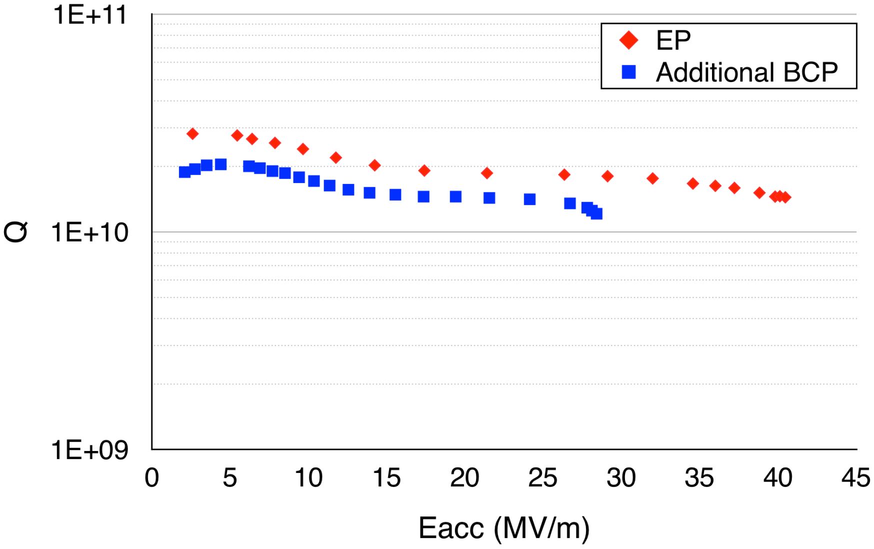

boundaries. One will notice in Fig. 2.9 that the behavior of the field limitation is changed from a remarkable exponential Q-drop (HFQS) to the rather shape quench. The result in Fig. 2.9 suggests that the problem is still on the grain-boundaries but has less impact on the exponential Q-drop in the large-grain niobium material, or other issues within the crystalline in the large-grain material such as dislocation.

2.4.4 Multiple BCP with Large-grain Cavity

KEK investigated the impact of successive BCP on large-grain cavity [98]. A 1.3 GHz Ichiro shape cavity was mechanically polished inside (~ 80μm by the centrifugal barrel polishing (CBP) to smooth the grain-boundary steps). Note that Ichiro cavity shape has a smaller B_p/E_{acc} ratio (3.56 mT/[MV/m]) compared to the ILC shape (B_p/E_{acc} = 4.26 mT/[MV/m]). After 750 ^{circ}C hydrogen degas annealing for 3 hrs, a bulk etching of 160 μm took place using vertical BCP (V-BCP, BCP in the vertical position with a cavity, conventional BCP in most institutes). The tight loop test took place in total five times removing 30 μm each time by V-BCP (first cycle). In these tests, the LTB is applied post-V-BCP for all measurements. The result is shown in Fig. 2.10. The decreasing of E_{acc} onset of HFQS is observed with increased V-BCP material removal. This result clearly shows that the cause of HFQS is getting more serious with increased material removal by BCP. Two potential causes are considered: 1) the grain-boundaries are still a problem, even for the large-grain material; 2) accumulation of contamination. For potential cause 1), resetting the surface roughness by mechanical grinding might be a useful way.

In the second cycle, the surface topography was reset by CBP, then the tight loop test was repeated by H-BCP. The original experimental goal was to validate that the H-BCP (BCP in the horizontal position with cavity) performance is better than normal V-BCP due to more uniform material removal. Again the degradation of onset HFQS happened for each extra 30 μm BCP, the average of the E_{acc} onset of HFQS (red line) increased compared to the 1st cycle (pink line), but $E_{acc,max}$ average (dark blue line) is lower than the 1st cycle (blue line). The conclusion from these results is that resetting surface roughness does not work to improve the HFQS for $E_{acc,max}$, which suggests lowering the (macro) surface roughness does not sufficiently increase the BCP maximum gradient.

Temperature map result for a large-grain cavity also shows that there is no preferential heating on the grain-boundary area [99], where the high roughness region is mainly located. The before and after baking temperature map shows the reducing of the heating area is not located in the grain-boundary area, either (Fig. 2.11). The Q Vs E_{acc} result for before and after-LTB is shown in Fig. 2.12, where the Q improvement is from the LTB.

2.4.5 BCP with Single-crystal Cavity

single-crystal cavity can completely rule out concern of the topographic issue with BCP HFQS, which has no grain-boundaries and can attain 0.1 μm scale very smooth surface even by BCP. To date, single-crystal niobium sheets are available via directly slicing the ingot with very large-grain at 15 - 30 cm scale. Cavities half cups are assembled by electron beam welding (EBW); however, it

Figure 2.10: KEK E_{acc} vs Increasing BCP amount results, first round and second round. All results were taken after LTB.

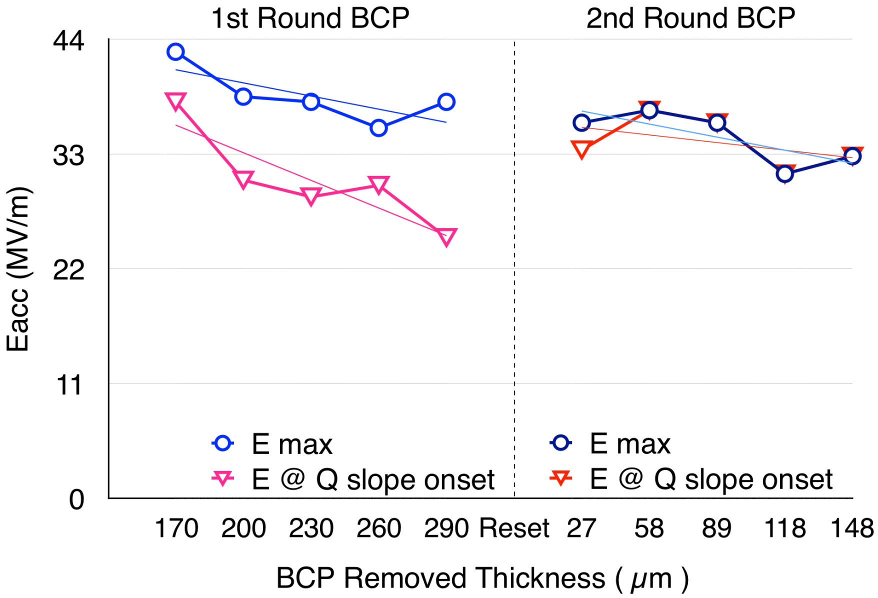

Figure 2.11: Temperature map for a cavity before LTB at 110 mT (left) and after 100 °C baking at 130 mT. No. 10 correspons to the thermometer located around equator. [99]

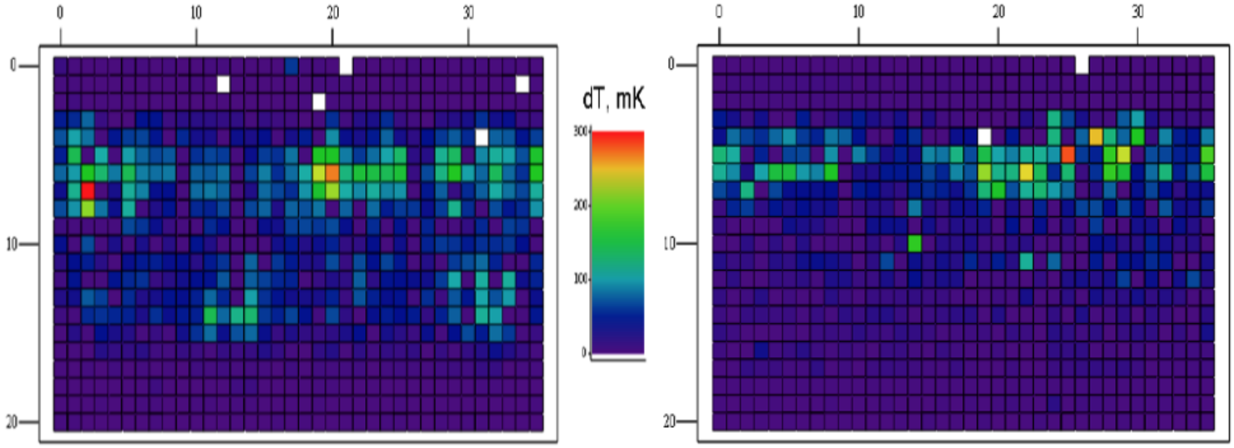

Figure 2.12: Q Vs E_{acc} for the cavity that shown temperature map in Fig. 2.11. [99]

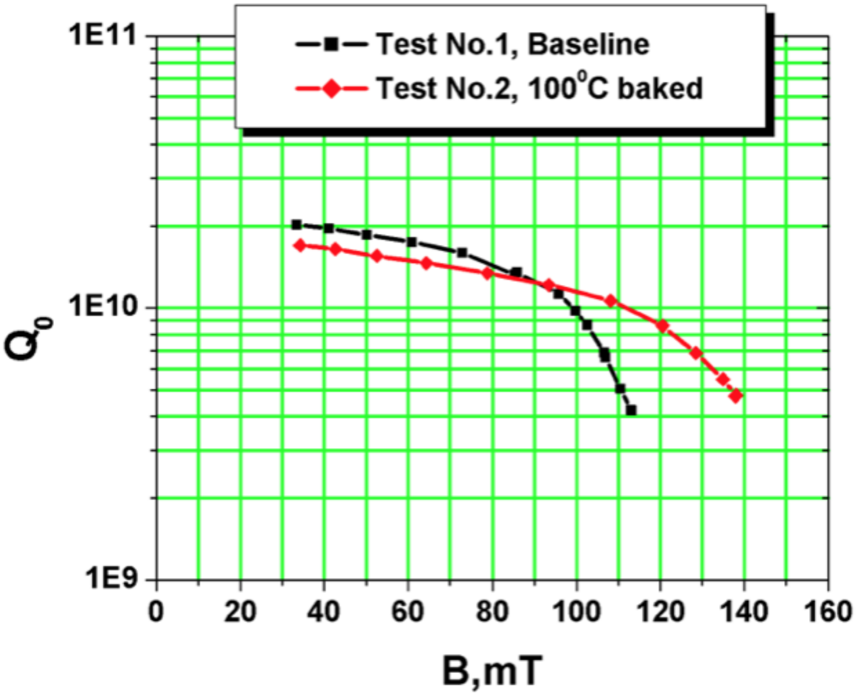

does not produce any grains if the crystal orientation is arranged with the two half cups [94]. So we can fabricate the entire interior cavity surface with a single-crystal. P. Kneisel fabricated a 2.2 GHz single-crystal Low Loss-ILC shape cavity cutting out single-crystal sheets from the large gain ingot (CBMM material), treated it with BCP plus baking and investigated the performance [100]. The result is shown in Fig. 2.13 red curve. We found that combining BCP and LTB for single-crystal cavity, the HFQS disappeared like standard EP cavities, while the maximum gradient is still below the fundamental limit. The LTB eliminates the HFQS, but field gradient still limited ~ 45 MV/m (160 mT) and did not reach the fundamental field limit (~ 180 mT), unlike EP'ed cavities. The limitation behavior is changed from the exponential Q-drop to a sharp quench. Originally HFQS was defined by exponential Q-drop behavior. However, here we regard as that the sharp quench also produced by the same cause as the HFQS. Above the result with 2.2 GHz single-crystalline cavity. This fact provides direct evidence to rule out the topography as a major cause of BCP HFQS.

A nearly single-crystal 1.5 GHz High Gradient shape cavity shows a similar conclusion. This cavity was fabricated with an Nb ingot that has a ~ 20 cm diameter grain in the center and several

Figure 2.13: Q vs E of the 1.5 GHz High Gradient (HG, blue curve, B_p/E_{acc} is 4.47 mT/(MV/m)) shape and 2.2 GHz Low Loss-ILC (LL-ILC, red curve, B_p/E_{acc} is 3.56 mT/(MV/m)) shape single-crystal (SC) Cavities treated by BCP. Both results are after baking. (Courtesy of JLab) [100, 101]

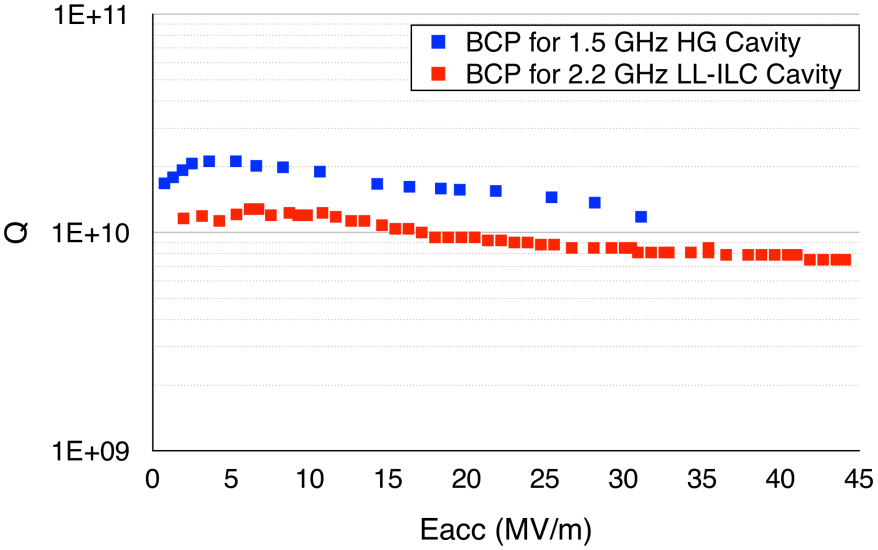

small grains ~ 1 cm. It is treated with BCP plus LTB , with a very smooth surface on most of the cavity. The field limit is 143 mT, as shown in Fig. 2.13 blue curve.

This evidence shows that even the limitation behavior changed, BCP cannot reach the fundamental field limit like EP and suggests there is still something else limiting the gradient in BCP.

The same experiment took place for 1.3 GHz ILC type single-cell cavity fabricated at DESY [102]. Heraeus produced the single-crystal sheets. Fig. 2.14 blue curve shows the result of BCP (112 μm and 120 °C bake for 6 hours). Q curve is very flat up to the gradient limit. The gradient is limited by 37.5 MV/m (~ 160 mT) which is close but still below the fundamental limit 180 mT.

One crucial fact is that this performance is worse than the DESY large-grain TESLA (ILC shape) cavity treated with EP in Fig. 2.9, which has a maximum gradient of 40.5 MV/m (~ 173 mT). This goes against the common understanding: single-crystal cavity, even treated with BCP, has a very smooth surface and better thermal conductivity, so it should have better performance than

Figure 2.14: Q vs E DESY single-crystal TESLA (ILC shape, $B_p/E_{acc} = 4.26$ mT/[MV/m]) cavities treated with BCP: before post-purification [102] in blue curve; after post-purification in red curve. Both results are after baking. (Courtesy of DESY & JLab) [103]

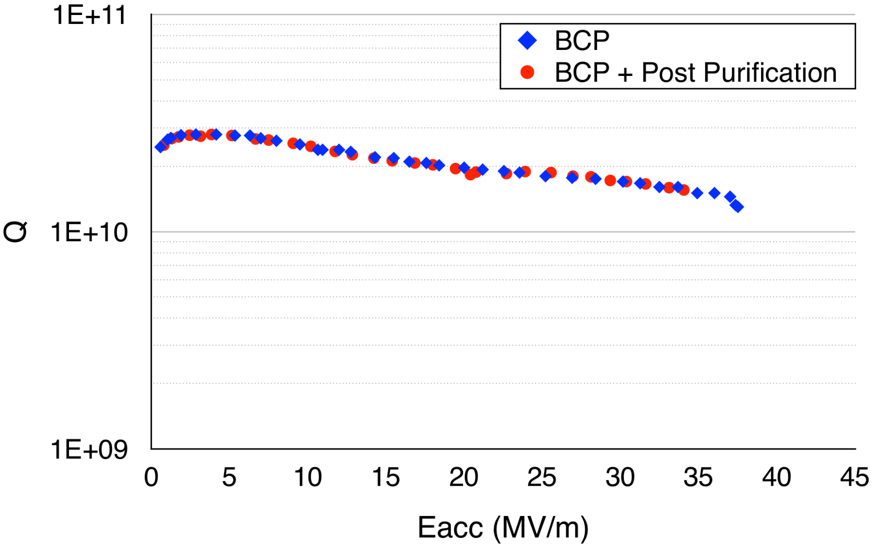

Table 2.2: Main differences between EP & BCP

	EP	BCP
R_z (μm)	0.5	2
Grain-boundary Prefer Etching	No	Yes
Contamination	H, F, O, C, S	H, F, O, C, N, P

large-grain cavity. This indicates the surface roughness itself cannot explain all the performance degradation.

Post-purification was also tested for this cavity. The result is shown in Fig. 2.14 red curve. After the post-purification, the cavity was BCP'ed and took 120 °C bake for 12 hrs. This process does not improve the field limit. The performance failed to improve even with reduced stress or improved dislocation on the SRF surface by post-purification. This also suggests that BCP still contains other issues.

2.4.6 EP & BCP Difference

By the above data mining, we can conclude that the topographic character of the SRF surface produced by the BCP polishing feature is not the only cause of the HFQS with BCP'ed cavities. Therefore, we need to look for other causes.

This chapter focuses on finding why BCP cannot get enough improvement as EP from LTB, so we may only focus on the differences between those two methods. As shown in Table 2.2, EP and BCP difference: roughness (discussed before and ruled out) and potential contamination (H, O, C, and S for EP; H, O, C, N and P for BCP). F from HF is proved not harmful for cavity performance, and P in phosphoric acid has never been reported to react with Nb. Then the only contamination difference is N and S. S problems in EP were discussed in several papers and solved; therefore, N becomes the only potential contamination that causes worse performance in BCP. It is well known that nitrogen reacts with Niobium and generates niobium nitride.

2.4.7 Nitrogen Diffusion Calculation for the Same Condition with LTB

Fick's second law predicts how diffusion causes the concentration to change with time. It is a partial differential equation which is one dimension reads:

$$\frac{\partial c}{\partial t} = D\frac{\partial^2 c}{\partial x^2}, \tag{2.3}$$

c is the concentration in dimensions (example: in mol/m^3), $c = c(x,t)$ is a function that depends on location x and time t [104]. A simple case of diffusion with time t in one dimension (taken as the x-axis) from a boundary located at position x = 0, where the concentration is maintained at a value c_0 is

$$c(x,t) = c_0\text{erfc}(\frac{x}{r}), \tag{2.4}$$

where erfc is the complementary error function, r is the Diffusion Distance and defined as r = $2\sqrt{Dt}$, D is the diffusion coefficient (or Diffusivity) in dimensions (example m^2/s) define as:

$$D = D_0\exp(-\frac{E_a}{k_B T}), \tag{2.5}$$

Table 2.3: Diffusion parameters for the interstitial elements N and O in Nb [105].

Interstitial Element	Temperature Range (°C)	Frequency Factor D_0 (cm^2/s)	Atomic Activation Energy E_a (eV)	Diffusivity D (cm^2/s)
Oxygen	40 - 150	2.0×10^{-2}	1.17	3.0×10^{-21} - 2.3×10^{-16}
	150	1.5×10^{-2}	1.20	7.7×10^{-17}
Nitrogen	150 - 300	8.6×10^{-3}	1.51	8.9×10^{-21} - 4.5×10^{-16}
	300	9.8×10^{-2}	1.65	3.0×10^{-16}
Carbon	130 - 280	4.0×10^{-3}	1.43	5.3×10^{-21} - 3.7×10^{-16}
	150	1.5×10^{-2}	1.15	3.0×10^{-16}

where $k_B = 8.6173324 \times 10^{-5} eV/K$ is the Boltzmann's constant, T is the absolute temperature, E_a is the atomic activation energy, D_0 is the frequency factor, these parameters are shown in Table 2.3, the Diffusivity are calculated from Eq. 2.5 with the corresponding temperature shown in the same table.

At 150 °C, D_O is 7.7×10^{-17} and D_N is 8.9×10^{-21}, so if the diffusion time t is 40 hours, the Diffusion Distance for oxygen is 66 nm, while for nitrogen the Diffusion Distance is only 0.71 nm. This means during the LTB process oxygen diffuse to the distance similar/longer than the London Penetration Depth while nitrogen still stays on the surface. This agrees with our nitrogen contamination induce HFQS assumption that low-temperature baking can fully recover the EP cavities, but only partially improve BCP cavity performance because nitrogen contamination still exists on the RF surface.

Our diffusion case is more close to a"thin-film" problem that the thin film is initially located at x = 0:

$$c(x,t) = \frac{N}{\sqrt{\pi} r} e^{-x^2/r^2}, \tag{2.6}$$

where N is the number of "source" atoms per unit area initially placed at x = 0, r is the Diffusion Distance, same as in Eq.2.4.

2.4.8 Nitrogen Contamination

Our first attention to the nitrogen contamination was the gas exposure test on the fresh SRF surface just after the vertical test, without vacuum break before the gas exposure [106]. We found that Argon

Figure 2.15: A comparison of diffusion concentration for nitrogen (left) and oxygen (right) on niobium surface (with different x-axis scale), calculated from Eq. 2.6 with t = 40 hrs and T = 150 °C.

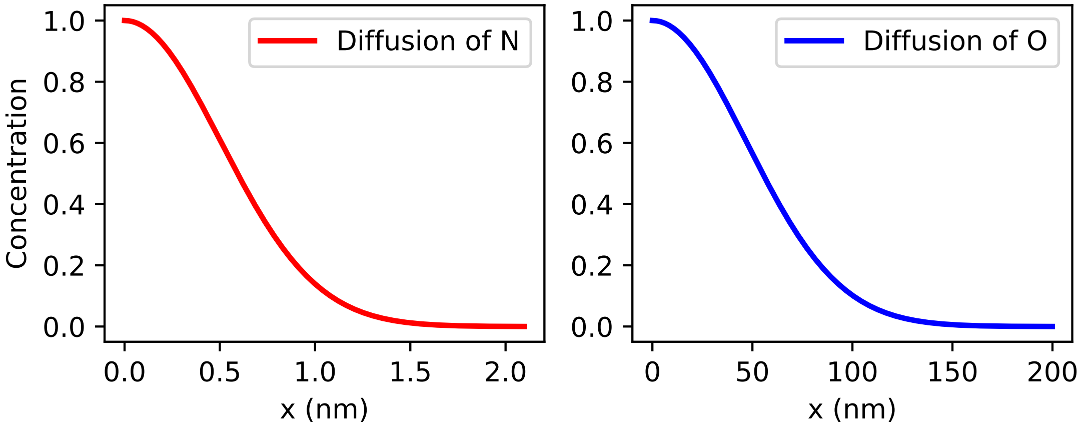

gas usually exposure has no performance degradation, but pure nitrogen gas exposure produces a remarkable Q degradation, as shown in Fig. 2.16. In this case, the low temperature (70 °C) bake even lower than 120 °C seems an effective cure. We also notice that a similar experiment shows the opposite result: exposing Nb cavity to Nitrogen gas for three days has no degradation observed in their case [107].

Our hypothesis that nitrogen contamination produces the HFQS is first corroborated by the experimental results summarized in Fig. 2.17. This experiment was originally done for the development of hydrogen-free EP [108]. Adding nitric acid (HNO_3) of (61% w/w) 1500 ppm into the EP acid (48% HF: 93% H_2SO_4 = 1: 10 V/V) was very effective to prevent hydrogen doping during EP. However, unlike the normal EP case, the HFQS still exists even after baking. The only difference between these two processes (normal EP and new EP used EP acid added HNO_3) is the small amount of the nitric acid so that we think the N contamination gives this degrading of the cavity field limit.

The second decisive evidence is in the recent nitrogen doping study. FNAL has successfully developed the nitrogen doping method to increase Q of SRF Nb cavities [109]. They put nitrogen gas into the vacuum furnace at 800 - 900 °C vacuum annealing to contaminate the surface. They proved that only the interstitial nitrogen in the niobium contributes to enhancing the Q because it shortens the mean free path. During the doping process, niobium-nitride metal phase (Nb_xN_y) is also generated on the top surface. This has to be removed by several microns of electropolishing; otherwise remarkable field limit happens. Later, low temperature (~ 120°C) nitrogen infusion was developed [110]. The cavities treated with this method have a much higher maximum gradient; in the meantime, niobium nitride does not exist. This further indicates nitrogen contamination (especially niobium nitride) lowers the gradient.

Thirdly, KEK experiment with stepwise BCP and reset (Fig. 2.10) indicates that, if the HFQS is attributed to N contamination, the CBP before second experiment cycle only resets the roughness but does not remove all the contamination, or BCP after CBP already produced deeper N contamination, and this explains the degradation of the reachable gradient.

Finally, the KEK experiment with multiple EP followed by BCP and then more EP (Fig. 2.6) also agree with this assumption. After the step 5, 100 μm EP removal for Nb is sufficient for recover the roughness to less than 1 μm; however, it is not enough to remove the contamination in the deep site, so the maximum gradient is limited to only ~ 26 MV/m.

While after step 6, even though the roughness does not change much, it removes 50 μm more Nb, which contains most N contamination. Therefore, the $E_{acc,max}$ increased a lot and is close to the original result, ~ 37 MV/m.

2.4.9 Generation of Nitrogen Contamination and observation

During nitrogen doping, Nb_xN_y starts to generate at temperature ~ 400 °C ([112], is 673 K, corresponds to 0.058 eV). Nb_xN_y, which has a very low thermal conductivity (1/10 of Nb at low temperature), is harmful to cavity performance and could be the reason for low E_{acc} and HFQS. While the low temperature (120 °C) infusion does not form Nb_xN_y so this can produce high gradient and high Q cavity performance [109].

We can then assume that if Nb_xN_y can be generated on Nb surface on BCP, it can cause HFQS.

Figure 2.16: KEK cavity performance degradation with nitrogen exposure [106]

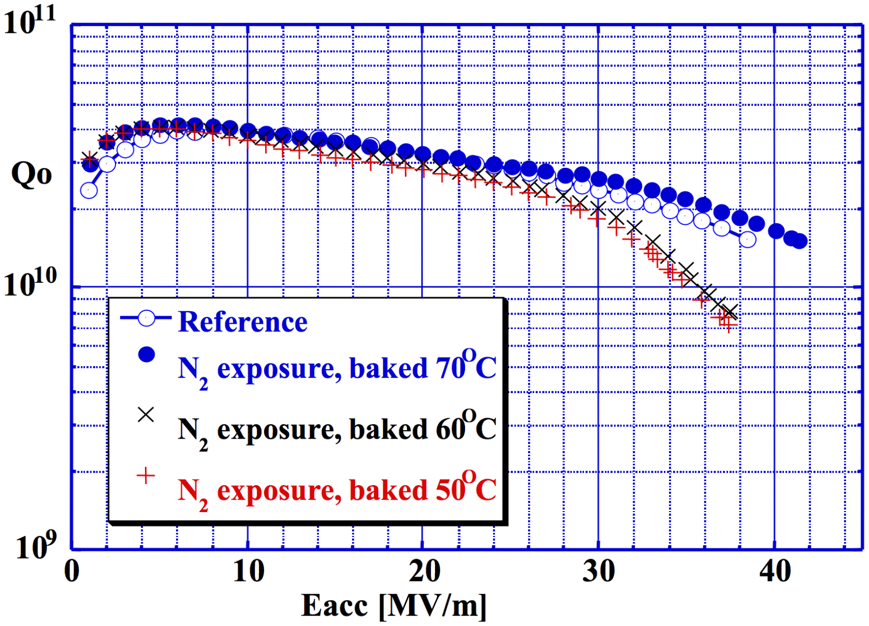

Figure 2.17: Q vs E for KEK fine-grain Type A cavity, blue cross curve is an example for normal EP cavity performance [77], red circle curve is the cavity dealer with EP plus one drop of nitric acid [111]. Both cavities was applied baking after EP.

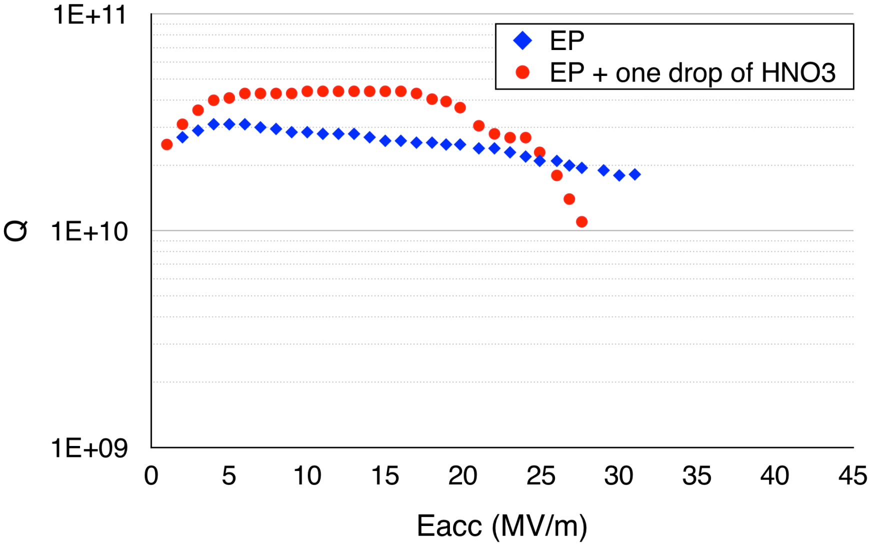

Figure 2.18: Reaction speed vs 1/T for different BCP ratio. [113]

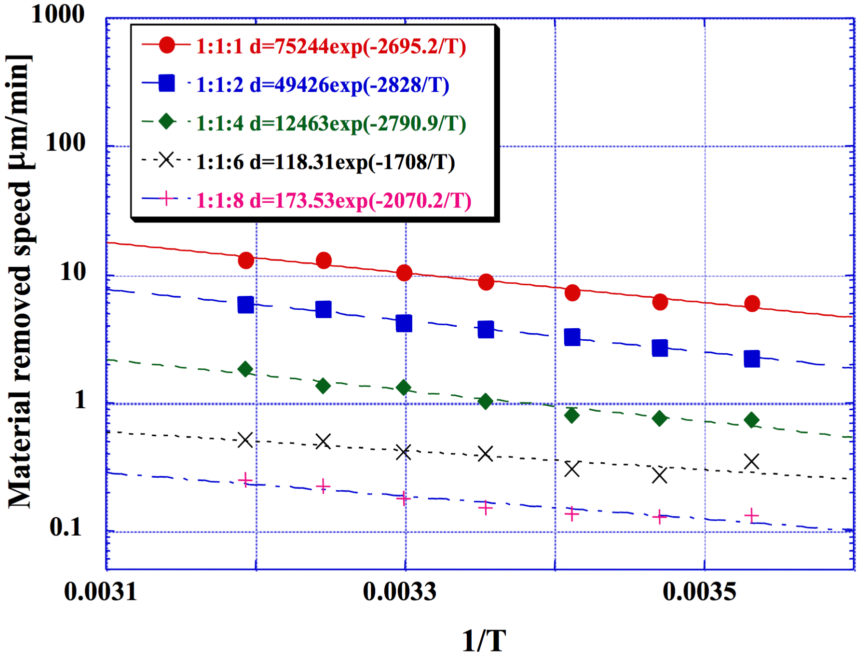

The reaction energy of BCP is estimated by measuring the temperature dependence of the polishing rate [113]. The result is shown in Fig. 2.18. The results are well fit by the Arrhenius equation:

$$d(T) = d_0 \exp(-\frac{Q}{k_B T}) \tag{2.7}$$

The constant value of 2695.2 for the BCP acid composition HF: HNO_3: H_3PO_4 = 1: 1: 1 (V/V) corresponds to 0.232 eV (~ 2419 °C). Nb_xN_y can form (but with very low probability reaction) by the nitric acid reacting with niobium in such energy. JLAB has observed nitrogen by SIMS on BCP'ed niobium sample [114]. Nitrogen element mostly stays on the surface 0.05 μm. On the other hand, FNAL showed that interstitial nitrogen and Nb_xN_y phase lie at different depths on niobium top surface. Nb_xN_y mostly resides on the surface within 2 μm [115]. These indicate the niobium contamination on Nb top surface by BCP is in Nb_xN_y phase.

We discussed in Eq. 2.1 and Eq. 2.2 that the low thermal conductivity could cause R_s increasing, where the $\kappa_{\mathrm{Nb2O5}} \sim 1$ W/(m·K) and the Kapitza resistance between Nb and Nb_2O_5 is 0.05 (m^2K)/W. For niobium nitride, $\kappa_{\mathrm{NbxNy}} \sim 1$ W/(m·K) and the Kapitza resistance between Nb and NbxNy is

0.9×10^{-5} (m^2K)/W [116].

2.5 Conclusion

HFQS with BCP'ed cavities is not perfectly removed by the LTB, unlike EP'ed cavities. There is no common consensus on the mechanism of the HFQS in BCP'ed cavities to date. We mined past data on fine-grain, large-grain and single-crystal cavities to show inconsistencies in previous explanations, and developed a new model for the root cause of the BCP HFQS. This model says that the nitrogen contamination, especially niobium–nitride phase (Nb_xN_y) is the remain cause of the HFQS BCP'ed cavities. The niobium-nitride phase is generated by the reaction between niobium and the nitrogen from the decomposed nitric acid in the BCP reaction. Nitrogen in niobium-nitride phase does not move by the LTB; thus, the HFQS is not recovered by the LTB. Not only does the nitrogen contamination model agree with all experimental data sets, it also offers coherent explanations for previously unresolved phenomena in circumstances including: (1) applying multiple BCP post EP (Fig. 2.6 and Fig. 2.7); (2) adding HNO_3 to EP (Fig. 2.17); and (3) maximum field of BCP single-crystal cavities (Fig. 2.13 and Fig. 2.14) lower than EP large-grain cavity (Fig. 2.9). These results provide evidence for our model and inspire us to develop a new acid that can solve this HFQS problem.

CHAPTER 3

NEW ACID: ACID DEVELOPMENT

In our previous data analysis in the last chapter, we concluded that the potential root cause could be nitrogen contamination on the surface. The nitric contamination could be created by nitric acid during BCP which uses the mixture of hydrofluoric acid (HF), nitric acid (HNO_3), and phosphoric acid (H_3PO_4). Based on this thought, we started to develop a new chemical polishing acid that replaces the nitric acid by another N-free oxidizer, such as hydrogen peroxide.

3.1 Acid Component

As we introduced in chapter 1, general idea and mechanism of chemistry polishing (non-electrical and electrical) is to continuously oxidize the metal and remove the oxide layer by HF, to refresh the metal surface. So we need to choose a strong enough oxidizer, and oxide layer remover. We then try to find a replacement acid, which should be consist of both of these functions.

3.1.1 Oxide Layer Remover

HF is a weak acid but can dissolve niobium oxide very effectively, and there are only two component elements. The acid strength refers to the tendency of an acid, symbolized by the chemical formula HA, to dissociate into a proton, H^+, and an anion, A^-. The dissociation of a strong acid in solution is effectively complete, except in its most concentrated solutions. There is no motive to replace the HF, so we only change the oxidizer HNO_3 in the conventional acid.

The reaction of HF with Niobium oxide is

$$Nb_2O_5 + 10\,HF \longrightarrow 2\,NbF_5 + 5\,H_2O. \tag{3.1}$$

Table 3.1: Oxidization power comparison for some normal oxidizer

Potential Range	Oxidizer	Standard electrode potential (V)
E < 0.77V	Diluted H_2SO_4	0.17
	Cu^{2+}	0.341
	Cu^+	0.52
0.77 V < E < 1.23 V	Fe^{3+}	0.77
	Ag^+	0.8
	H_2SO_4	0.9, 1.1 when heated
	Diluted HNO_3	0.96
	HNO_2	0.983
	HNO_3	1.1
1.23 V < E < 1.83 V	O_2	1.23
	Cl_2	1.358
	$HClO_3$	1.47
	Au^{3+}	1.5
	Pb^{4+}	1.691
	Au^+	1.692
	H_2O_2	1.776
E > 1.83 V	Ag^{2+}	1.98
	O_3	2.076
	O	2.694
	F_2	2.866

3.1.2 Oxidizer Choosing

Table 3.1 shows some normal oxidizer and their standard electrode potential, which indicate their oxidization power. H_2SO_4 is used in EP acid, which needs to add electrodes to make the reaction happen; thus, we need an oxidizer stronger than that (0.9 V). Table 3.1 shows the HNO_3 has a standard electrode potential of 1.1 V, so the new acid should have similar or higher value than that.

Based on our previous analysis conclusion Chap. 2, the new acid should have no nitrogen element, and it better be no introducing other potential contamination elements, so H_2O_2 with the standard electrode potential equals to 1.776 V, should be the best choice. It is a strong oxidizer that consists of simple elements, with low price and no pollution to the environment after waste acid treatment. We decide to choose H_2O_2 mixing with HF as the promising new etching acid for niobium cavity. This kind of acid mixture is already utilized for the treatment of engine parts made of iron in the automotive industries.

3.1.3 Record on This Acid

We found two studies with this acid mixture. One was in the early 1980s to resolve the issue in wastewater treatment in the conventional BCP acid [117] because HNO_3 has an issue with the wastewater treatment. This mixture of HF and H_2O_2 was unstable, and the resultant polished surface was not smooth. They concluded it was due to the higher water content. This acid was not applied.

The second one was to improve the BCP'ed cavity performance [118] at the end of the 1990s at Saclay, France. They attempted to find an alternative chemical treatment of the conventional BCP, precisely similar to our study, but they had no conscious about the nitrogen contamination with niobium in their study. A various mixture of HF (5 - 15 mol/L) and H2O2 (2.5 - 5 mol/L) was applied to niobium samples. However, the surface was always degraded by severe grain-boundary etching and resulted in significant roughness (mean peak-to-valleys > 50 μm). They did not give an explanation of the mechanism for this rough finishing surface. They gave up to persuade the optimization of this acid. We did not know their experimental results until we started new acid development. This was a fortune for us. If we know earlier, we would not have tried this kind of acid. Later, one will see the difficulty that we also meet, but finally, we have discovered the resolution with this new acid as seen in the Chap. 4.

3.2 Experiments

3.2.1 General Experimental Setup

Before the experiments, niobium samples were cut to 50 mm × 15 mm × 4 mm and were mechanically polished by emery paper to adjust the initial surface roughness. The surface roughness after etching was measured at no fewer than 5 points near the initial measurement points, and the results were averaged. The standard deviation was used to construct the error bar.

To maintain consistency with previous published data sets of superconducting Nb surface, we

Figure 3.1: R$_{p1}$, R$_{p2}$, R$_{p3}$, R$_{p4}$ and R$_{p5}$ are the distances from the mean line (m) to highest 5 peaks in the range of sampled reference length, R$_{v1}$, R$_{v2}$, R$_{v3}$, R$_{v4}$ and R$_{v5}$ are the distances from the mean line (m) to lowest 5 valleys in the range of sampled reference length.

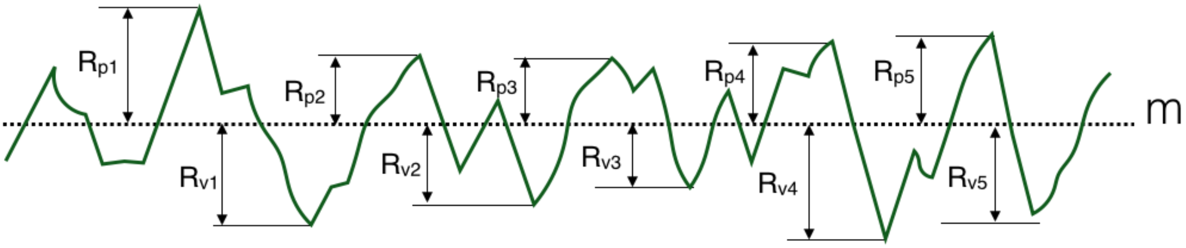

Table 3.2: Preliminary Recipe

RRR of Nb	Initial Temperature	H_2O_2%	H_2O_2 (mL)	HF %	HF (mL)
300	45 °C	35	45	50	10

take R_z as a measure of surface roughness defined by:

$$R_z = \frac{1}{5}\sum_{i=1}^{5}(R_{p,i} - R_{v,i}), \tag{3.2}$$

where $R_{p,i}$ and $R_{v,i}$ denote the i^{th} highest peak and i^{th} lowest valley (Fig. 3.1) within the evaluation length respectively [119]. R_z is directly measured by the stylus (roughness tester, the measurement range is several micrometers).

3.2.2 Preliminary Results

Because of the tight FRIB cavity production schedule and waiting for Job Safety Analysis (JSA) approval for FRIB chemical room use, originally this experiment started in Nomura Plating Ltd, Japan and got a promising preliminary result. The original recipe is shown in Table 3.2. This is based on a study of the automobile industry from Toyota [120, 121]. The result is luckily good, the R$_z$ is ~ 2.5 μm with about 80 μm removal.

I tried several times to reproduce the preliminary result with the same recipe in the Physics department's chemistry room but failed to reproduce the result. All trials have very rough finishing surface, R$_z$ = 8 ~ 9 μ m with only about 20 μm removals.

Figure 3.2: Preliminary results in Nomura Plating. Ltd. Conventional BCP recipe, 5 min reaction, ~ 100 μm removal.

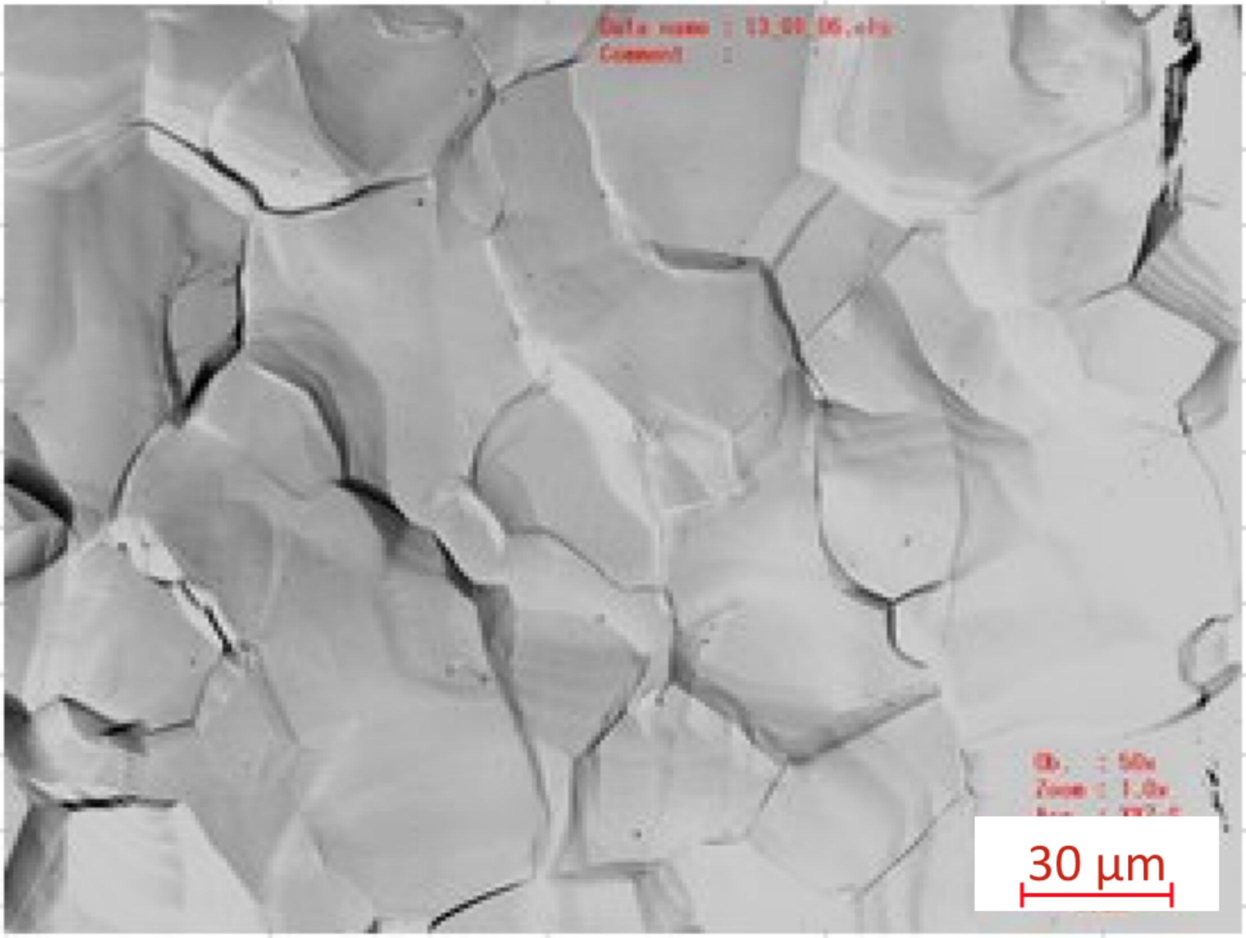

I went to visit Nomura. Ltd Plating to check their recipe step by step, and reproduced their first good results, $R_z \sim 2.5$ μm, similar to BCP (Fig. 3.2), only have some small structures looks like dirt (Fig. 3.3), which need to be solved.

A half-reaction-time experiment was done (the etching time reduced from 60 min to 30 min), to study the formation process of the roughness structure on Nb surface, as shown in Fig. 3.4. However, no visible roughness building process was observed.

We then tried to eliminate those small structures by stirring the acid during the reaction, unlike the original recipe that just put the Nb sample in the acid and watch. Another motive to do the stirring is to reproduce my experiment in the MSU physics department chemistry room, where I always do the stirring during the reaction. The result is shown in Fig. 3.5.

Figure 3.3: Preliminary results in Nomura Plating. Ltd. Original Recipe, 60 min reaction, ~ 80 μm removal.

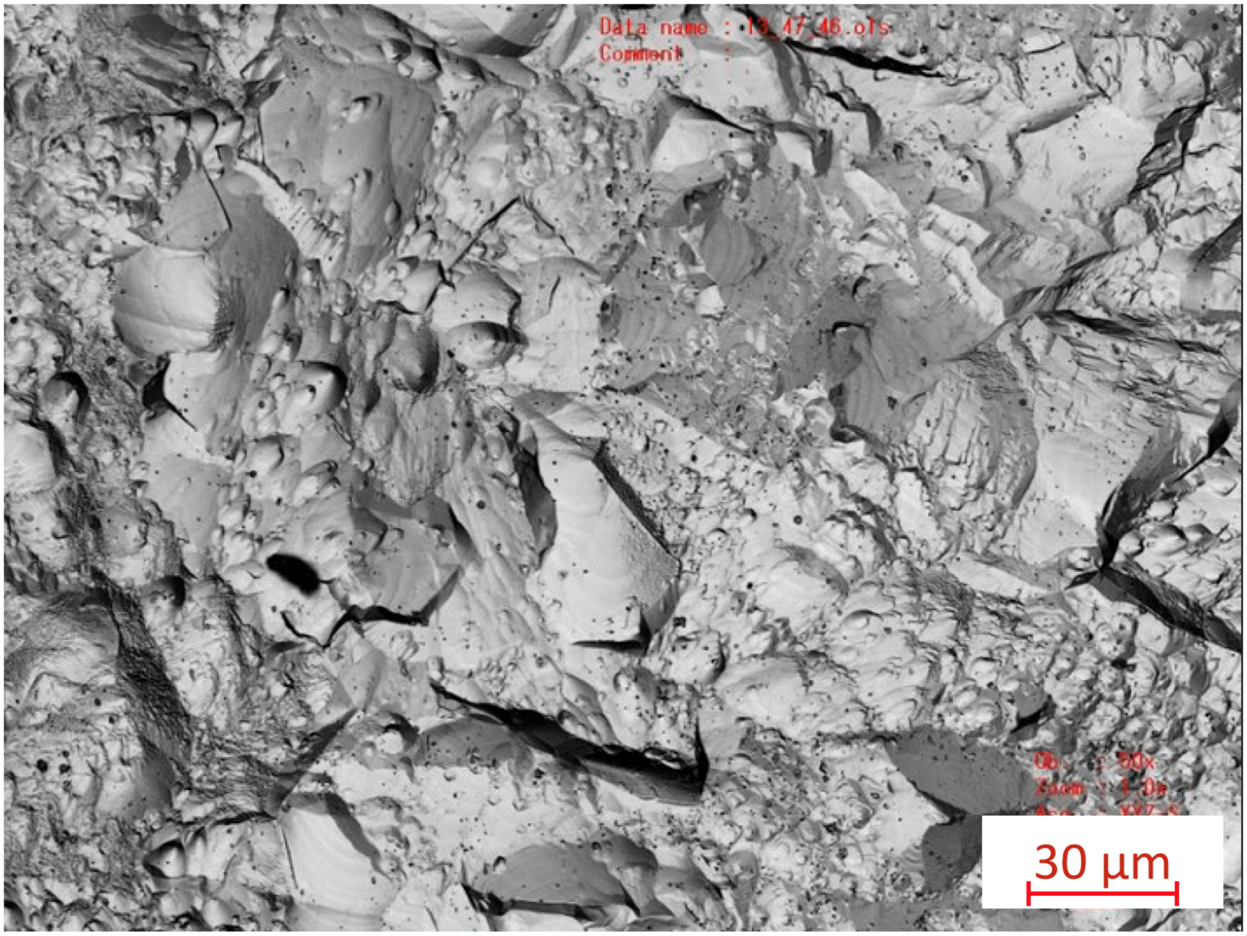

In the stirring case, the structures and dirt somewhat disappear (as shown in Fig. 3.5), but the roughness got very high, 7 ~ 9 μm with the same reaction time (1 hr, removal= 40 μm), similar to my experiment result in MSU physics department's chemical room. We then confirmed that stirring could make the Nb surface rough.

After visiting Nomura plating, I started to try to reproduce their good result without stirring, but to our surprise, we still fail to get their R_z = 2.5 μm results.

We then summarized several other possibilities from comparing the experiment process in two places:

- Acid vibration during temperature control makes finishing surface rough. At first, I was trying to maintain the temperature bath, while the self-made thermostat is not very stable. I

Figure 3.4: Preliminary results in Nomura Plating. Ltd. Original Recipe, 30 min reaction, ~ 40 μm removal.

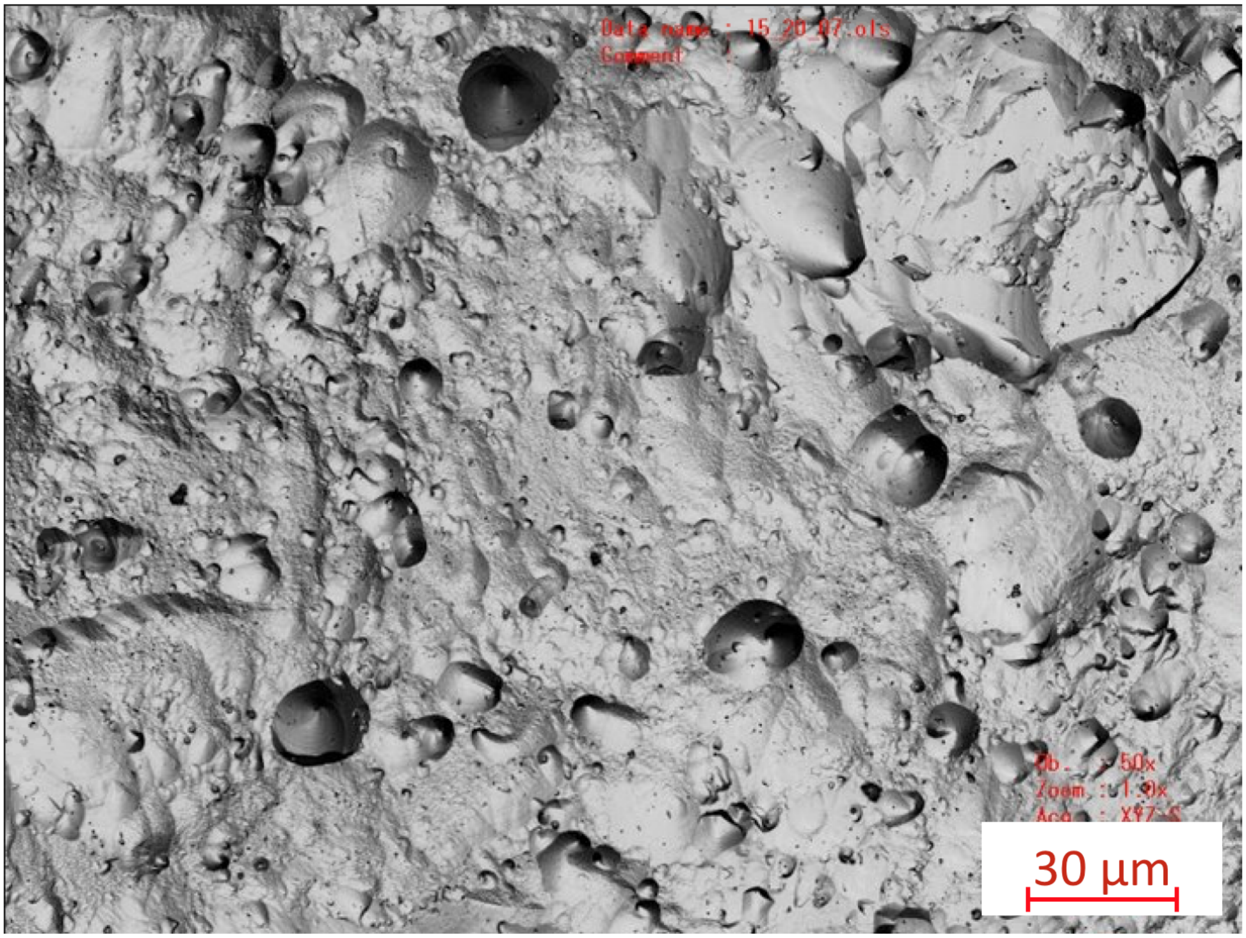

remove the acid beaker (made of polyethylene) out of the bath when the water bath too hot. This moving process may generate vibration during the reaction.

- Reaction speed highly depends on acid temperature.
- Acid temperature may influence the finishing surface. The finishing surface depends on oxide layer formation and removal, which depends on the oxidation and removal reaction speed. The two reactions may have different temperature dependence, and affect the surface roughness.
- Different pre-etching degreaser may influence the finishing surface. The degreasing process in Nomura Plating is another difference from my MSU experiments. There may exist some

Figure 3.5: Preliminary results in Nomura Plating. Ltd, original recipe With stirring, 30 min reaction.

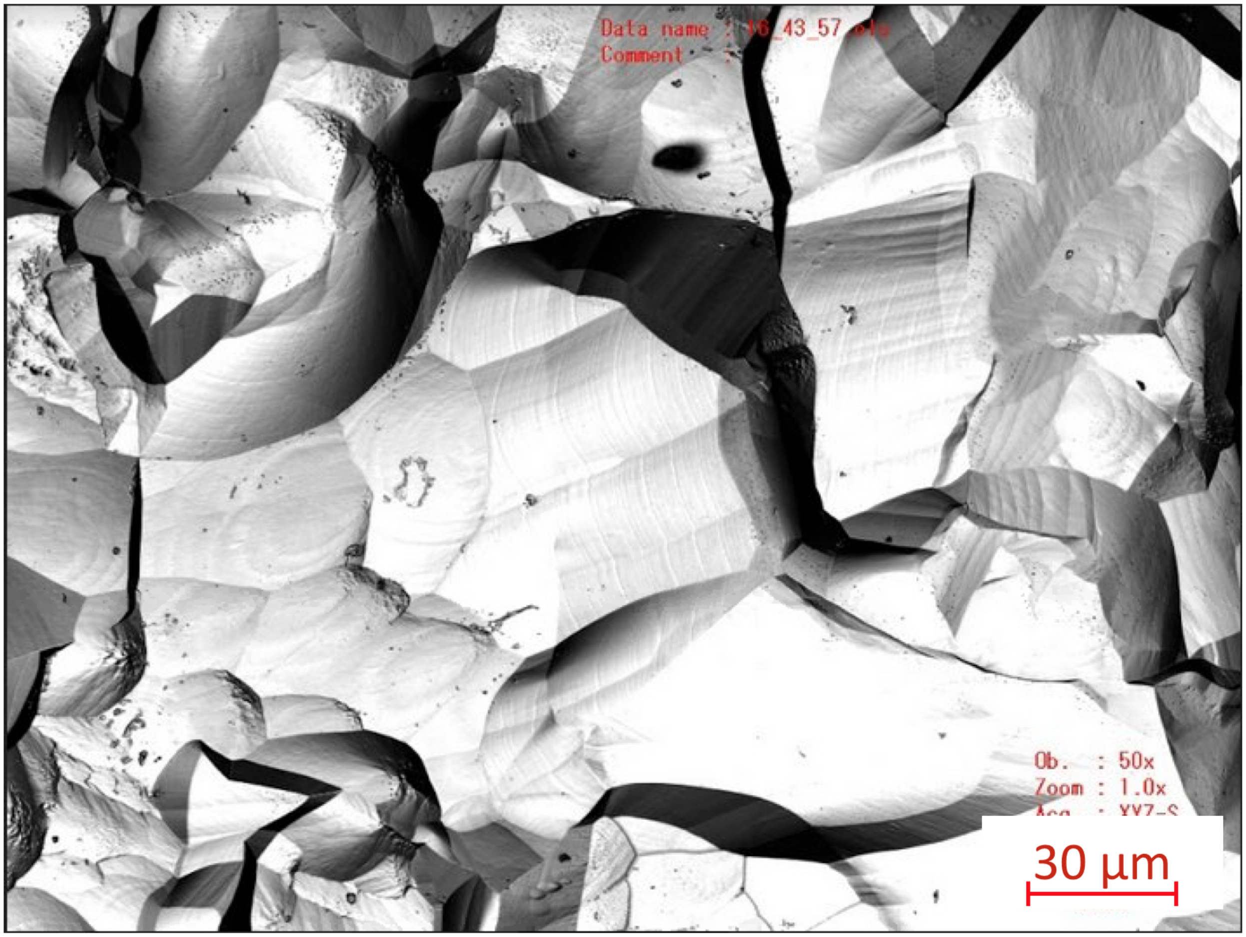

surface process we do not know.

The acid vibration while putting in or removing the beaker from the water bath was ruled out after I did the experiment which I did not move the beaker and tried to make the beaker stay stably.

3.2.3 Degreaser Influence

3.2.3.1 Experiment and Result

To study the degreasing influence, I tried three degreasers: Alconox (MSU physics department sample/container cleanser), Acetone, Micro-90 (FRIB routine cleanser for cavity assembling), and Micro-90 with HF rinsing. Nb samples were immersed in these degreasing solutions with

Table 3.3: Study of degreaser influence on roughness for new Acid. Reaction time is 30 minutes for all cases. R_z is the average value of 10 measured points on each sample, σ_{R_z} is the standard deviations of the measured values.

Method	d (μm)	R_z (μm)	σ_{R_z} (μm)	R'_z (μm)	$\sigma_{R'_z}$ (μm)
Alconox	20.5	6.77	2.58	12.08	2.96
Acetone	12.0	6.32	3.11	10.32	2.48
Micro-90	14.0	6.59	2.10	13.42	2.61
Micro-90 + HF Rinse	23.5	5.58	2.21	11.87	4.46
Micro-90 with Cu accident	93	8.05	2.21	13.85	2.49

Figure 3.6: Experiment set up.

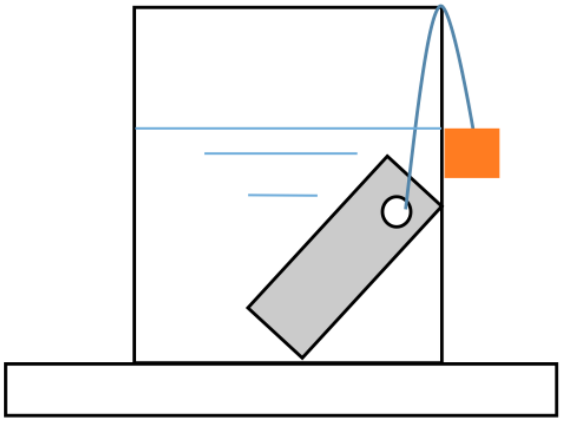

30 minutes ultrasonic, then rinsed with ultrapure water and wipe dry. The same acid recipe was applied to these samples for 30 minutes, and the reaction temperature is 43.7 ± 1.47 °C. The result is shown in Table 3.3.

It is apparent that all finishing roughness R'_z are higher than before reaction, and there is no obvious roughness difference with different degreasing methods. All of the results are far higher than Nomura Plating's $R'_z = 2.5\ \mu$m results.

After trying these possibilities, we still fail to reproduce result in Nomura Plating; then we started to look for the optimization route by controlling parameters systematically.

3.2.3.2 One Accident of Copper Nut Contamination #α

In an experiment to see the Micro-90 degreasing effect on etching result, I accidentally dropped a copper nut (tied to the Nb sample to make it easy to take out of the acid, see Fig. 3.6) into the acid before I put the Nb sample (result in Table 3.3, last term). Massive amount of bubbles were generated. I took the nut out with tweezers after about 30 seconds, the bubbling stopped, and the acid solution became slightly blue, which is the color of copper ion.

The Nb sample (pre-cleaned with Micro-90) was put into this acid mixture and found that colossal bubbling happened again, on the Nb surface. This phenomenon is very different from previous experiments. In all of them, Nb quietly stays in the acid.

The temperature also increased quickly, unlike the other experiments maintain the temperature (43.7 ± 1.47 °C), this case started with ~ 18 °C, reached 27.2 °C in 5 minutes, 33 °C in 10 minutes, 50 °C in 20 minutes and increased to above 90 °C in less than 30 minutes.

The reaction speed is also much higher than the other four cases, maybe partially due to high temperature. This new phenomenon was also studied later, parallel with the main series. This case is named #α for future convenience.

3.2.4 Another Guess: Ratio Based on Reaction Equation

The original acid ratio is the chemical polishing recipe for steel, the reaction is:

$$2\,\mathrm{Fe} + 3\,\mathrm{H_2O_2} \longrightarrow \mathrm{Fe_2O_3} + 3\,\mathrm{H_2O}, \tag{3.3}$$

$$\mathrm{Fe_2O_3} + 12\,\mathrm{HF} \longrightarrow 2\,\mathrm{Fe(HF_2)_3} + 3\,\mathrm{H_2O}. \tag{3.4}$$

The overall reaction is:

$$2\,\mathrm{Fe} + 3\,\mathrm{H_2O_2} + 12\,\mathrm{HF} \longrightarrow 2\,\mathrm{Fe(HF_2)_3} + 6\,\mathrm{H_2O}, \tag{3.5}$$

the H_2O_2 and HF ratio is 1: 4, while for Nb, the reaction is:

$$2\,\mathrm{Nb} + 5\,\mathrm{H_2O_2} + 10\,\mathrm{HF} \longrightarrow 2\,\mathrm{H_2NbOF_5} + 8\,\mathrm{H_2O}, \tag{3.6}$$

or written as

$$2\,\mathrm{Nb} + 5\,\mathrm{H_2O_2} + 10\,\mathrm{HF} \longrightarrow 2\,\mathrm{NbF_5} \cdot \mathrm{H_2O} + 8\,\mathrm{H_2O}, \tag{3.7}$$

and the H_2O_2 and HF ratio is 1: 2.

Figure 3.7: R_z Vs Removal and H_2O_2 Amount, the green bars show previously used 35% concentration, and the red bar is H_2O_2 using 50% result.

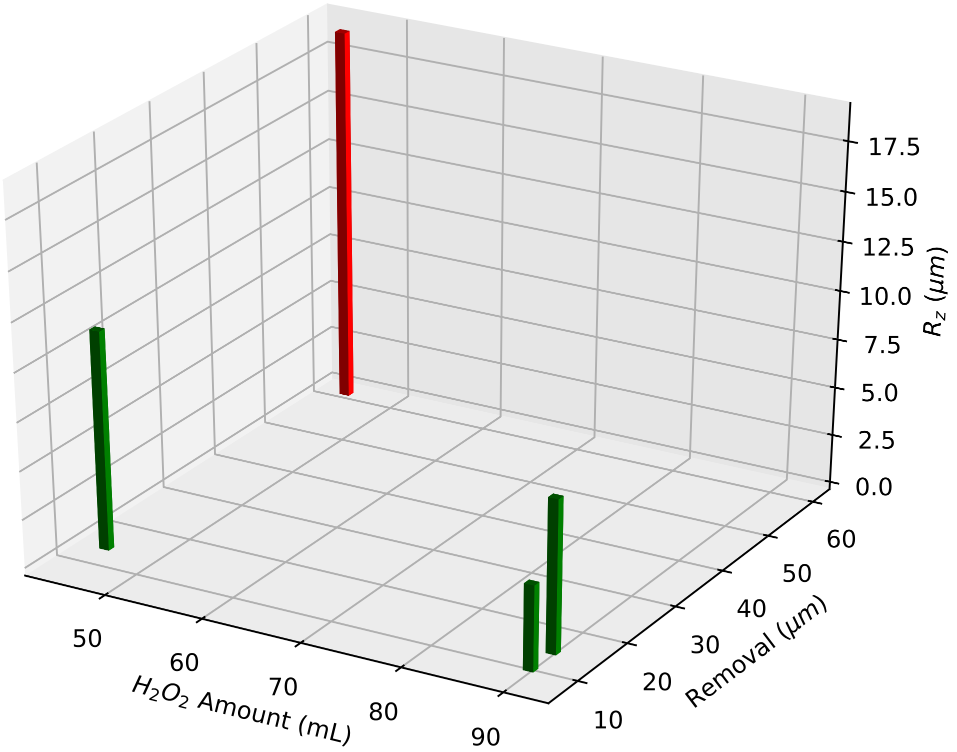

Table 3.4: Double the H_2O_2 amount for new Acid recipe. The 50 %HF amount for all cases are 10 mL, the R_z of Nb samples before reaction is 4.94 μm ± 2.92 μm. Trial 1 reaction starts from room temperature and all others start from 35 °C.

Trial	H_2O_2 (mL)	H_2O_2%	Time (min)	d (μm)	T (°C)	R'_z (μm)	$\sigma_{R'_z}$ (μm)
1	90	35	40	8.0	19.90	4.42	1.45
2	90	35	60	12.5	35.89	7.89	2.94
4	45	35	60	12.0	34.83	11.24	3.56
5	45	50	60	59.0	42.83	18.97	4.90

So we decided to try doubling the H_2O_2 amount based on the reaction difference, to see if there is an improvement.

Figure 3.8: R_z Vs Removal for different H_2O_2 Amount, the green bars show previously used 35% concentration, and the red bar is H_2O_2 using 50% result.

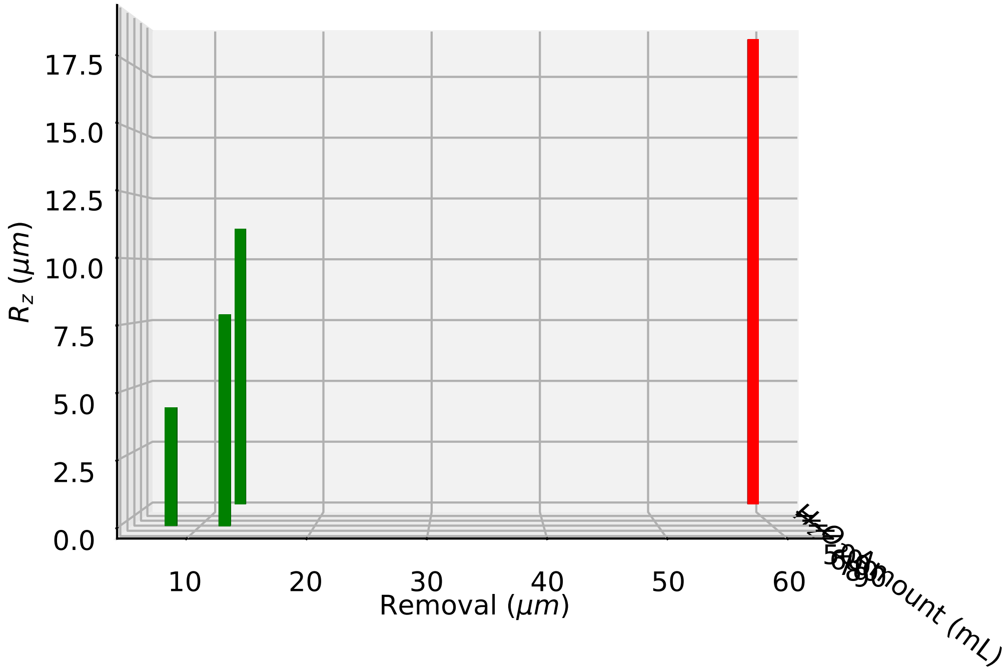

3.2.4.1 Experiment of Acid Ratio Variance

The result is shown in Table 3.4. For trial # 1, the starting temperature was 19.2 °C (room temperature), the reaction speed was too low, only 8 μm in 40 minutes.

All other trials started with a temperature of 35 °C and reacted 60 minutes. The average temperatures for each case during the experiment was shown in Table 3.4. We can get some information from this group of experiments:

- Trial # 2 with doubled H_2O_2 amount has similar removal amount but has lower finishing roughness comparing with trial # 4.
- It has the finishing surface of 7.89 ± 2.94 μm with only 12.5 μm removal but is not enough for our goal (3 μm).
- All 35% cases have very low reaction speed, ~ 0.2 μm/min, much slower than the BCP case.

Figure 3.9: Temperature dependence, removal and roughness. The blue bars shows 4 different temperature cases with the same acid recipe. The red bar is one trial with Cu added in acid before Nb reaction. Standard deviation is about 25% for roughness.

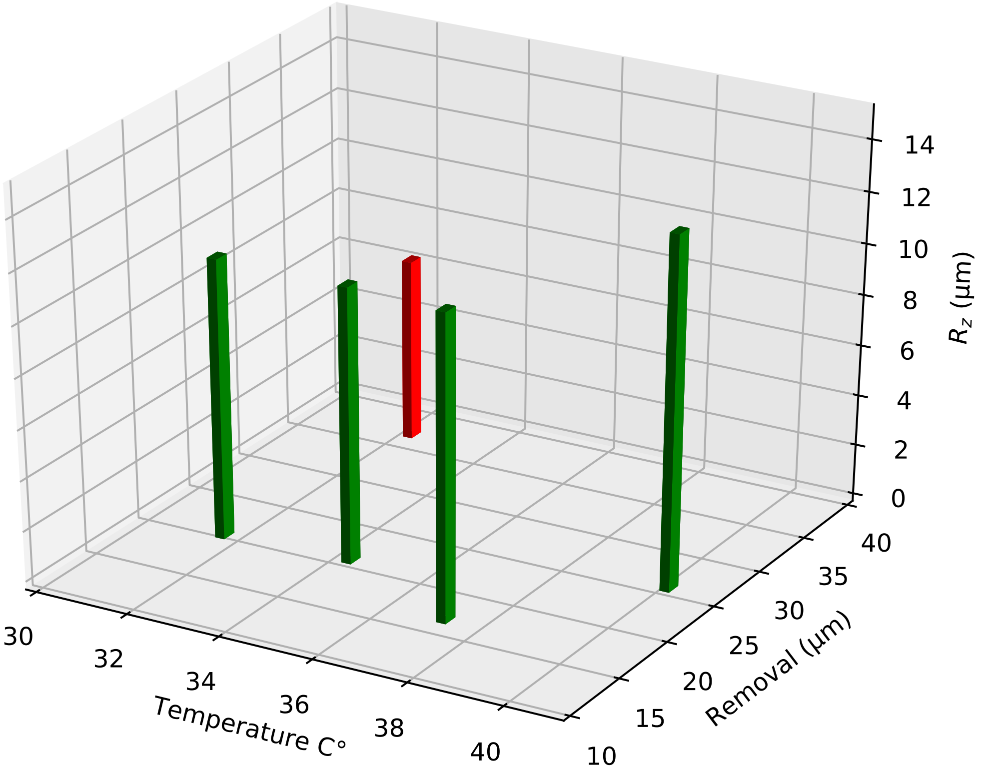

- The 50% case for trial # 5 has much higher (5 times) reaction speed. We may consider using this concentration for the latter experiments to shorten the reaction time and get a more obvious reaction result.

Even we have no firm conclusion in this group of experiments because of low removal, the oxidization Vs removal ratio is an important process parameter. A systematical optimization for acid ratio will be shown later.

Figure 3.10: R_z Vs T

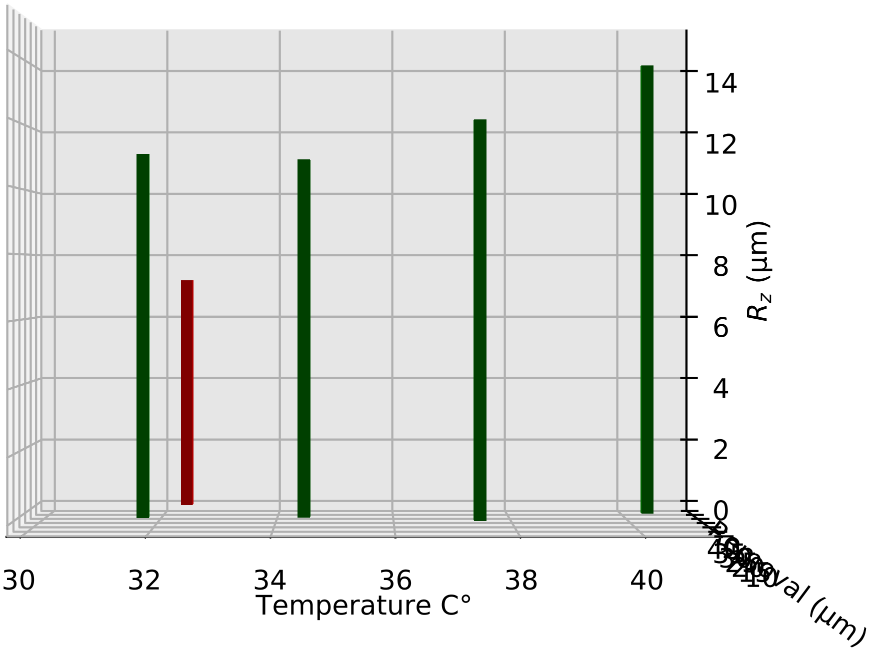

Figure 3.11: R_z Vs Removal

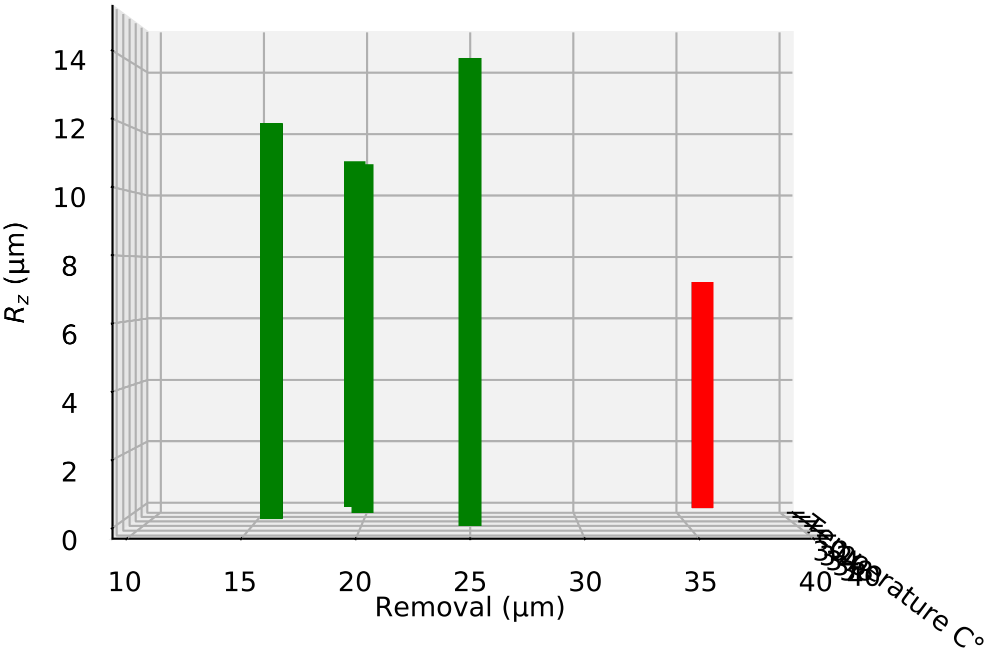

3.3 Control Parameters

3.3.1 Temperature Influence

Temperature controlling is the most complicated and dangerous procedure in the experiment:

- The thermostat water bath is not accurate and varies based on the location.
- The thermometer is hard to be fixed.
- The flotation force on the acid beaker makes it easy to fall.
- The water tank block the view makes it hard to view or control the equipment.

These factors make it more dangerous, especially when working with HF acid.

3.3.1.1 Temperature Difference Experiment

We decided to study the temperature influence first, to see if the complicated step of temperature worth the effort. The result is shown in Fig. 3.9.

If we only check the R_z Vs T, it seems like higher temperature leads to higher roughness, as shown in Fig. 3.10. However, the roughness difference is not very obvious, especially considering the 25% measure error. If the R_z Vs d (see Fig. 3.11) get checked, one may also think the roughness is growing with reaction. Since the temperature does not influence roughness too much, we decided to experiment with room temperature to make the process safer and easier to control, and potential hydrogen absorption in niobium during etching.

3.3.1.2 Cu Influence #β

The etching used the new acid resolved Cu in an accident as reported in the section 3.2.3.2 still stays in my mind for a long time. So, I did The experiment of the acid resolved copper using the previous recipe. The reaction beaker was put in a room temperature water bath to slow the sharp

Table 3.5: Systematical ratio dependence study. H_2O_2 and HF are both using 50%. Starting temperature is 20 °C, roughness before reaction is 4.31 μm ± 1.237 μm. Sample 1, 5', 6' and 7' should have higher finishing roughness because some measure values exceed the measurement range 25.2 μm and can only read 25.2 μm. *Sample 7' has too high reaction speed and too dangerous to control temperature, about 50 mL water was added when the temperature increased too high and very dangerous.

Trial	H_2O_2 (mL)	HF (mL)	Time (min)	d (μm)	T (°C)	R'_z (μm)	$\sigma_{R'_z}$ (μm)
6	51	4	60	4.5	20.14	5.02	1.162
4	48	7	60	10.0	20.91	10.63	2.688
2	45	10	60	20.5	21.60	19.53	2.707
1	42	13	60	31.0	24.29	19.09	5.019
5'	36	19	60	45.0	33.08	23.48	2.288
6'	27	28	40	251.5	53.07	22.82	3.074
7'	18	37	40	107.0	49.60*	22.94	2.596

increase of reaction temperature. The average temperature was 32.3 °C (22.1 °C increased to 44.8 °C), removal is 35.5 μm in 30 minutes reaction time.

As shown in Fig. 3.9 and Fig. 3.11, the result is very encouraging, not only the finishing roughness is 7.2 ± 1.6 μm, far less than the other cases (above 10 μm), and the reaction speed is also much higher. This was more studied later, and we finally discovered the copper catalyst effect, which will be described in the next chapter. Here, we continued the optimization test of the new acid mixture for a while.

3.3.2 Acid Ratio

One group of systematic acid-ratio variance-dependence experiments were done, the condition and result are shown in Table 3.5. All Nb samples were mechanically polished to 4.31 μm ± 1.237 μm and ultrasonic cleaned with Alconox, then rinsed with ultra-pure water. Reaction beakers were put in room-temperature water bath to slow the temperature increasing.

The Roughness Vs. HF amount and Vs. removal graph is shown in Fig. 3.12. If only check the roughness VS HF amount (Fig. 3.13), one may think the finishing surface depends on the acid ratio, that the lower the HF amount is, the smoother the finishing surface is. However, the reaction speed also highly depends on the ratio. The roughness difference for each ratio may be only due to

Figure 3.12: R_z Vs Removal and HF. The reaction condition is shown in Table 3.5.

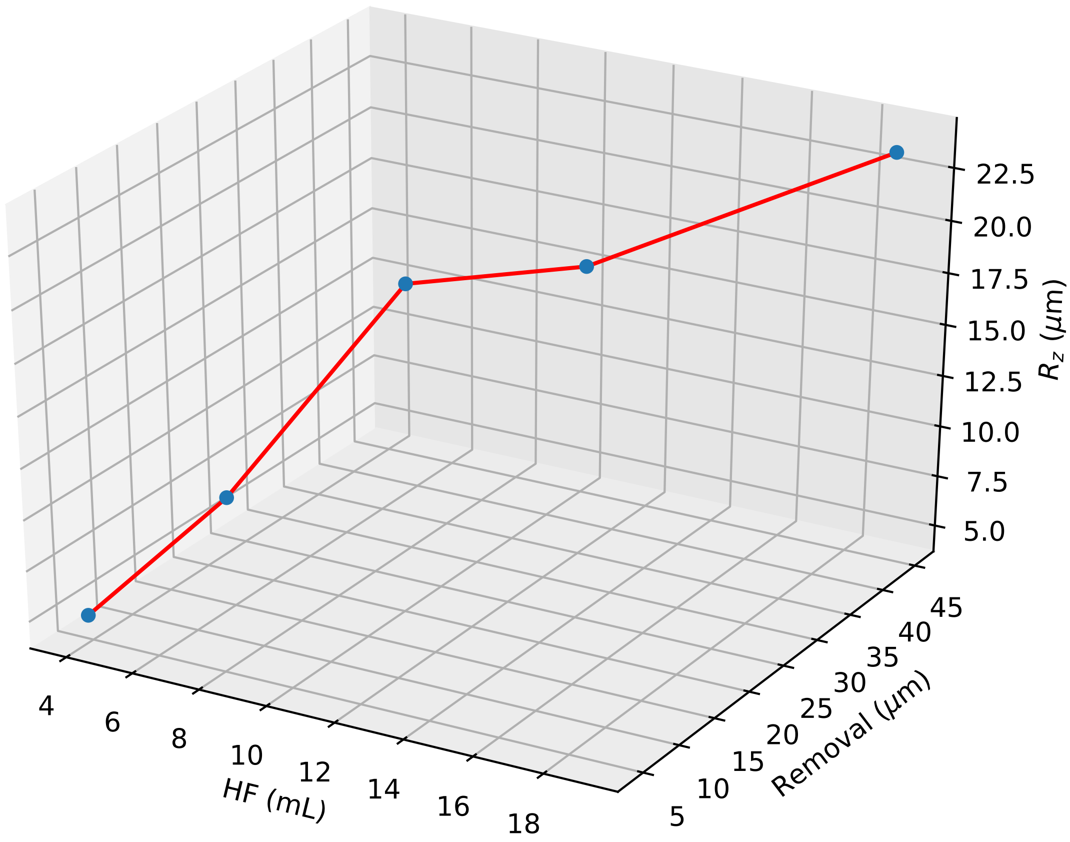

the removal difference.

It is evident that: less HF, reaction very slow, because the removal of the oxide layer is too slow; more HF reaction get much faster (this makes the experiment very dangerous), the temperature increase very fast, too.

There is no visible optimization result, all cases have very high finishing roughness, and the R_z seems proportional to the removal. Some other essential parameters need to be checked.

3.3.3 Viscosity Impact

We also tried to change the viscosity because much study shows that viscosity has an essential impact on the finishing surface.

Figure 3.13: R_z Vs HF

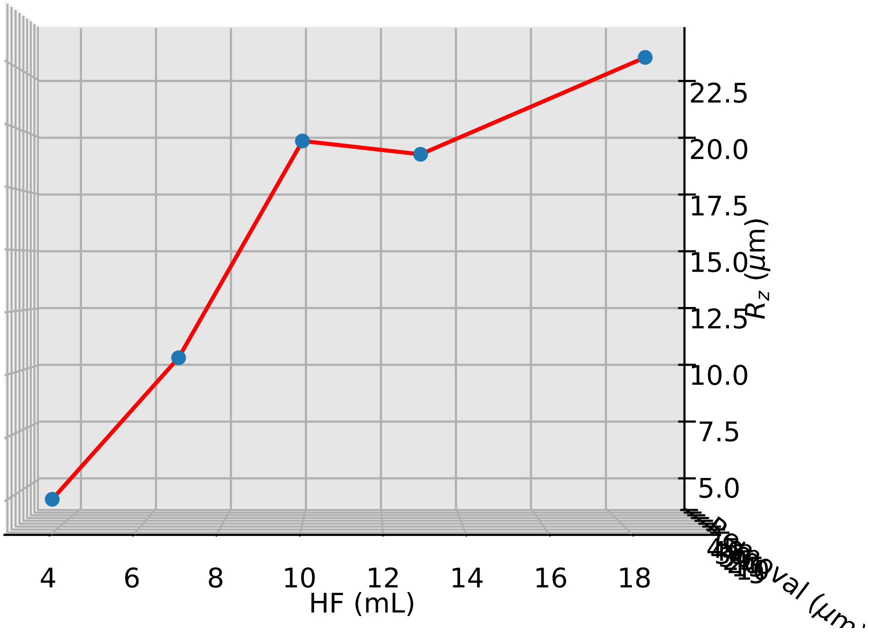

Figure 3.14: R_Z Vs Removal

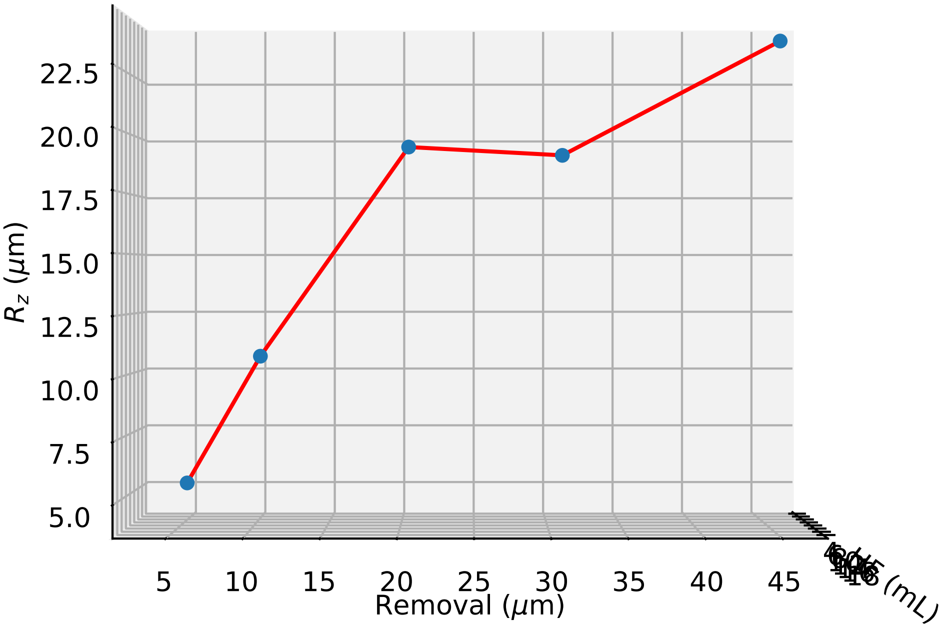

Table 3.6: Viscosity dependence for H_2O_2 and HF ratio equals to ~ 3: 1, same as Table 3.5 sample # 1. The reaction time for all cases are 120 minutes instead of 60 minutes for sample # 1 in Table 3.5. H_2O_2 and HF are both using 50%, H_3PO_4 is 90%. Starting temperature is 20 °C, roughness before reaction is 3.582 μm ± 1.683 μm.

Trial	H_2O_2 + HF (mL)	H_3PO_4 (mL)	d (μm)	T (°C)	R'_z (μm)	$\sigma_{R'_z}$ (μm)
1	55	0	31.0	24.29	19.09	5.019
A	37	18	22.0	25.47	17.09	3.963
B	28	27	10.5	23.54	10.85	4.702
C	18	37	3.0	21.70	5.17	1.930

Table 3.7: Viscosity dependence for H_2O_2 and HF ratio equals to ~ 1: 1, same as Table 3.5 sample # 6'. The reaction time for all cases are 120 minutes instead of 40 minutes for sample # 6' in Table 3.5. Starting temperature is 20 °C, roughness before reaction is 3.582 μm ± 1.683 μm.

Trial	H_2O_2 + HF (mL)	H_3PO_4 (mL)	d (μm)	T (°C)	R'_z (μm)	$\sigma_{R'_z}$ (μm)
6'	55	0	251.5	53.07	22.82	3.074
D	28	27	23.0	23.77	21.46	3.218
E	18	37	10.0	22.97	13.61	3.491

The viscosity of etching acid can influence the performance of BCP as follows. It is practical to slow the diffusion electrolyte reaction products by the chemical reaction, making the morphology: peak area has higher acid concentration, and more reaction happens, and vice versa for the valley area. Also, it prevents preferential etching. This polishing effect is enhanced when the viscosity is high [122–124].

3.3.3.1 Experiment for Viscosity Influence

In order to study the viscosity effect, we then tried $HF+H_2O_2+H_3PO_4$ mixture because phosphoric acid has a high viscosity and is commonly used in BCP.

Two groups of experiments were done. One based on section 3.3.2, trial # 1 (42 mL H_2O_2: 13 mL HF), increase H_3PO_4 over acid ratio from 0 to 1: 2, 1: 1 and 2: 1. Another one is based on section 3.3.2, trial # 6' (51 mL H_2O_2: 4 mL HF), increase H_3PO_4 over acid ratio from 0 to 1: 1 and 2: 1.

No improvement was observed for both groups of experiments. As seen in Fig. 3.15, the increased viscosity slower the reaction speed; however, the results for both groups showed that

Figure 3.15: R_z Vs H_3PO_4/Acid Ratio and Removal

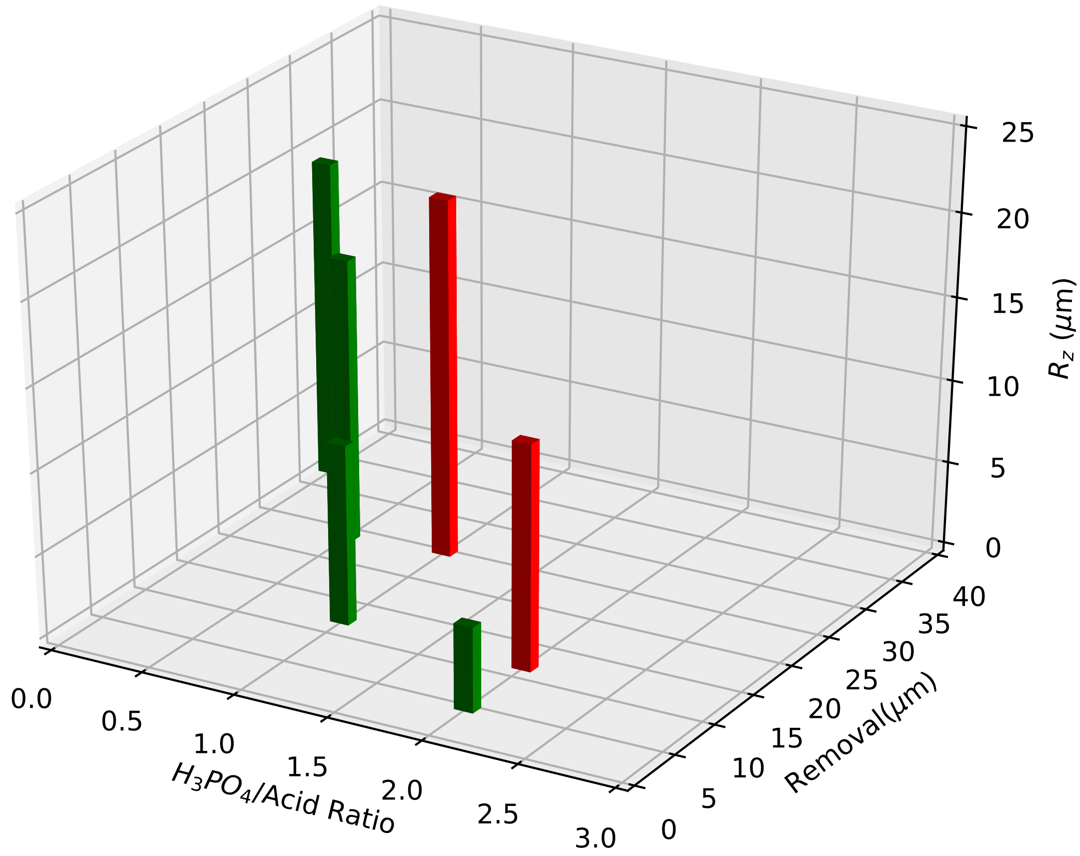

only material removal speed was reduced, some case such has minimal reaction while the surface remained very rough.

3.3.3.2 Using H_2SO_4 to Increase Viscosity

$HF+H_2O_2+H_2SO_4$ mixture was also used in another trial. This group of experiments were done in Nomura Plating. Ltd because the mixture is possibly explosive. The reason for the material speed reduction in the above H_3PO_4 mixture is probably due to the poor oxidation capability. Sulfuric acid will add oxidation power as well as high viscosity to the new acid.

The results showed surface roughness $R_z = 10.4 \pm 6.2$ μm after ~ 8.4 μm etched. The mixture

Figure 3.16: Microscope images for fine-grain sample reacted with new acid (A) and with new acid plus H_2SO_4 (B).

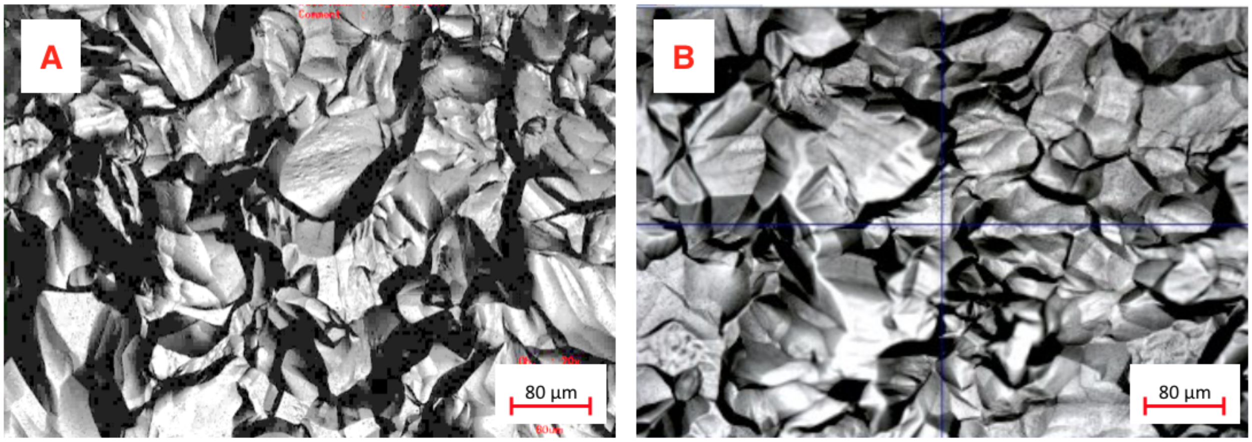

Table 3.8: Comparison of copper cases with or without H_3PO_4. #β is the Cu case in section 3.3.1, Table 3.9. H_2O_2 is in 35% and HF is using 50%, and the ratio is 45: 10, Cu amount is ~ 3.10^{-4} mol and Starting temperature is 20 °C for both cases. The roughness before reaction for β is 9.067 μm ± 2.953 μm and for γ is 4.000μm ± 2.783 μm.

Trial	H_2O_2 + HF (mL)	H_3PO_4 (mL)	d (μm)	T (°C)	R'_z (μm)	$\sigma_{R'_z}$ (μm)
β	55	0	35.5	32.3	7.19	1.640
γ	28	27	16.5	19.92	9.01	3.511

consisted of 10 mL 50% HF, 45 mL 35% H_2O_2, and 60 mL 98% H_2SO_4. We also tried other composition ratios, but the results had no significant differences. Fig. 3.16 shows the SEM image of the adding H_2SO_4 cases (B) and original new acid (A) results. There is no obvious difference between these two cases.

3.3.3.3 Copper Case with Higher Viscosity #γ

Copper case with H_3PO_4 was also studied. We use the acid ratio same as the previous sample #β in section 3.3.1 case 28 mL, and add 27 mL of H_3PO_4, then add copper. One Nb sample was put into the acid mixture after copper finished reaction. The increased viscosity does not help the Nb get a better surface and even worsen it. We think maybe the high viscosity blocked the bubbles from getting away.

Overall we found none of these trials can reduce the roughness. Same as in section 3.3.1 and in section 3.3.2, there is also a trend for the R_z Vs Removal in this case. We think some fundamental parameters should exist, but we have not found. Without meeting those criteria, all trials can only have small scale impact, but the roughness will still stay at quite a high level.

3.4 High Roughness Study

We got high roughness for all cases (except for the copper cases) of our new acid experiments. Before getting the mechanism of it, we can study the location of the high roughness first. There are two possibilities:

- High roughness due to grain-boundaries.
- High roughness in the grain gets erosion from the new acid.

Considering that we are using fine-grain (~ μm) Nb samples for all experiments, one straightforward guess is that the grain-boundary preferential etching leads to the high roughness just like the BCP cases.

Different reaction speed for grain crystalline direction is another possibility relate to grain-boundaries. This is because different orientation has different atom density, which may cause different reactions speed.

Large-grain (1 - 2 cm scale) niobium samples has much fewer grain-boundaries than fine-grain (~ 50 μm scale) ones and these boundaries are visible after the reaction. Experiments with these large-grain (~ cm size) Nb samples were done to study the possible grain-boundary influence. If the large-grain Nb sample gets lower roughness than before, we can confirm grain-boundary – either preferential etching or orientation reaction speed difference – lead to the high roughness. Otherwise the high value most from in grain roughness.

3.4.1 Orientation of Large-grain Nb Crystalline

One large-grain Nb sample composed of three large crystallines with sizes ~ 1.5 cm × 0.5 cm were studied after new acid reaction (10 μm removal). A joint point image was captured by Orientation

Figure 3.17: Orientation Imaging Microscopy (OIM) image of a joint point of three grains on a large-grain Nb sample after ~ 10 μm removal by new acid. Different color indicate different crystalline orientation.

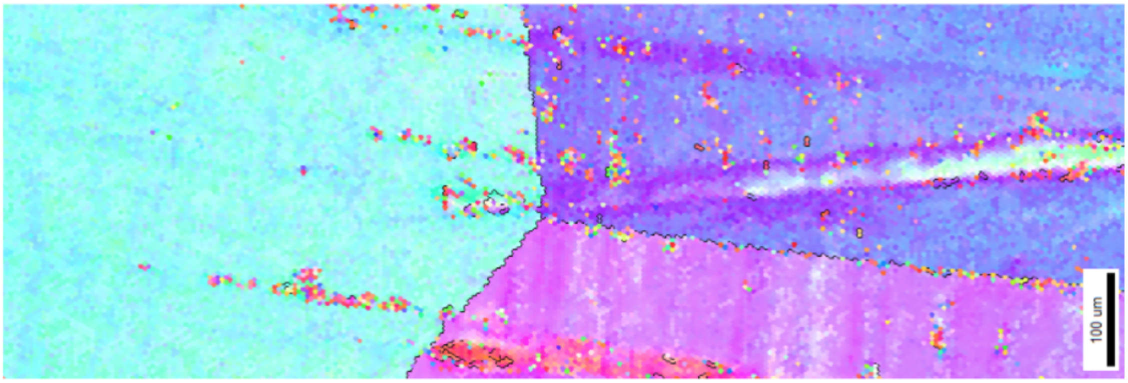

Imaging Microscopy (OIM) to get the orientation information, as shown in Fig. 3.17.

According to the OIM result, it is obvious that different grain has a different orientation. However, some noise points exist on the image due to high roughness which means this method results can be influenced by roughness. If we apply OIM on the fine-grain sample, the resulting image will have more roughness noise than the large-grain one that we cannot distinguish the orientation from the roughness. One fine-grain Nb sample which was also removed ~ 10 μm by new acid was observed, while no signal of OIM image can get.

3.4.2 Roughness between Grain-boundaries and Internal Grain

Among the large-grain samples, one sample shows different reaction speed on different grains. For example, Fig. 3.18 shows step structure on grain-boundaries while no visible grain-boundary preferential etching observed on this figure. The roughness crosses the grain-boundary is ~ 7 μm, while the internal grain is ~ 2 μm. This indicates the reaction speed difference on different grains in the fine-grain Nb sample (grain size ~ 50 μm) can cause the high roughness, because the measurement route of the roughness tester is several millimeters long, and would cross ~ 100 grains.

However, we noticed the internal grain roughness ~ 2 μm is still high compare with conventional BCP large-grain roughness, which is only ~ 250 nm. Fig. 3.19 and Fig. 3.20 shows SEM images

Figure 3.18: Reaction difference is observed in one large-grain sample. This sample was reacted with new acid and the removal is ~ 20 μm.

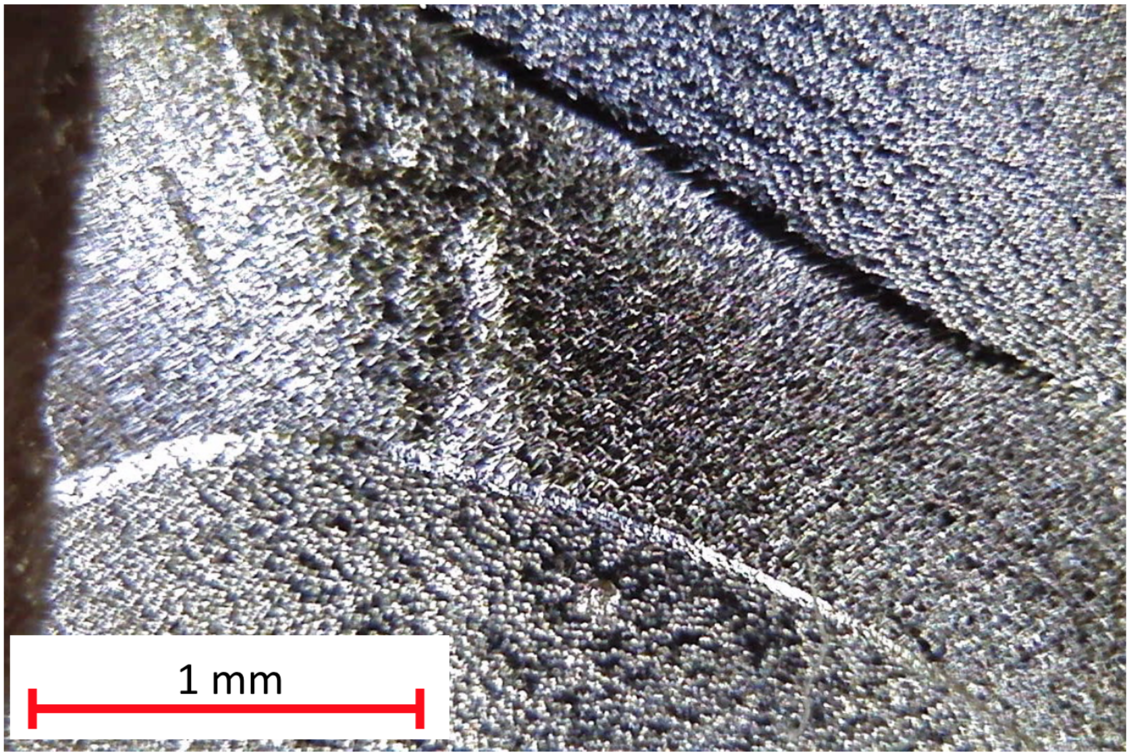

Figure 3.19: SEM images and roughness map for large-grain sample reacted with new acid.

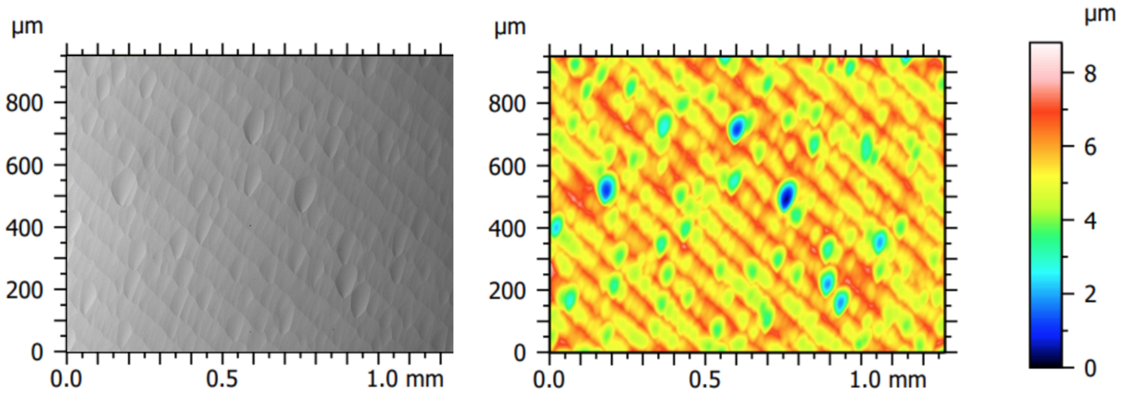

and roughness map of large-grain Nb sample treated with new acid and with conventional BCP.

We conclude that both grain difference and in-grain erosion caused the high roughness of new acid with Nb sample.

Figure 3.20: SEM images and roughness map for large-grain sample reacted with conventional BCP.

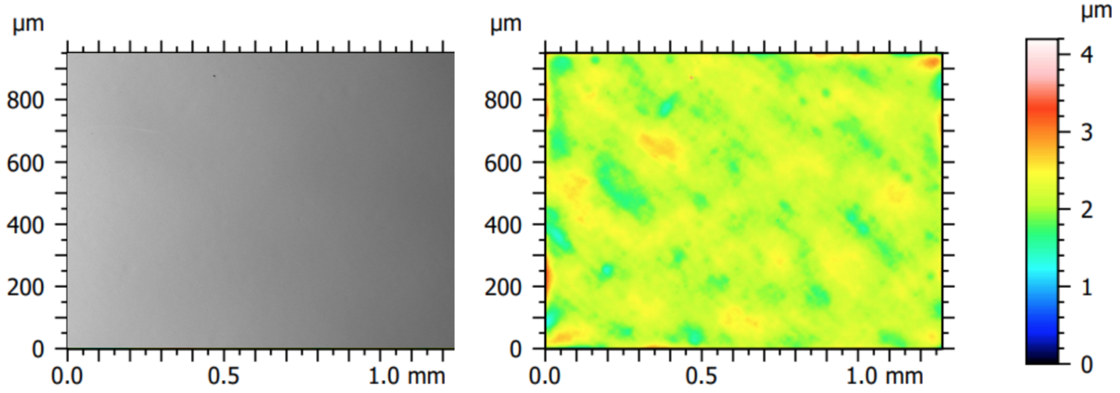

3.4.3 Discussion

For the new acid, we got the confirmation that the grain-boundary influence is as severe as BCP cases because of the reaction speed difference on density difference from different crystalline orientation. Additionally, some erosion effects always exist on the internal grain surface reaction, and we have no information on why this happens.

As seen above, we made many efforts for the new acid optimization: acid agitation, acid mixture ratio, pre-preparation choice, temperature control, viscosity, and other trials. Unfortunately, we could not find the critical condition in any of these parameters to get the smooth finished surface $\sim 3\ \mu$m.

Our conclusion for the rough finishing surface with the new acid is due to mainly the preferential etching performance of this new acid, which will be the behind the reason why Saclay gave up this mixture. We remain a question why Nomura plating succeeded to the smooth finishing surface using this mixture; even they need to improve the finishing microstructure as seen in Fig. 3.2 and Fig. 3.3. However, if the preferential etching is the leading cause of the rough finishing surface, we have to give up this new acid, as Saclay did it. However, we still have hope for the new acid resolved copper, as shown in section 3.3.1.2. So I decided to continue more study for this acid.

CHAPTER 4

COPPER CATALYST

We described several experiments related to a copper contamination accident that happened during the new acid experiment process in section 3.2.3.2, section 3.3.1.2, and section 3.3.3.3. We found this copper additive somewhat helped to solve the high roughness problems, so we decided to optimize this copper case and meanwhile try to find the mechanism of the high roughness reason for our new recipe. Two example pictures are shown in Fig. 4.1.

4.1 Setup optimization

4.1.1 A Quick Check of Copper amount and H_2O_2 Concentration Influence

We are curious about the H_2O_2 concentration and the copper amount influence, and we did one group of experiment.

For the copper used in the experiment; initially, the accident was caused by a copper nut drop

Figure 4.1: A comparison between new acid sample without and with Cu catalyst.

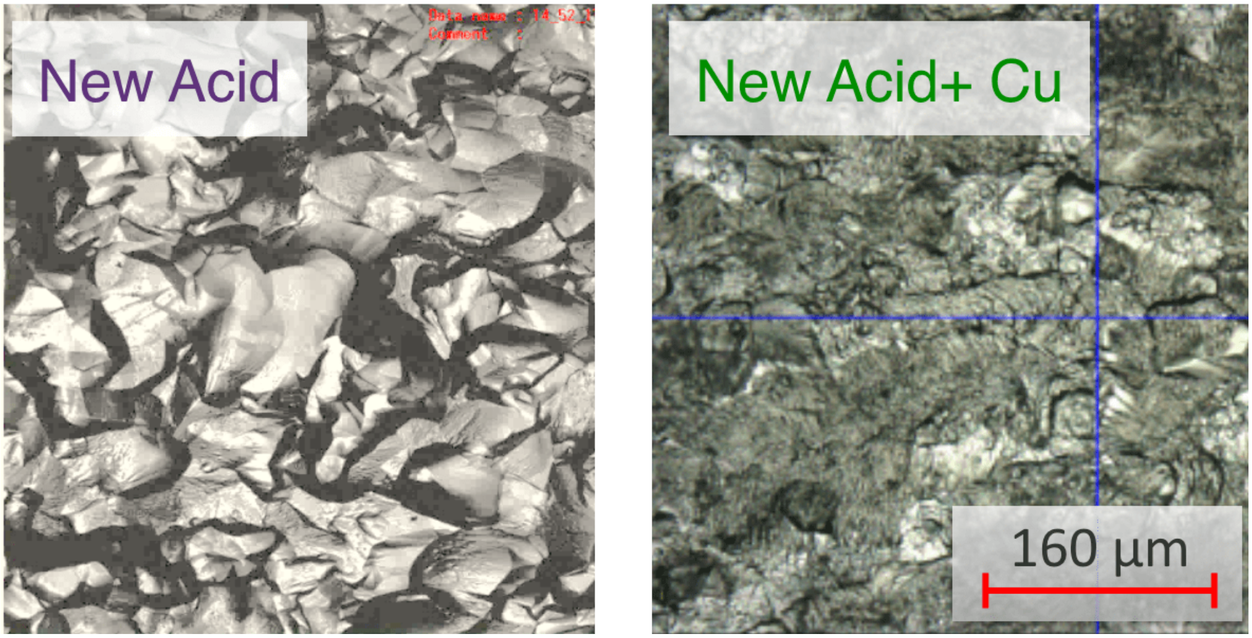

Table 4.1: H_2O_2 concentration and Cu amount variation results, HF concentration is 50 % for all cases.

Trial	H_2O_2 %	Cu (mol)	d (μm)	T (°C)	R'_z (μm)	$\sigma_{R'_z}$ (μm)
H	35	3.10×10^{-4}	41	26	5.95	1.52
I	35	6.20×10^{-4}	40	28	6.68	1.52
J	50	2.09×10^{-4}	53	28	5.49	1.16

into the acid, there was no reaction amount of cooper information. For the second and third experiment, we used a sealing copper gasket (Commercial product with the purity of > 99.0 % copper) which was discarded from cavity assembly. We cut it in half. The half ring is pure enough and easy to handle. The Cu mole amount is calculated from its mole mass 63.546 g/mol, where the Cu mass is measured before and after the half gasket reaction.

A controlling of the Cu amount is based on the reaction time, 30 seconds and 60 seconds are the two options which we used in this group of experiments. Acid mixture for a sample # H and J both has the 30 seconds reaction on the same Cu, the Cu amount resolved in the acid for two reactions are 0.3945 g; and I has a 60 seconds reaction, for which the amount of Cu dissolved in acid is 0.2657g, correspondence to 2.09×10^{-4} mole, which is lower than the Cu amount resolved in acid for sample H, this may be due to the H_2O_2 higher concentration.

For all three cases, Nb sample roughness was 3.51 ± 1.45 μm before reaction; the reaction time was 40 minutes, the starting temperature was 20 °C. For the volume of acid mixture, 50 %HF amount is 10 mL, H_2O_2 amounts is 45 mL and the concentrations are list in Table 4.1.

For trial # J, we used 50% H_2O_2 and compare with # H which used 35% H_2O_2, the Cu amount is slightly different even both cases has 30-second copper reaction before Nb was put in, this should be due to acid concentration difference. The result of # J is not too different, while the Nb reaction was too fast and dangerous, so for the following cases, we continue our experiment with 35% H_2O_2.

For trial # H and I, it seems like # H has slightly smoother result. To study the copper effect more, we purchased Copper powder for more accurate controlling of the copper amount and continued the experiment.

Table 4.2: Cu powder amount variation results

Trial	Cu (mol)	d (μm)	T (°C)	R_z (μm)	σ_{R_z} (μm)	R'_z (μm)	$\sigma_{R'_z}$ (μm)
R	1.24×10^{-4}	40.0	25.9	4.68	0.915	6.74	1.62
S	3.02×10^{-4}	46.0	27.3	5.41	1.722	6.05	1.64
T	6.45×10^{-4}	57.0	27.3	7.74	2.817	8.32	1.99
U	1.15×10^{-3}	56.5	26.3	6.76	3.606	8.22	1.34

4.1.2 Copper Amount Variation for 45: 10 Recipe Using Cu Powder

In the following experiments, we want to control the copper amount in the mixture to see the influence, so we need more accurate value. We used copper powder (99.9 % pure) in this group of experiments. The copper powder is tough to transfer, so we use small centrifuge tube as a container when measuring the copper powder, and put the whole opened tube into the acid and wait until the reaction between copper and acid finished, and take the tube out before putting Nb in.

We also try to get similar Nb removal, so we watch the color of the acid instead of setting a specific reaction time because the similar shade of green color indicates similar Nb dissolved in acid. Case R and S have 50 minutes, T had 60 minutes, and U had 70 minutes reaction time.

The acid recipe follows # H and I, 45 mL 35% H_2O_2 plus 10 mL 50% HF and starting temperature also 20 °C. The Nb roughness before reaction for each case is very different because of bad controlling of mechanical polishing; the data is listed in Table 4.2.

We got the best result from sample S (3×10^{-4} mole Copper), slightly better than all other cases. However, even though the measured value more accurate, the copper powder is tough to handle. The powder is very easy to spit out even we put the whole centrifuge tube in acid. (Trial # S split a bit copper) The copper powder is also easy to adhere to the beaker's wall or gloves due to electrostatic attraction. This again makes the amount of copper very uncertain.

4.1.3 HF Amount Variation for 3×10^{-4} mole Copper Powder

In this case, we want to keep the H_2O_2 concentration, and copper amount stay the same and only study the HF concentration influence. We improved the experiment method by using 29 mL 50%

Table 4.3: HF amount variation results for 3 × 10^{-4} mole Copper Powder. 6' has same condition with 2', but with stirring.

Trial	HF (mL)	H_2O (mL)	d (μm)	R_z (μm)	σ_{R_z} (μm)	R'_z (μm)	$\sigma_{R'_z}$ (μm)
2'	10	16	66.5	4.18	1.27	7.32	1.35
3'	15	11	83.5	4.86	2.38	6.27	1.55
4'	20	6	76.0	4.64	1.30	6.59	1.62
5'	25	1	90.5	4.61	2.02	10.10	2.86
6'	10	16	78.0	5.05	1.63	8.14	1.62

Table 4.4: Additional reaction for case 3', 4' and 5'. The same Nb samples are without extra mechanical polishing, so the roughness before reaction are from R'_z in Table 4.3. The Nb were put into the original acid saved from last reaction.

Trial	HF (mL)	H_2O (mL)	d (μm)	R'_z (μm)	$\sigma_{R'_z}$ (μm)	R''_z (μm)	$\sigma_{R''_z}$ (μm)
3"	15	11	11.5	6.27	1.55	6.04	1.30
4"	20	6	34.0	6.59	1.62	9.36	2.24
5"	25	1	30.5	10.10	2.86	13.03	3.20

H_2O_2 for all cases, add different amount of HF, and adjust the concentration of H_2O_2 by adding water to reach a total volume of acid 55 mL. The Copper amount for each case is $2.72 \pm 0.45 \times 10^{-4}$ mol. The starting temperature is 18 °C and the ending temperature is about 32°C for all cases. 50% HF amount and water amount are shown in Table 4.3. 2' and 6' has 70 minutes of reaction time, and other cases have about 10 minutes reaction time because higher HF amount leads to very high reaction speed.

Additional reactions for three cases are done for case 3', 4' and 5', shown in Table 4.4, to compensate the possible different reaction amount of Nb.

In the two groups of experiments, trail 3' and 3" show an optimum roughness compare with other cases listed in Table 4.3 and Table 4.4, so we decided to choose this recipe to continue the optimization.

This time we tried to directly put the copper powder in the beaker before any reaction to avoid copper spit during opening the small tube used in section 4.1.2. However, we are still not sure about the amount of copper since some may still spit out or adhere to the beaker wall and does not react with acid.

Table 4.5: Copper variation for H_2O_2 (50%): HF (50%): H_2O = 29: 15: 11 Recipe using thin copper wire.

Trial	Cu mg/L	d (μm)	R_z (μm)	σ_{R_z} (μm)	R'_z (μm)	$\sigma_{R'_z}$ (μm)
a	230	33.5	2.83	0.99	3.67	0.71
b	282	36.0	2.24	0.81	3.36	0.76
c	329	34.5	2.61	0.91	3.23	0.90
d	381	35.5	2.23	0.73	4.06	0.78
e	425	29.0	1.93	0.67	2.90	0.48
h	403	62.0	1.81	1.23	4.07	0.79
i	403	71.5	1.42	0.46	3.82	0.89
j	464	64.5	1.45	0.44	3.97	0.84
k	522	51.0	1.85	0.70	4.66	0.94
l	573	51.5	1.70	0.55	4.90	1.12

4.1.4 Copper Amount Variation for 29: 15: 11 Recipe Using Thin Cu Wire

We then switched to a very thin copper wire (99.999 % pure) and the diameter is ~ 0.127 mm, the length density is ~ 0.11 g/m. We first cut a wanted estimated length of the copper, then measure the mass for a more accurate value. This is our optimized way of controlling the copper amount because it is accurate and easy to handle. The roughness before the reaction was also improved to a lower and stable value. We are using recipe of sample 3' for this round of experiment, which is 29 mL 50% H_2O_2, 15 mL 50% HF and 11 mL H_2O.

The amount of copper for each cases are shown in Table 4.5. For example, case #j has 464 mg/L Cu, correspondence to 4×10^{-4} mol Cu in 55 mL mix acid, which is 7.27×10^{-3} mol/L.

We tested the copper concentration from 230 mg/L to 573 mg/L, of which results are summarized in Table 4.5.

Case # e has 2.90 ± 0.48 μm roughness with 425 mg/L copper (best result), while other cases, such as case # c has 3.23 ± 0.90 μm, is not much worse than this best result, especially when we consider the roughness before reaction, see Fig. 4.3. The finishing roughness still has a worsening trend, but it is much mitigated by using copper resolved acid. The role of the copper is considered a catalyst effect, which will discuss later. Till now, we think Cu amount 329 to 425 mg/L has the best effect to help our new acid to smooth the Nb finishing surface, while it does not need to be very accurate.

Figure 4.2: R_z Vs Cu amount and Removal. Green squares are roughness after reaction, and red squares are roughness before reaction. 1 ppm equals to 1 mg/L (defined in analytical chemistry).

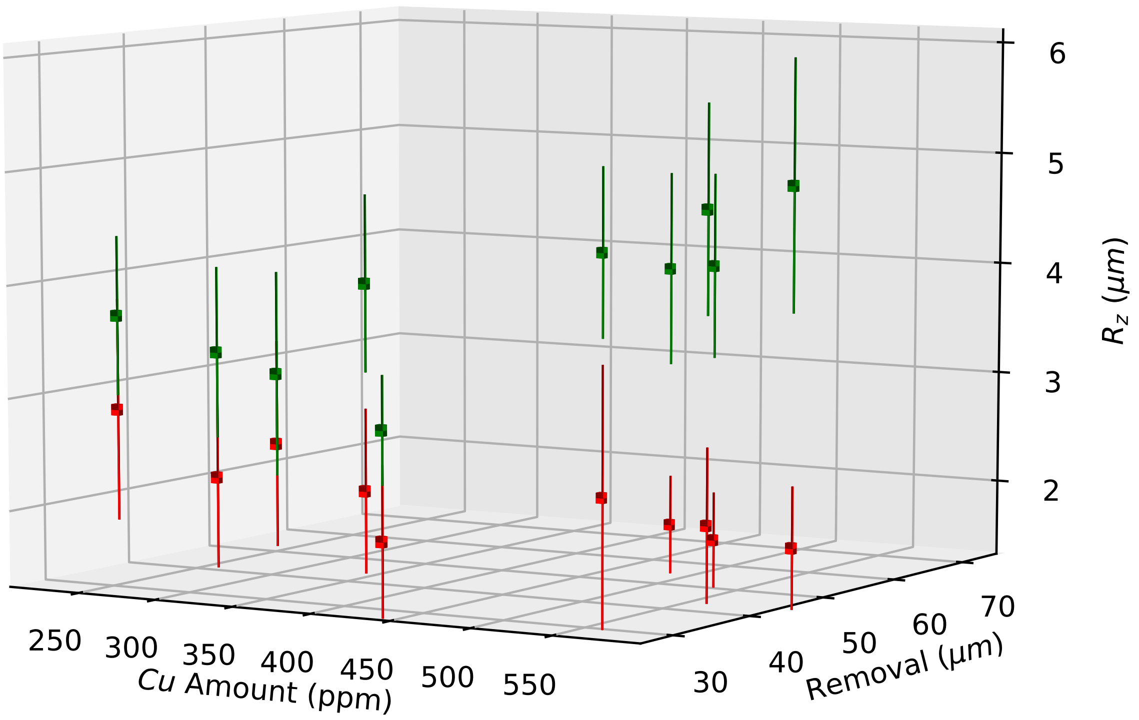

4.2 Summary of Experiments

A summary of our experiment is shown in Fig. 4.4. The grey ones are all reactions without Cu catalyst; the red triangles are BCP results with Acid ratio 1: 1: 2 (Volume ratio HNO_3: HF: H_3PO_4); the blue dots are HF variation test and the green crosses are Cu amount variation.

The finishing roughness trend with no copper catalyst cases is much higher than those with catalyst cases. The copper catalyst cases after optimization are similar to the BCP cases. (red solid triangle mark in Fig. 4.4). One can see in Fig. 4.4 that the best-optimized mixture recipe with the copper catalyst can suppress the grain-boundary preferential etching on the new mixture (no copper), reached R_z = 3 μm after 75 μm material removal, which satisfies our goal.

For the morphology, a large scale photo is shown two samples together reacted with new acid with catalyst and reacted with BCP in Fig. 4.5. The roughness on millimetre-scale is similar for both cases, while the BCP sample has some typical "orange skin" structure.

Figure 4.3: R_z Vs Cu amount. Green squares are roughness after reaction, and red squares are roughness before reaction. 1 ppm equals to 1 mg/L (defined in analytical chemistry).

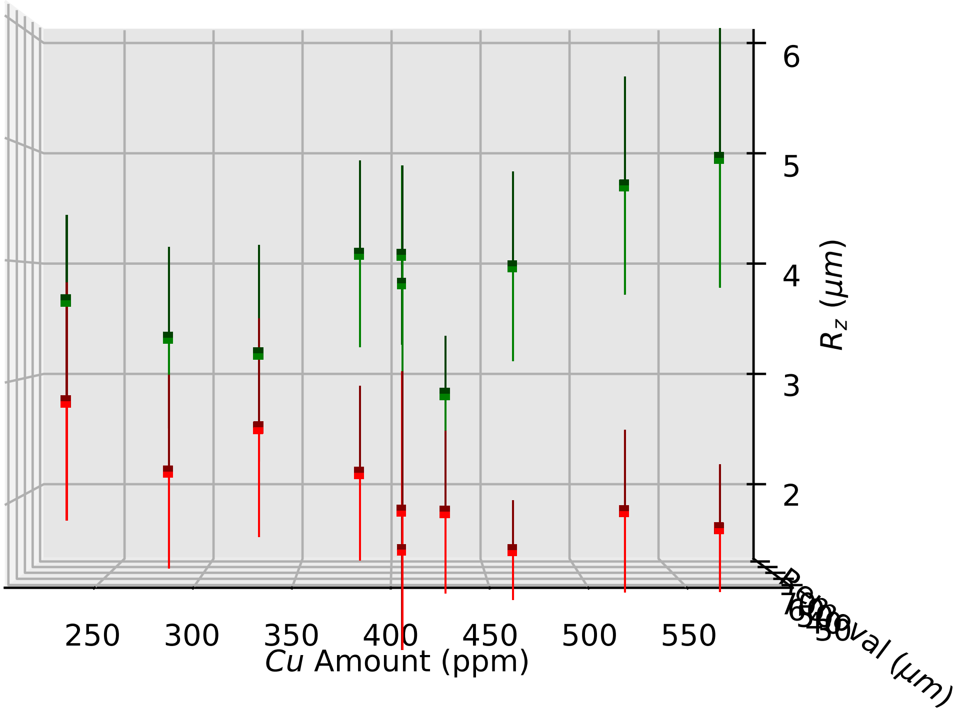

Figure 4.4: A summary of the whole optimization process with conventional BCP result. Grey marks are new acid without catalyst, red triangles are BCP (1: 1: 2) cases, blue dots are HF variation results, green crosses are Cu variation results that using the previous best 15 mL recipe from the HF variation results. The Cu variation influence is already shown in Fig. 4.2 and 4.3.

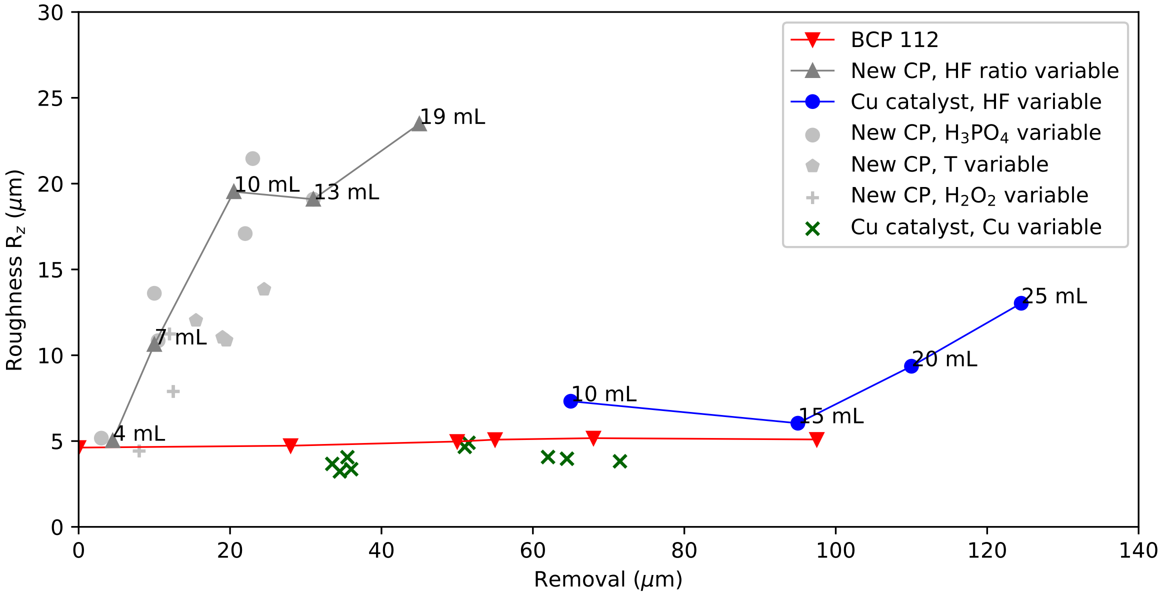

Figure 4.5: A comparison between new acid with Cu catalyst sample and BCP sample.

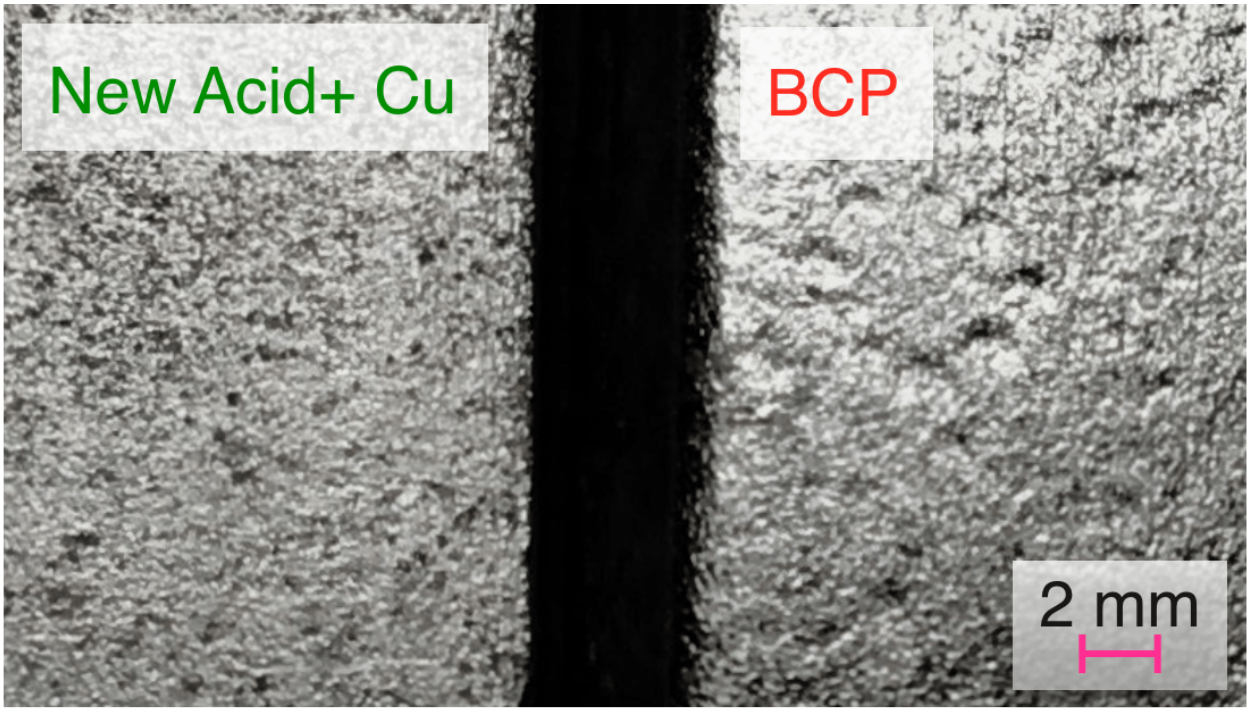

Three magnification of SEM images are shown in Fig. 4.6, Fig. 4.7 and Fig. 4.8. It is more clear that for 500 μm scale (Fig. 4.6), the new acid sample is more smooth, while in the 20 μm scale (Fig. 4.8), the BCP sample has less structures.

4.3 Mechanism

4.3.1 Chemical Reactions

This section explains the chemical reactions that occur when Cu is added into the polishing acid mixture and discusses their implications.

A series of reactions happen during the experiment:

$$\mathrm{Cu} + \mathrm{H_2O_2} \longrightarrow \mathrm{CuO} + \mathrm{H_2O}, \tag{4.1}$$

$$\mathrm{CuO} + \mathrm{H_2O_2} \longrightarrow \mathrm{CuO_2} + \mathrm{H_2O}, \tag{4.2}$$

$$2\,\mathrm{CuO_2} \longrightarrow 2\,\mathrm{CuO} + \mathrm{O_2}\uparrow. \tag{4.3}$$

Figure 4.6: SEM Image of Nb samples after new acid polishing (a) and after BCP (b), 75 times magnification.

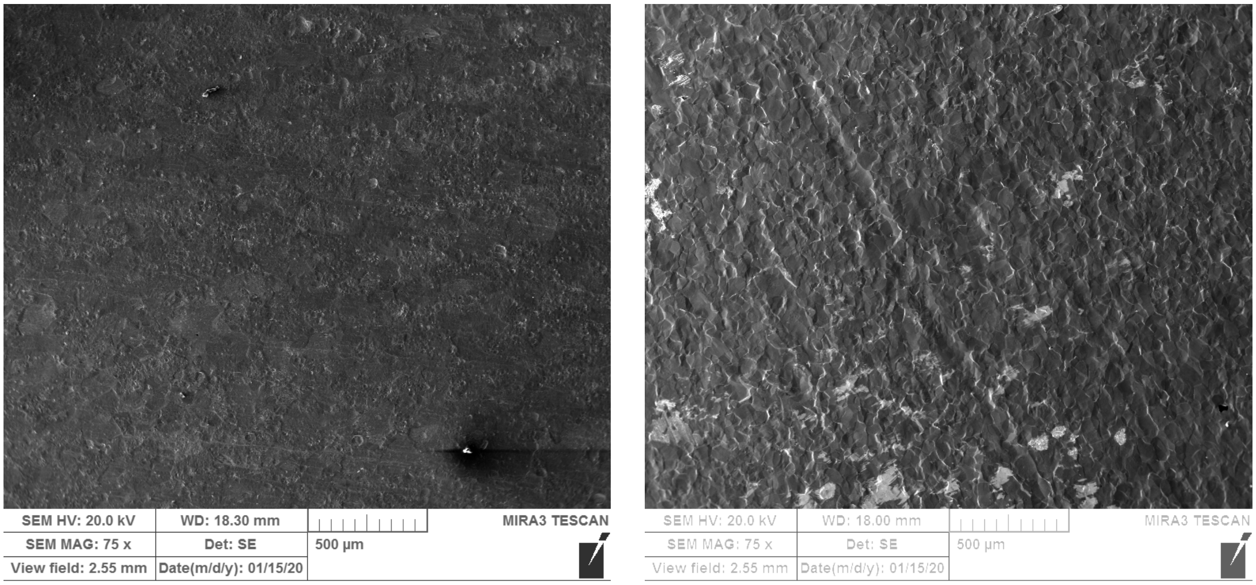
(a)

(b)

Figure 4.7: SEM Image of Nb samples after new acid polishing (a) and after BCP (b), 350 times magnification.

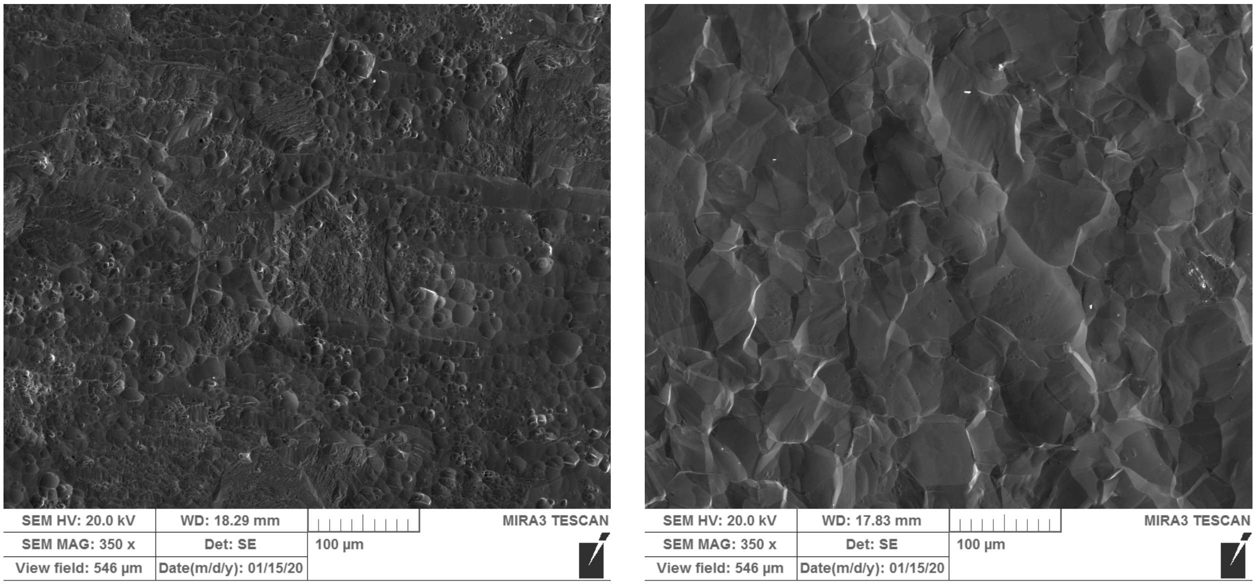
(a)

(b)

Figure 4.8: SEM Image of Nb samples after new acid polishing (a) and after BCP (b), 350 times magnification.

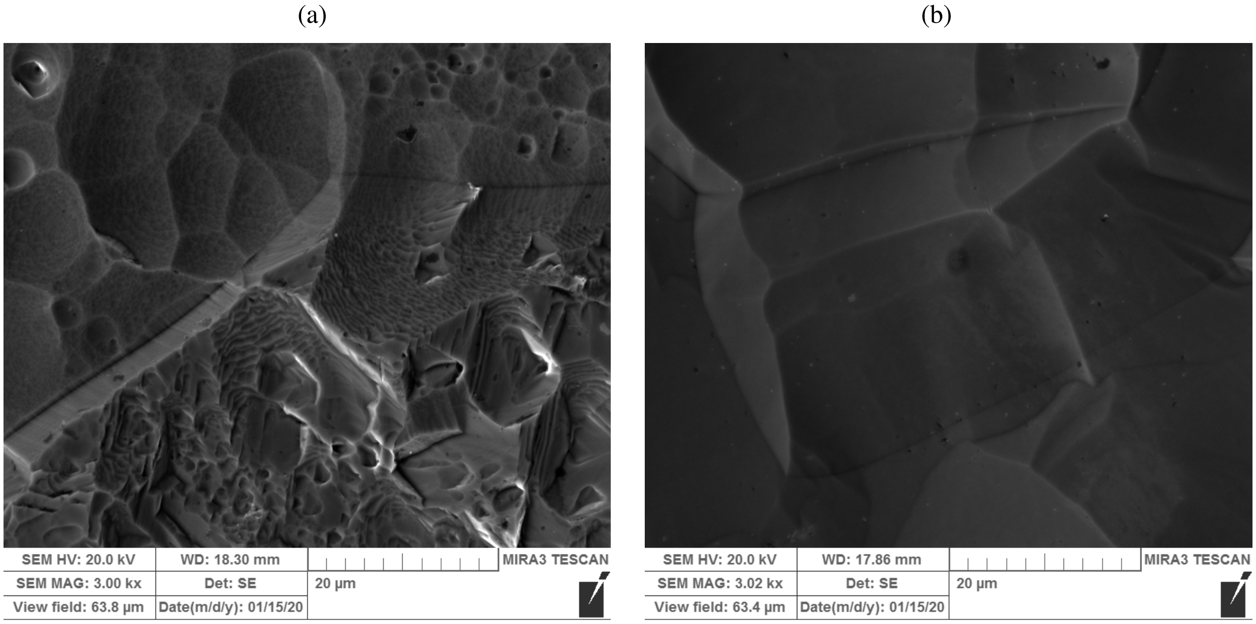

Figure 4.9: SEM Image of another Nb sample after new acid polishing (a) 75 times (b) 350 times and (c) 3000 times magnification.

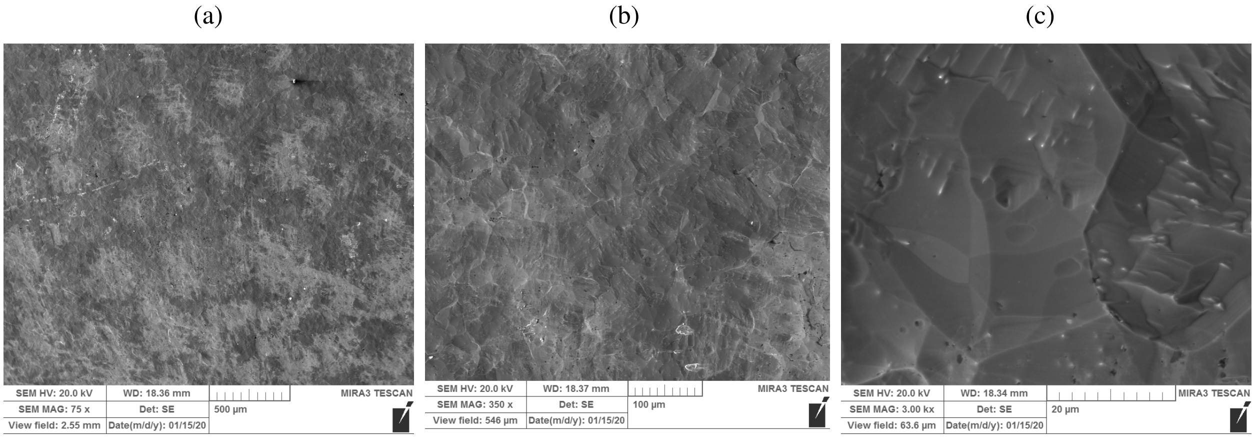

These reactions constitute a H_2O_2 decomposing process with Cu as the catalyst, and can be written as:

$$2\,H_2O_2 \xrightarrow{\text{Cu}} 2\,H_2O + O_2\uparrow. \tag{4.4}$$

Then the CuO reacts with HF:

$$CuO + 2\,HF \longrightarrow CuF_2 + H_2O, \tag{4.5}$$

or

$$CuO + 4\,HF \longrightarrow Cu(HF_2)_2 + H_2O. \tag{4.6}$$

The Cu^{2+} dissolves in the acid, and when Nb is put into the acid, reaction

$$5\,Cu^{2+} + 2\,Nb \longrightarrow 5\,Cu + 2\,Nb^{5+}, \tag{4.7}$$

happens due to single-displacement reaction, and Nb^{5+} dissolves into the acid to generate a Cu layer outside the Nb, and reaction Eqs. 4.1 to Eqs. 4.7 continuously happen, until any of the component is consumed. During this process, Cu accelerates the reaction and is not consumed, thus acting as a catalyst.

The combination of the whole process can be written as:

$$20\,H_2O_2 + 20\,HF + 4\,Nb \xrightarrow{\text{Cu}} 4\,NbF_5 + 5\,O_2\uparrow + 30\,H_2O. \tag{4.8}$$

The critical components of the whole reaction series are reaction Eqs. 4.4 and reaction Eqs. 4.7: there will be no gas product without reaction Eqs. 4.4, which is essential to finishing surface roughness (will be explained later); if there is no reaction Eqs. 4.7, the metal ions will be excluded from the reaction series and stay in the acid. Therefore, any metals that meet these two processes should be able to work as a catalyst for this acid. Reaction Eqs. 4.7 needs the metal to be less reactive (in the reactivity series) than Nb, and reaction Eqs. 4.2 needs the metal to be at least oxidizable by H_2O_2 (can be found from Standard electrode potential), so the series of potential catalysts are: (Nb), Zn, Cr, Ga, Fe, Cd, In, Tl, Co, Ni, Mo, Sn, Pb, W, Ge, Cu, Tc, Ru, Po, Hg, Ag.

Figure 4.10: Acid component is 45 mL 35% H_2O_2, 10 mL HF with (a) Fe amount 2×10^{-4} mole, 35 μm removal, $R_z = 13.52 \pm 5$ μm and (b) Fe amount 1×10^{-4} mole, 38 μm removal, $R_z = 16.08 \pm 3$ μm.

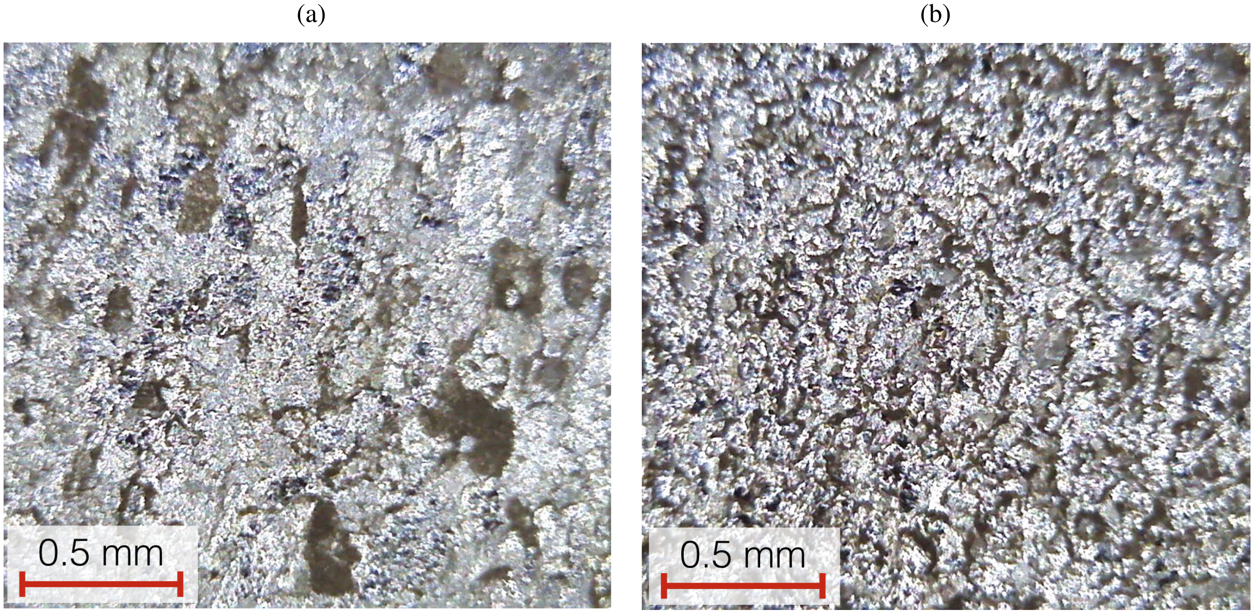

In this series, the more reactive (closer to Nb) the metal is, the slower reaction Eqs. 4.7 will be, which is closer to the scenario without a catalyst. Conversely, the less reactive (closer to Ag) the metal is, the stronger the metal ion's oxidization power, so it is more catalyst effective.

We also tried Fe, which is closer to Nb than Cu, and the reaction happened as we predicted and the finishing surface roughness was $R_Z = 10 \sim 16$ μm depending on the amount of Fe. The result agrees with our analysis of catalyst effectiveness. As shown in Fig. 4.10, the roughness is very sensitive with the Fe amount, when the amount is 2×10^{-4} mole, some bubble-sign like large scale holes exist, we think this is over amount; however, when the Fe amount is 1×10^{-4} mole, the roughness and morphology is very similar to no catalyst case, we think this is under amount.

4.3.2 General Chemical Polishing Principle and the Bubble Effect

The underlying principle of general chemical polishing is a higher reaction rate at the peaks than at the valleys. This produces a soothing effect on the surface; some fundamental studies can be found in Ref. [122]. Several parameters are essential for the finishing surface, such as viscosity [123,

Figure 4.11: Bubble generating (a) and growing (b) on metal peak and valley during chemical polishing.

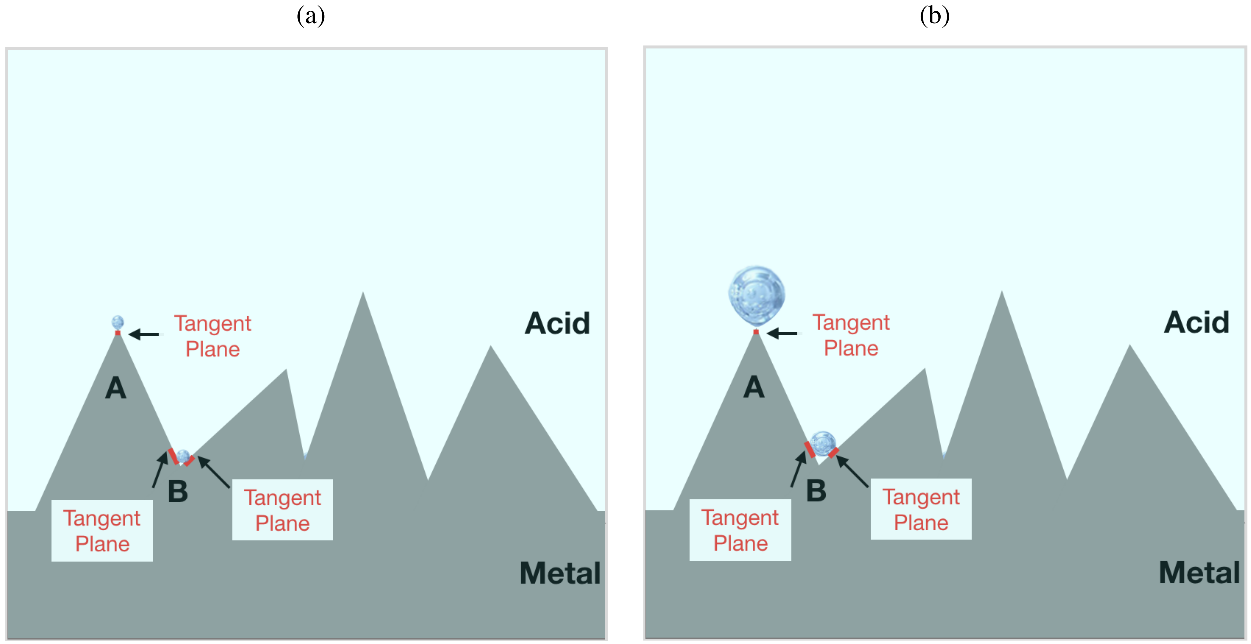

124], oxidation layer formation [125], temperature.

For a chemical polishing process, the reaction rate difference arises because the peak has higher acid amount to react with than the valley for a similar reaction area [122, 126]. This difference can be enhanced by bubbles generated on the metal surface which block the reaction more around the valley area than at the peak [127] because bubble grow slower and stay longer on the valley area.

Bubbles that grow during the reaction will start departing the surface once they reach a critical condition when the floating force becomes more significant than the surface tension, and the value of it is related to the tangent plane area (Fig. 4.11). For the peak, the surface tangent area is only a dot while for the valley, the surface tangent area is more close to a ring, which makes the surface tension much higher than on the peak area, this makes the bubbles stay longer on the valley area (Fig. 4.12). Some study of bubbles in liquid can be found in Ref. [128, 129].

Hence, bubbles take a longer time to depart from valleys and block the reaction at valleys for a longer time than they do at peaks. This effect enlarges the reaction rate difference and facilitates the generation of a smoother surface.

Figure 4.12: Force on bubbles

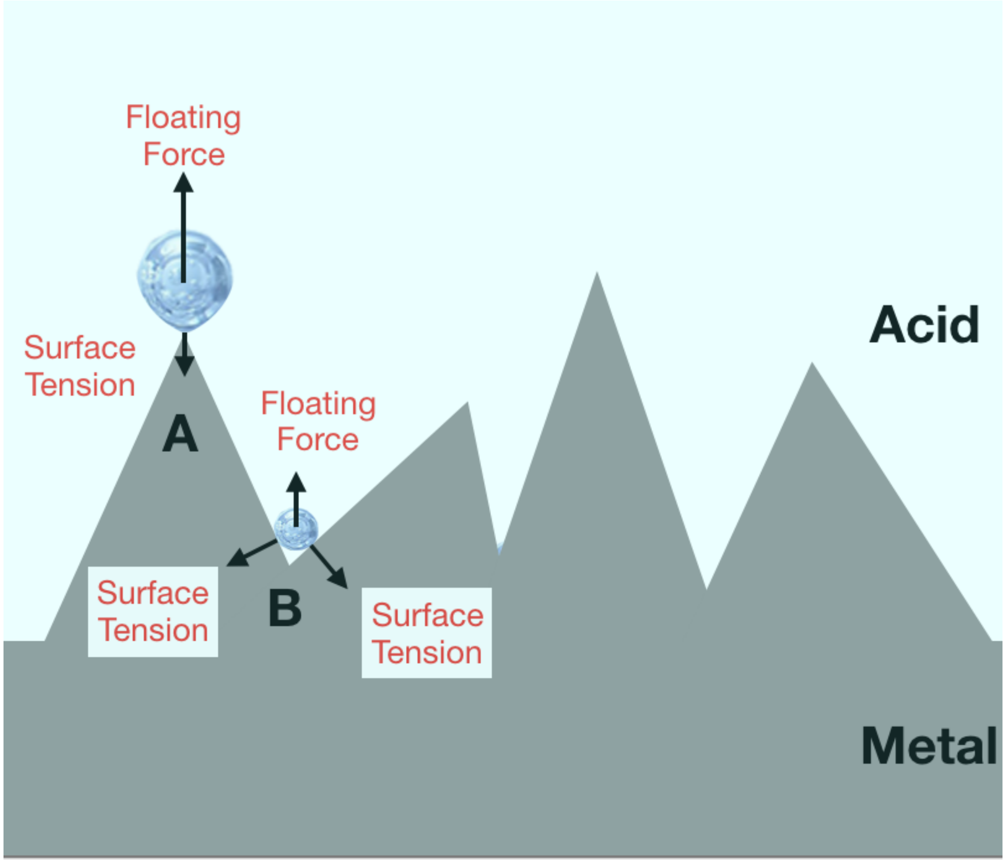

The reaction on Nb of the H_2O_2 plus HF without Cu is:

$$5\,H_2O_2 + 2\,Nb + 10\,HF \longrightarrow 2\,NbF_5 \cdot H_2O + 8\,H_2O. \tag{4.9}$$

One noticeable difference between this reaction (Eqs. 4.9) and the Cu case (Eqs. 4.8) is the O_2 gas generated on Nb surface, and these oxygen gas bubbles may help generate the smooth surface.

Another evidence for that bubbles play a role for the smoothing effect is the Fe catalyst experiment, when there is more Fe, too many bubbles will be generated, and worsen the surface with bubble marks (Fig. 4.10a); when there is less Fe, the result is more close to no catalyst case (Fig. 4.10b).

Unfortunately, we are not able to get an optimized Fe amount to get a smooth Nb surface. We think this is due to Fe ion has less oxidation power, it reacts less than Cu ion in Nb oxidation equation (Eq. 4.7) but react more than Cu ion in the H_2O_2 decomposing equation (Eq. 4.4). Thus if less Fe is added, not enough Fe ion involved in oxidation, while if more Fe added, too many bubbles are generated, and it can hardly get a balance. This also supports our bubble effect explanation.

4.3.3 Micro EP Effect: Electrodes Forming on Nb Surface During Single Displacement Reaction

There is an extra benefit from adding Cu: the Cu generated on Nb surface from Eqs. 4.7 forms cathode, increases the total reaction rate (especially on the peaks because the peaks already react faster [126]) and intensifies the reaction rate difference. This is due to Galvanic corrosion, which is similar to the aluminum case in Ref. [125].

We cannot distinguish which dominate the smoothing process, the bubble effect or the micro EP effect. The Fe ion less oxidation power can also explain the microcurrent effect: less oxidation power induces less micro-current and less peak filed enhancement reactions.

4.4 Copper Remnant Study

Although copper can be found as a catalyst to chemically polish new acids, potential copper contamination is concerned. Instead of analyzing the copper's impact on the Niobium Cavity, we first try to find the possibility of removing the copper from the surface of the Niobium Cavity.

We have mentioned that the Cu only reacts on the Nb surface and in the acid (Eqs. 4.4 to Eqs. 4.7). Energy-dispersive X-ray spectroscopy (EDS) analysis is a method that can detect the elements on the 1000 nm surface of a conductor, and it should be able to analyze the contamination on Nb surface, so we decided to adopt this method to study the Cu remnant.

4.4.1 Experiment and EDS Analysis Result

Five samples were treated with the same optimized acid (copper amount 347 mg/L), and then four of them were rinsed by different acid listed in Table 4.6. We then do the EDS analysis on the samples to check the element on the Nb surface. However, we did not get any Cu signal even on the non-rinsed Nb sample, one example signal spectrum is shown in Fig. 4.14 for Selected Area 1

Table 4.6: Copper remnant removal experiment setup

Sample #	Reaction Amount	Treatment	Time
1	72.5 μm	None	None
2	77 μm	15 mL HF + 40 mL H_2O rinse	5 min
3	76 μm	15 mL HF + 40 mL H_2O rinse	10 min
4	85.5 μm	Mix Acid Without Cu rinse	5 min
5	86 μm	Mix Acid Without Cu rinse	10 min

Figure 4.13: Three selected areas to do the EDS analysis on non-rinsed Nb sample treated with new acid plus Cu catalyst.

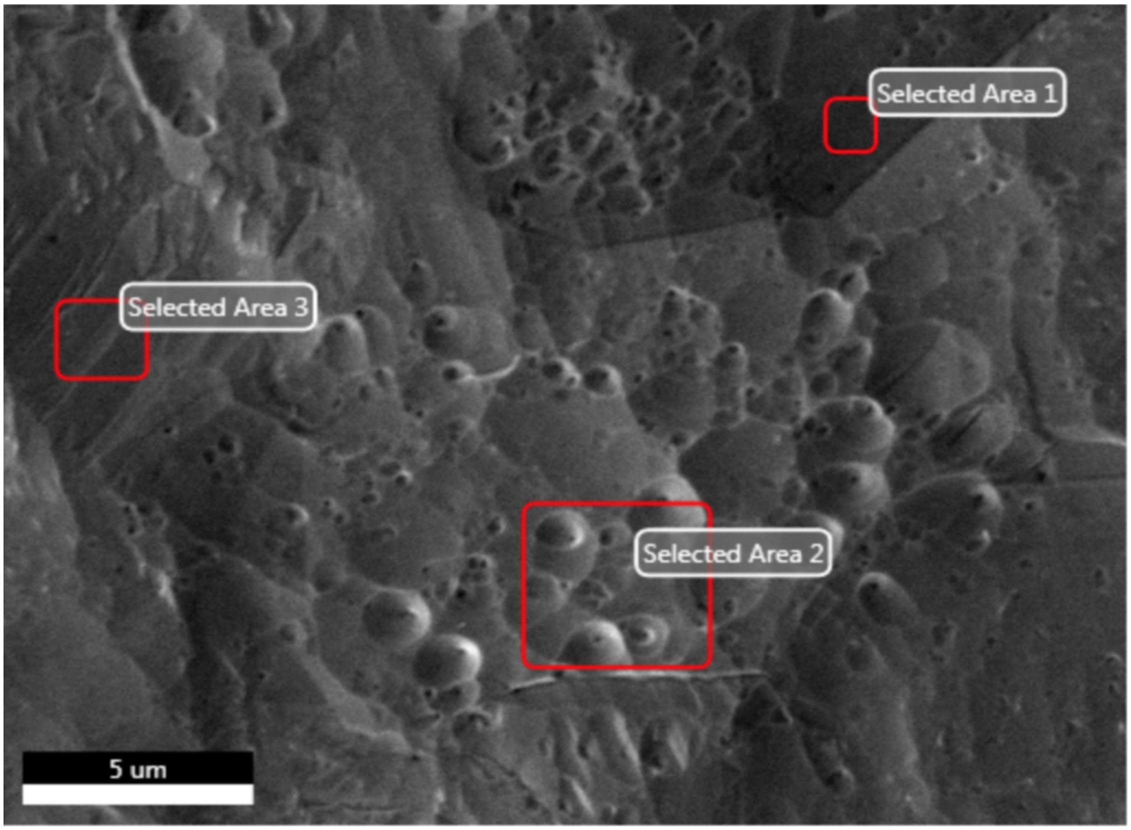

in Fig. 4.13. Other areas have similar signal and shown no Cu. This indicates that the Cu amount is very low and cannot be detected by EDS.

4.5 Discussion

In this chapter, we investigated the new mixture with copper resolved in detail. We have discovered the best optimization between 329 mg/L and 464 mg/L of the resolved copper into the mixture consisted of H_2O_2 (50%, 29 mL, HF (50%, 15 mL), and water (11 mL), total mixture

Figure 4.14: EDS Result of Nb sample after new acid on Selected Area 1 in Fig. 4.13.

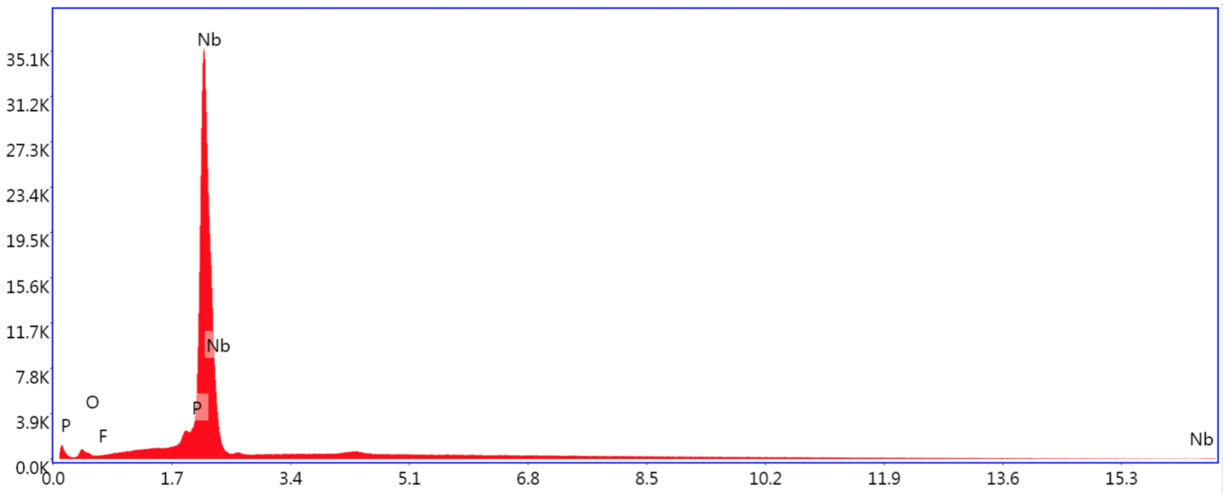

volume 55 mL. This optimized mixed acid can provide almost no preferential etching for enough material removal (70 μm, maybe more), which thanks to the copper catalyst effect. The material-removing speed is $\sim$ 5 μm/min and the finished surface roughness is $\sim$ 3 μm if the initial roughness is adjusted around 2 μm. This etching performance is compatible with that of the current BCP acid (1: 1: 2).

Then we investigated the chemical reactions, found out that the difference between the reactions for with and without Cu catalyst then concluded bubbles during reactions and micro-EP effect enhanced the smoothing effect which improved the roughness to roughness similar to conventional BCP. In the end, we did EDS analysis and found there is no sufficient Cu contamination to get Cu signal on the Nb surface; this indicates the Cu contamination amount is very low and maybe will not influence the future Nb cavity performance.

CHAPTER 5

CONCLUSION AND FURTHER WORK

This dissertation describes the original motive of solving High Field Q Slope (HFQS) problem, which is a phenomenon that the Nb superconducting cavity Quality Factor started drop exponentially when the accelerating gradient reaches a specific value ($B_P = 80 \sim 100$ mT). This HFQS problem is one of the primary limits of Nb cavity performance, especially for those treated with Buffered Chemical Polishing (BCP) method. The process of 120 °C Low-Temperature Baking (LTB) can relief the dropping slope at high electric field especially for the EP processed Nb cavities, which is associated with the oxygen diffusion. However, this LTB method could not provide a solution to the BCP HFQS problem, can only partially improve the slope.

There are several proposed models for this BCP particular degradation; however, none of them can explain the BCp'ed HFQS behavior for cavities made of fine grain, large grain, and single-crystalline niobium material consistently. Instead of their models, we concluded by massive past data mining that nitrogen contamination during BCP should be the root cause of the BCP HFQS, which is caused by the nitric acid in the current BCP acid.

The above conclusion motivated us to develop a nitrogen-free chemical polishing acid for Nb. After the basic chemical polishing method investigation, we decided to use hydrogen peroxide as our oxidizer and continue to use HF as our oxide layer remover in the mixed acid. The hydrogen peroxide has no extra element introduced in the acid, and it has enough oxidization power to react with Nb, this made us adopt it in our new acid development. Our goal for this acid is: getting the reaction to happen with a moderate speed; and with a finishing surface similar to conventional BCP ($R_z \sim 3\ \mu$m).

This dissertation covers the process of acid developing. We firstly tried several experiments outside MSU before we get job safety analysis (JSA) approved with an acid composed of 45 mL 35% H_2O_2 and 10 mL 50% HF with a starting temperature 45 °C. We then try to reproduce the result in MSU after the JSA approval, but we got very high roughness on all result surface.

We started over the process by doing controlling parameters experiments, and tried temperature, stirring or not, temperature maintaining methods, viscosity, component concentration and acid ratio. Most of these influence the reaction ratio but have no improvement on surface roughness. All trials have very high roughness after enough reaction.

We found the high roughness located both in the grain and on grain-boundaries, by comparing results of single-crystal Nb and fine-grain Nb that processed by conventional BCP and our new acid. This means both erosion effect and reaction speed different on different crystal orientation (preferential etching) both exist in the new acid reaction.

We found Cu can be a catalyst in our reaction, which can improve the smoothness, and the operation is merely adding a small amount of Cu in the acid before putting Nb in. We applied the controlling parameter process again, include acid ratio, viscosity and Cu amount, and we eventually found a relatively best recipe, and finally achieve a smooth Nb surface that similar to conventional BCP result.

We studied the mechanism and deducted the chemical reaction formulas. By comparing the reaction with and without Cu, we found the most obvious difference is that the one with Cu has oxygen bubbles generated on the Nb surface. The Cu ions consistently oxidize Nb by metal single displacement reaction and become Cu metal and then dissolve in acid become Cu ion again. There is no Cu consumption in the process, and that is why we think the catalyst is the role of Cu. The Cu is a catalyst of H_2O_2 decomposing. The oxygen bubbles generated on the Nb surface stay in valley longer than on the peak, which generates a reaction speed difference and enhances the polishing process. The single displacement reaction on the Nb surface also generate microcurrent on the Nb surface, which may form Micro-EP effect, and also help improve the surface smoothness.

Thus any metal that: its ion can react with Nb metal by single displacement reaction, and can help with H_2O_2 decomposing, should be able to be our new acid catalyst. We tried Fe, and the results agree with our mechanism analysis.

In the end, we studied the Cu remnant amount. There is no signal of Cu when we do EDS analysis; this means the copper amount is very low and not detectable by EDS. In the future, if some potential degradation still happened on Nb cavities by Cu contamination, it should be easy to remove by reacting a small amount on the surface with the original new acid, because Cu reacts much faster than Nb in the acid. Another possible solution is trying a new catalyst: a superconductor under cavity operation temperatures, such as indium or lead; or use Sn to react with Nb and generate Nb_3Sn on its surface, which is another promising material for SRF cavities. These studies will offer more possibilities for SRF material.

APPENDICES

APPENDIX A

E & M FIELD IN A RF CAVITY

A.1 Field in wave guide

Because of the cylindrical geometry, we can single out the spatial variation of the fields in the z direction, and assume

$$\left.\begin{array}{l}\mathbf{E}(x,y,z,t)\\[1em] \mathbf{B}(x,y,z,t)\end{array}\right\} = \left\{\begin{array}{l}\mathbf{E}(x,y)e^{\pm ikz-i\omega t}\\[1em] \mathbf{B}(x,y)e^{\pm ikz-i\omega t}\end{array}\right. \tag{A.1}$$

Maxwell equations take the coming form:

$$\left\{\begin{array}{l}\nabla\times\mathbf{E} = i\omega\mathbf{B}\\ \nabla\cdot\mathbf{B} = 0\\ \nabla\times\mathbf{B} = -i\mu\epsilon\omega\mathbf{E}\\ \nabla\cdot\mathbf{E} = 0\end{array}\right. \tag{A.2}$$

For our case, both E and B satisfy

$$\left[\nabla_t^2 + (\mu\varepsilon\omega^2 - k^2)\right]\left\{\begin{array}{c}\mathbf{E}\\ \mathbf{B}\end{array}\right\} = 0, \tag{A.3}$$

where

$$\nabla_t^2 = \nabla^2 - \frac{\partial^2}{\partial z^2}. \tag{A.4}$$

Separate the fields into components parallel to and transverse to the z axis,

$$\mathbf{E} = \mathbf{E}_z + \mathbf{E}_t, \tag{A.5}$$

$$\mathbf{E}_z = \hat{z}E_z, \tag{A.6}$$

$$\mathbf{E}_t = (\hat{z}\times\mathbf{E})\times\hat{z}. \tag{A.7}$$

And the same setting for B. Do some calculation, we can get

$$\underbrace{\frac{\partial E_z}{\partial y} + \frac{\partial E_z}{\partial x}}_{\nabla_t \mathbf{E}_z} - \underbrace{(\frac{\partial E_y}{\partial z} + \frac{\partial E_x}{\partial z})}_{-\frac{\partial \mathbf{E}_t}{\partial z}} = \underbrace{i\omega(B_x - B_y)}_{i\omega\hat{z}\times\mathbf{B}_t} \tag{A.8}$$

.

And $\hat{z}\cdot(\nabla_t \times \mathbf{E}_t) = i\omega\mathbf{B}_z$. Do the same thing to $\nabla \times \mathbf{B} = -i\mu\epsilon\omega\mathbf{E}$ and sum up, we can get

$$\frac{\partial \mathbf{E}_t}{\partial z} + i\omega\hat{z}\times\mathbf{B}_t = \nabla_t E_z, \qquad \hat{z}\cdot(\nabla_t \times \mathbf{E}_t) = i\omega B_z, \tag{A.9}$$

$$\frac{\partial \mathbf{B}_t}{\partial z} - i\mu\epsilon\omega\hat{z}\times\mathbf{E}_t = \nabla_t B_z, \qquad \hat{z}\cdot(\nabla_t \times \mathbf{B}_t) = -i\mu\epsilon\omega E_z, \tag{A.10}$$

$$\nabla_t \cdot \mathbf{E}_t = -\frac{\partial E_z}{\partial z}, \quad \nabla_t \cdot \mathbf{B}_t = -\frac{\partial B_z}{\partial z}. \tag{A.11}$$

Considering eq.A.1, we can get

$$\Rightarrow \frac{\partial \mathbf{E}_t}{\partial z} = \nabla_t E_z - i\omega\hat{z}\times\mathbf{B}_t, \tag{A.12}$$

and

$$\Rightarrow \mathbf{E}_t = \frac{i}{\omega^2\mu\epsilon - k^2}(k\nabla_t E_z - \omega\hat{z}\times\nabla_t B_z). \tag{A.13}$$

Use the same method, we can get

$$\mathbf{B}_t = \frac{i}{\omega^2\mu\epsilon - k^2}(k\nabla_t B_z + \mu\epsilon\omega\hat{z}\times\nabla_t E_z). \tag{A.14}$$

Only consider the Transverse Electro-magnetic (TEM) wave, let $E_z = B_z = 0$, $E_t = E_{TEM}$, satisfies

$$\nabla_t \times \mathbf{E}_{TEM} = 0, \quad \nabla_t \cdot \mathbf{E}_{TEM} = 0. \tag{A.15}$$

This means the E_{TEM} is irrotational and no charge, and therefore

$$k = k_0 = \omega\sqrt{\mu\epsilon}, \tag{A.16}$$

$$\mathbf{B}_{TEM} = \pm\sqrt{\mu\epsilon}\hat{z}\times\mathbf{E}_{TEM}. \tag{A.17}$$

In hollow cylinders and on transmission lines at high frequencies, there occur two types of field configuration because of considering eq.1.22, E_z, B_z and the boundary conditions be satisfied. The presence of surface charges and currents at the interface allows the existence of a normal component of $D(D = \epsilon E)$ at the boundary, and also a tangential component of $H(B = \mu H)$, but the tangential component of E and the normal component of B must be continuous across the boundary. The boundary conditions are

$$\mathbf{n} \times \mathbf{E} = 0, \quad \mathbf{n} \cdot \mathbf{B} = 0, \tag{A.18}$$

where n is a unit normal at the surface S. And also

$$E_z|_s = 0, \quad \frac{\partial B_z}{\partial n}|_s = 0. \tag{A.19}$$

A.2 TM mode and TE mode

Since the boundary conditions on E_z and B_z are different, the eigenvalues will in general be different. So the fields are divided into two categories:

Transverse Magnetic(TM) waves $B_z = 0$ everywhere, boundary condition $E_z|_s = 0$.

Transverse Electric(TE) waves $E_z = 0$ everywhere, boundary condition $\frac{\partial B_z}{\partial n}|_s = 0$.

For the propagation of waves inside a hollow waveguide of uniform cross section, the transverse magnetic and electric fields for both TM and TE waves are related by

$$H_t = \frac{\pm 1}{Z} \hat{z} \times E_t, \tag{A.20}$$

where

$$Z = \begin{cases} \dfrac{k}{\epsilon\omega} = \dfrac{k}{k_0}\sqrt{\dfrac{\mu}{\epsilon}} & \text{, (TM mode)} \\ \dfrac{\mu\omega}{k} = \dfrac{k_0}{k}\sqrt{\dfrac{\mu}{\epsilon}} & \text{, (TE mode)} \end{cases} \tag{A.21}$$

and for TM waves

$$\mathbf{E}_t = \frac{\pm ik}{\gamma^2} \nabla_t \psi, \tag{A.22}$$

for TE waves

$$\mathbf{H}_t = \frac{\pm ik}{\gamma^2} \nabla_t \psi, \tag{A.23}$$

where $\psi e^{\pm ikz}$ is $E_z(H_z)$ for TM (TE) waves, and

$$(\nabla_t^2 + \gamma^2)\psi = 0, \tag{A.24}$$

$$\gamma^2 = \mu\epsilon\omega^2 - k^2, \tag{A.25}$$

the boundary conditions are

$$\psi|_s = 0, \quad or \quad \frac{\partial\psi}{\partial n}|_s = 0, \tag{A.26}$$

for TM(TE) modes.

Due to these equations and boundary conditions, there will be a spectrum of eigenvalues that

$${k_\lambda}^2 = \mu\epsilon\omega^2 - {\gamma_\lambda}^2, \tag{A.27}$$

and we can define a cutoff frequency,

$$\omega_\lambda = \frac{\gamma_\lambda}{\sqrt{\mu\epsilon}}. \tag{A.28}$$

Figure A.1: Cutoff frequency

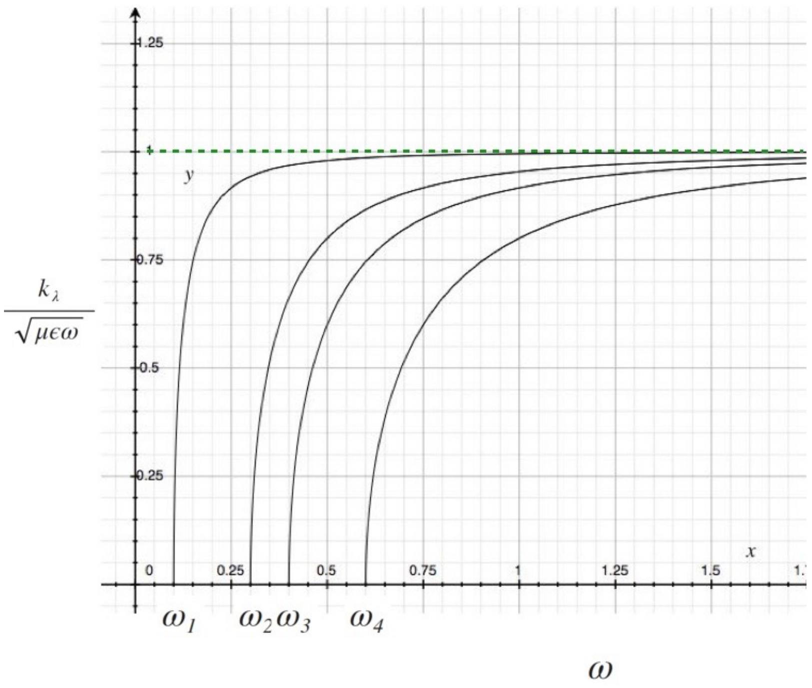

Then the wave number can be written as

$$k_\lambda = \sqrt{\mu\epsilon}\sqrt{\omega^2 - \omega_\lambda^2}. \tag{A.29}$$

For a cylindrical waveguide, because of reflections at the end surfaces, the z dependence of the fields is that appropriate to standing waves:

$$A\sin(kz) + b\cos(kz). \tag{A.30}$$

If the plane boundary surfaces are at z=0 and z=d, the boundary conditions can be satisfied at each surface only if

$$k = p\frac{\pi}{d} \quad (p = 0, 1, 2, ...). \tag{A.31}$$

For TM fields the vanishing of E_t at $z = 0$ and $z = d$ requires

$$E_z = \psi(x, y)\cos(\frac{p\pi z}{d})(p = 0, 1, 2, ...). \tag{A.32}$$

Similar for TE fields, the vanishing of H_z at z=0 and z=d requires

$$H_z = \psi(x, y)\sin(\frac{p\pi z}{d})(p = 0, 1, 2, ...). \tag{A.33}$$

Then we can get for TM fields

$$\mathbf{E}_t = -\frac{p\pi}{d\gamma^2}\sin(\frac{p\pi z}{d})\nabla_t\psi, \tag{A.34}$$

$$\mathbf{H}_t = \frac{i\epsilon\omega}{\gamma^2}\cos(\frac{p\pi z}{d})\hat{z}\times\nabla_t\psi. \tag{A.35}$$

TE fields

$$\mathbf{E}_t = -\frac{i\omega\mu}{\gamma^2}\sin(\frac{p\pi z}{d})\hat{z}\times\nabla_t\psi \tag{A.36}$$

,

$$\mathbf{H}_t = \frac{p\pi}{d\gamma^2}\cos(\frac{p\pi z}{d})\nabla_t\psi, \tag{A.37}$$

and consequently

$$\gamma^2 = \mu\epsilon\omega^2 - (\frac{p\pi}{d})^2, \tag{A.38}$$

and

$$\omega_{\lambda p}^2 = \frac{1}{\mu\epsilon}\left[\gamma_\lambda{}^2 + (\frac{p\pi}{d})^2\right]. \tag{A.39}$$

The cylinder waveguide, with radius R and length d, for a TM mode the transverse wave equation for $\Psi = E_z$, subject to the boundary condition $E_z = 0$ at $\rho = R$ has the solution

$$\psi(\rho, \phi) = E_0 J_m(\gamma_{mn}\rho)e^{\pm im\phi}, \tag{A.40}$$

where

$$\gamma_{mn} = \frac{x_{mn}}{R}, \tag{A.41}$$

x_{mn} is the n th root of the equation,$J_m(x) = 0$. The integers m and n take on the values m=0,1,2,..., n=1,2,3,... The resonance frequencies are given by

$$\omega_{mnp} = \frac{1}{\sqrt{\mu\epsilon}}\sqrt{\left[\frac{x_{mn}^2}{R^2} + (\frac{p\pi}{d})^2\right]}. \tag{A.42}$$

For TE modes, the boundary condition on

$$H_z[\frac{\partial\psi}{\partial\rho}|_R] = 0, \tag{A.43}$$

gives

$$\gamma_{mn} = \frac{x'_{mn}}{R}, \tag{A.44}$$

so that

$$\omega_{mnp} = \frac{1}{\sqrt{\mu\epsilon}}\sqrt{\left[\frac{{x'_{mn}}^2}{R^2} + (\frac{p\pi}{d})^2\right]}. \tag{A.45}$$

Almost every RF cavity operates using the TM$_{010}$ accelerating mode. This mode has a longitudinal electric field E_z in the center of the cavity and is the lowest mode, which can accelerate the beam.

So that

$$\omega_{010} = \frac{1}{\sqrt{\mu\epsilon}}\sqrt{\left[\frac{x_{m=0,n=1}^2}{R^2} + (\frac{0\times\pi}{d})^2\right]} = \frac{2.405}{\sqrt{\mu\epsilon}R}. \tag{A.46}$$

we can see the frequency is independent of d in this mode, and we can get

$$\begin{aligned} R &= \frac{2.405}{\sqrt{\mu\epsilon}\times\omega_{010}} = \frac{2.405}{\sqrt{\mu\epsilon}\times 2\pi f} = \frac{2.405\times c}{2\pi f} \\ &= \frac{2.405\times 3\times 10^8 m/s}{2\times 3.14\times 1.3\times 10^9 Hz} = 0.0884 \text{ m}, \end{aligned} \tag{A.47}$$

for f = 1.3 GHz, we can choose d half of the wavelength, so that

$$d = \frac{\lambda}{2} = \frac{c}{2f} = \frac{3\times 10^8 m/s}{2\times 1.3\times 10^9 Hz} = 0.1153 \text{ m}. \tag{A.48}$$

In reality, when calculate the geometrical factor on the Pill Box cavity, the value is 263 Ω. The real cavity shape is optimized using computer codes like Superfish (2D), CST Studio (3D). The real cavity shape case for ILC cavity, the geometrical factor is 270 Ω.

The expressions for TM$_{010}$ mode fields are

$$E_z = E_0 J_0(\frac{2.045\rho}{R})e^{-i\omega t}, \tag{A.49}$$

$$H_{\psi} = -i\sqrt{\frac{\epsilon}{mu}}E_0 J_1(\frac{2.045\rho}{R})e^{-i\omega t}. \tag{A.50}$$

In Fig.A.2, Fig.A.3, Fig.A.4, Fig.A.5,we can see the field distribution in TM$_{010}$ mode.

Figure A.2: TM$_{010}$ mode

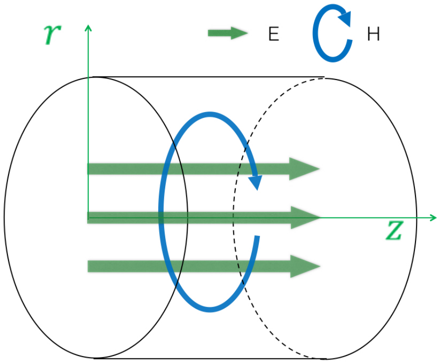

Figure A.3: E_z Vs d

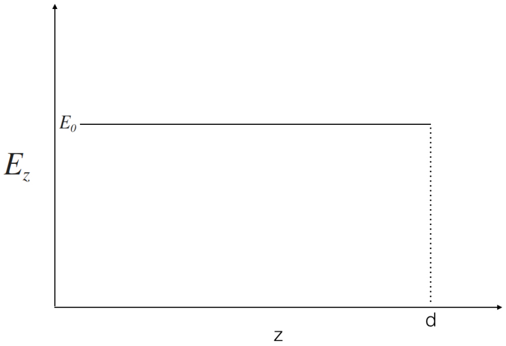

And for TM$_{020}$ mode, in Fig. A.6, we can see the E direction change when off the center.

For TE moodes, the lowest one is TE$_{111}$, the resonance frequency is:

$$\omega_{111} = \frac{1.841}{\sqrt{\mu\epsilon}R}\sqrt{\left[1 + 2.912(\frac{R}{d})^2\right]}. \tag{A.51}$$

For large d, (d > 2.03 R), the resonance frequency ω_{111} is smaller than that for the lowest TM mode. And because the frequency depends on the ratio d/R, it's possible to provide easy tuning by making the separation of the end faces adjustable. Detailed deduction can be found in Ref. [42].

Figure A.4: E_z Vs θ

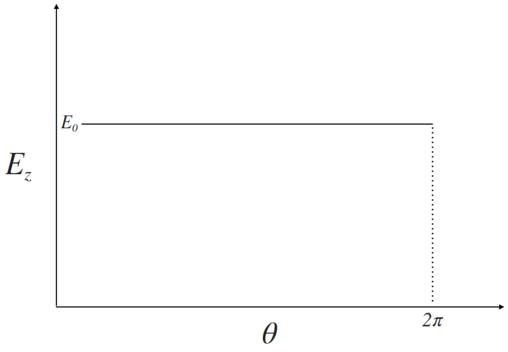

Figure A.5: E_z Vs r

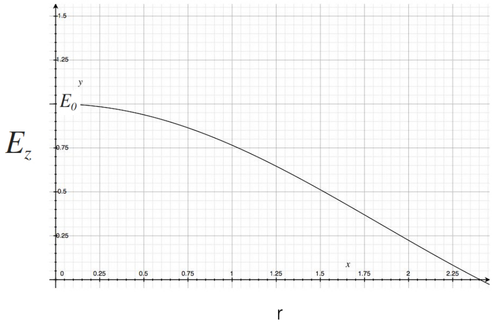

Figure A.6: TM$_{020}$ mode

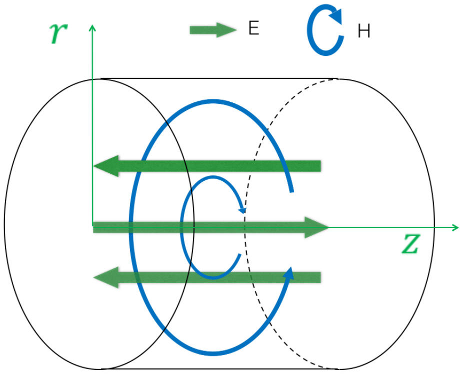

APPENDIX B

CRYOMODULE SOLENOID TEST IN FRIB

B.1 Cryomodules

In the FRIB cryomodules, superconducting solenoid packages for transverse focusing and steering are interspersed with the cavities. An example is shown schematically in Fig. B.1: the $\beta = 0.085$ QWR cryomodule (CM) contains 8 cavities and 3 superconducting solenoid packages. This cryomodule is similar to the cryomodules fabricated for the MSU re-accelerator, ReA3 [130]. An important feature of the cryomodule design is the local magnetic shielding around the SRF cavities [131]. The shields operate at cryogenic temperature ($\simeq 25$ K). Some parameters of the solenoid packages in FRIB are listed in Tab. B.1.

The cavities and solenoid packages are certified individually via Dewar tests prior to assembly onto the cold mass. After assembly of the cold mass into the cryomodule, the cavities and solenoids are tested again in situ. For the solenoid packages, the goal is to make sure that all of the coils can reach the FRIB design requirements (Table B.1), can operate stably and robustly, and do not adversely impact the SRF cavity performance. There are several considerations for the test:

- Energizing test of superconducting solenoid in the cryomodule bunker test handles high current ~ 90 A and have to be concerned safety. It potentially causes magnet quenches, which will make a damage on the solenoid magnet.

Figure B.1: Layout of FRIB-1 Cryomodule (CM-1). C: cavity (green); S: solenoid package (blue). Cavities 1 - 4 are shielded by mu-metal (black) and Cavities 4 - 8 are shielded by A4K (red).

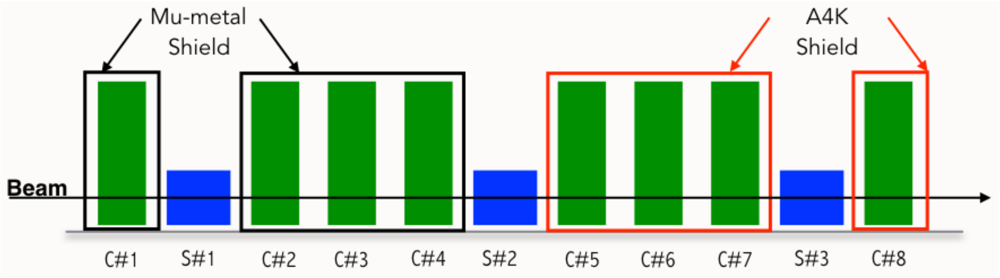

Table B.1: FRIB 50 cm solenoid package design requirements. The fringe field requirement applies at the magnetic shield.

Operating temperature	$4.5 + 0.5/{-0.0}$ K
Solenoid nominal current	≤ 90.9 A
$\int B^2 dz$	$\geq 13.6\ \mathrm{T^2 \cdot m}$
Peak solenoid field on beam axis	≥ 8.0 T
Fringe field	≤ 270 gauss

- Magnet quench will be a problem with safety by the highly vaporized helium gas pressure in the worst case.
- Because of the close proximity, the influence of the solenoid fringe field on cavity performance is a major concern.

This document describes the solenoid test procedures, mu-metal replacement of original shielding material effectiveness, an example of solenoid test result and the solenoid package CS-Studio automatic scan files.

B.2 FRIB Solenoid Package

The solenoid package is designed for focusing and steering the beam with fringe field compensation [132]. Figure B.2 shows a model of the coils, including the 8 T main solenoid, the two bucking coils for fringe field cancellation, and the two steering dipole coils. The model was made using CST Studio[1]. All of the coils are made of NbTi superconducting wire. The bucking coils are designed to reduce the fringe field to ~ 270 gauss at the magnetic shield. The bucking coils produce a field of 0.06 T, and are wired in series with the main solenoid, with a nominal current of 90 A [132].

B.3 Local Magnetic Shield

As discussed above and illustrated in Figure B.1, the SRF cavities are enclosed by local magnetic shields. This approach has two benefits: lower material cost for the shields, and better shielding of

---

[1] Computer Simulation Technology AG, Darmstadt, Germany

Figure B.2: CST Studio model of the 50 cm solenoid package. Inner cylinder: main solenoid; intermediate rectangles: dipoles; outer rings: bucking coils. The diameter is 39 cm.

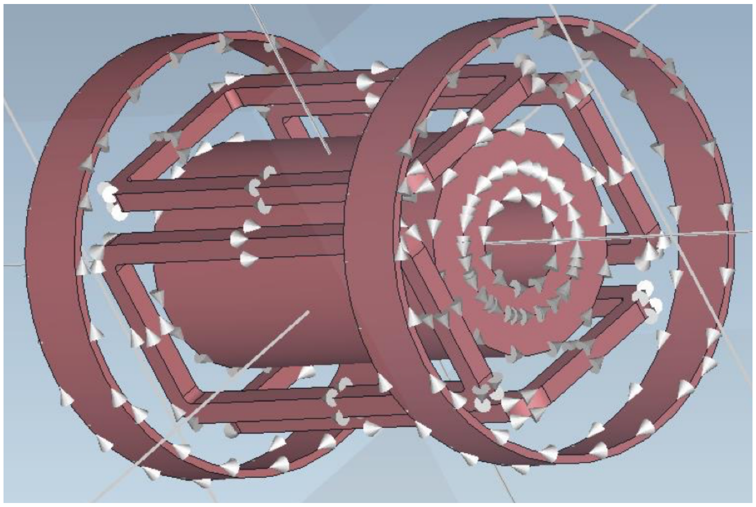

Table B.2: FRIB magnetic shield parameters.

Magnetic permeability μ	$\geq$ 10 000 at 25 K
Thickness	1 mm for QWR

the cavities from the remnant magnetic field in the cryomodule.

The need to mitigate the fringe field's effect on the SRF cavity performance sets the shield requirements. For the FRIB QWRs, the magnetic field at the cavity must be $\leq$ 15 milligauss. Fringe fields higher than $\simeq$ 300 gauss cannot be screened by the shield, hence they will produce a drop in the cavity quality factor after a cavity quench. The magnetic shield requirements are summarized in Table B.2.

For the ReA3 cryomodules, the local shields were made of A4K material, with $\mu > 10\ 000$ even at cryogenic temperature ($\simeq$ 25 K). However, a recent analysis [131] showed that mu-metal of thickness 1 mm with $\mu > 9000$ at $\simeq$ 25 K can meet the shielding requirements for the FRIB QWRs. Since cryogenic magnetic shields such as Cryoperm and A4K are very expensive compared to mu-metal, switching to mu-metal is economically advantageous, if mu-metal can provide adequate shielding. To evaluate the shielding performance of mu-metal relative to A4K, CM-1 includes shields of both types, as shown in Fig. B.1.

Figure B.3: Diagram of the cooling system for cryomodule testing.

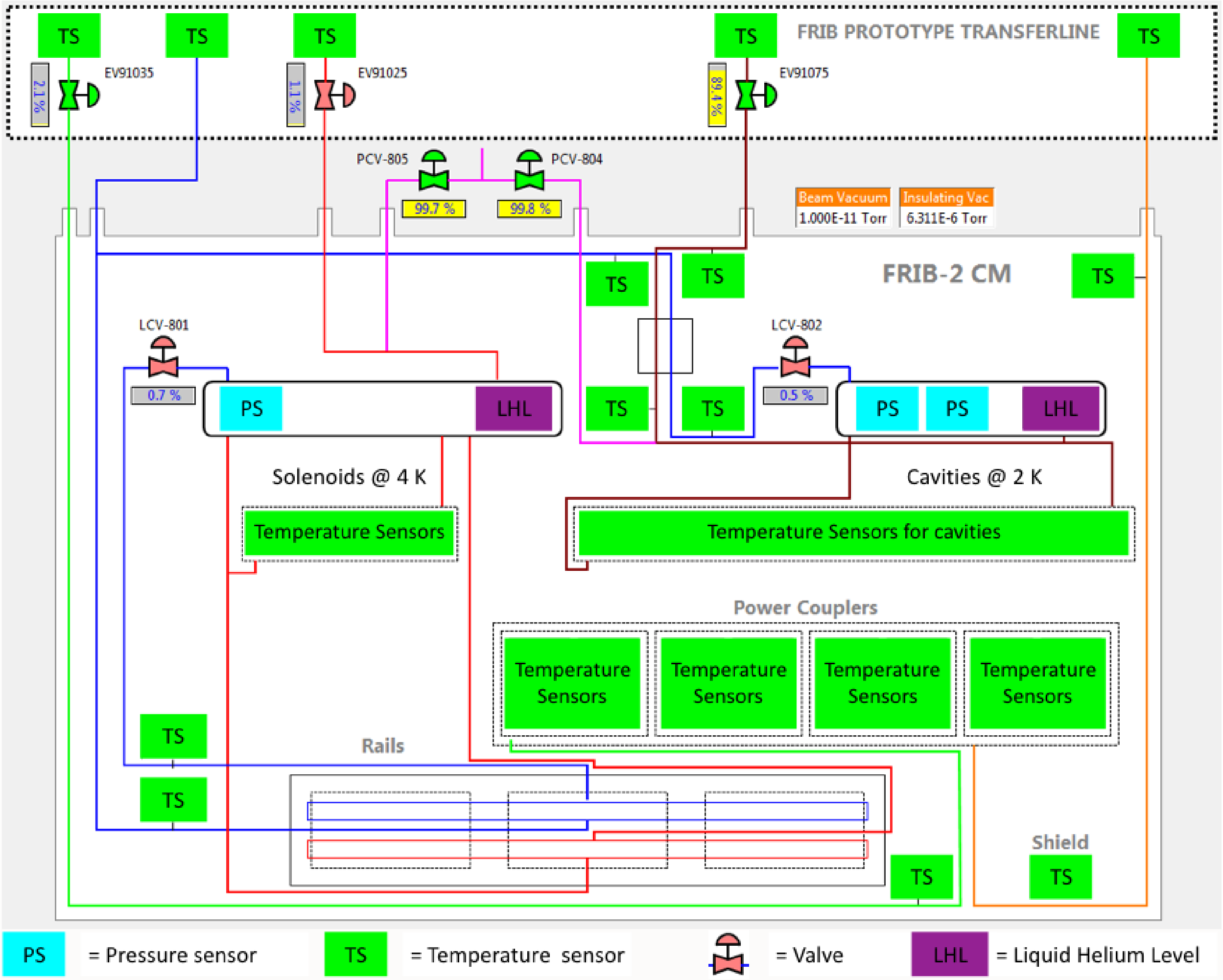

B.3.1 Cryomodule Test System

Figure B.3 shows a diagram of the cryogenic circuit for cryomodule testing. The cavities and solenoid packages are cooled via independent supply lines. The cavities are cooled to 2 K and the solenoid packages are cooled to 4.5 K. The current leads for the solenoid and dipoles are made of high-temperature superconductor (HTS) wires, cooled by helium gas from the solenoid header. The helium gas flow rate is controlled with a Proportional-Integral-Derivative (PID) loop based on the measured current lead voltage. As only one set of power supplies is available for the cryomodule test, one solenoid package is energized at a time.

B.4 Cryomodule Test Procedures

1. Energizing readiness check for the superconducting package: 1, Current calibration for magnet sources; 2, Magnet cable connection; 3, Resistance measurement for the connection; 4, Control system checking at a low current (2 A) prior to the solenoid test .

2. Magnet exciting system check: 1, protection cover on the Top can; 2, Open the water valve to cool the current sources behind the rack and Connect the gas cooling control cable in the bunker; 3, Set file names for data tracking and save the file to “srftest” folder; 4, Set the helium gas flow rate and switch the system to“Auto”.

3. Main solenoid excitation: gradually increase the current to 60 A with a 10 A step at the ramping rate 0.2 A/s and watch the voltage drop below 3 mV and insulation vacuum carefully. When stable, continually increasing the current to maximum (90 A or 91 A) with a 5 A step.

4. Main solenoid operation: 1, Hold the solenoid current at the max for at least 10 min; 2, change the current setting to negtive maximum with the same ramping rate and hold for 10 min; 3, set to 0 A with 0.3 A/s ramping rate.

5. Bending corrector (dipole X for vertical bending and dipole Y for horizontal bending) operation test, this is similar to the main solenoid excitation and operation: set the ramping rate to 0.3 A/s, increase the current to 15 A with a 5 A step and then increase to 19 A with 1 A step; hold for 5 min, switch to -19 A and hold for another 5 min, then set to 0 A; then repeat this for the other dipole.

6. Polarization Check by measuring the fringe field direction outside cryomodule. Sometimes the cable for dipole x and y are switched, and need to be verified.

7. Solenoid and dipoles integrated operation test, this is the demonstration of full magnet operation under the mutual fields and to make sure the mechanical robustness on the magnet frame. The running pattern is same as CM-1 example that shown in Fig. B.4.

8. All magnets and two cavities (acceleration gradient at about 5 MV/m) integrated operation test, this process simulates the cryomodule operation in the tunnel. The running pattern is same as CM-2 example that shown in Fig. B.5.
9. Turn off cavities and degauss the magnets: repeatly set negative 75% of the maximum for all the magnets until less than 0.1 A and then set to 0 A.
10. Turn off system, disconnect cables and close valve.

B.5 Example: CM-1 Solenoid Package Test

In the CM-1 test, we were able to energize all of the coils in all of the solenoid packages to their operating currents (Table B.1). The gas cooling of the HTS leads was adequate, with lead voltage drops below 40 mV.

Figure B.4 shows the magnet currents as a function of time for one of the solenoid packages during the test. The main solenoid and dipoles were operated individually and collectively. The magnets were ramped to their nominal currents with both polarities (±90 A for the solenoid, ±20 A for the dipoles). Different ramp rates were used, up to 0.5 A/s, to check the PID capability. We observed no magnet quenches during the tests, which indicates that the solenoid packages operate robustly.

The solenoid package and the nearest two cavities were turned on for one hour to test the influence of the solenoid package operation on the cavity performance. This test was repeated for each solenoid package. In all cases, no degradation in cavity performance was observed. This indicates that both mu-metal and A4K provide adequate shielding of the fringe field. A cavity quench test was not done due to administrative limits on the cavity fields. After the coils were energized, the solenoid package was demagnetized (see the last hour in Figure B.4 for an example).

The dynamic heat loads of the cavities at 2 K were measured to evaluate their shielding. The results are summarized in Table B.3. No systematic differences were seen between the A4K shields and the mu-metal shields. Thus, the mu-metal shielding of QWRs was successfully validated.

Figure B.4: Coil currents as a function of time for part of the solenoid tests in CM-1.

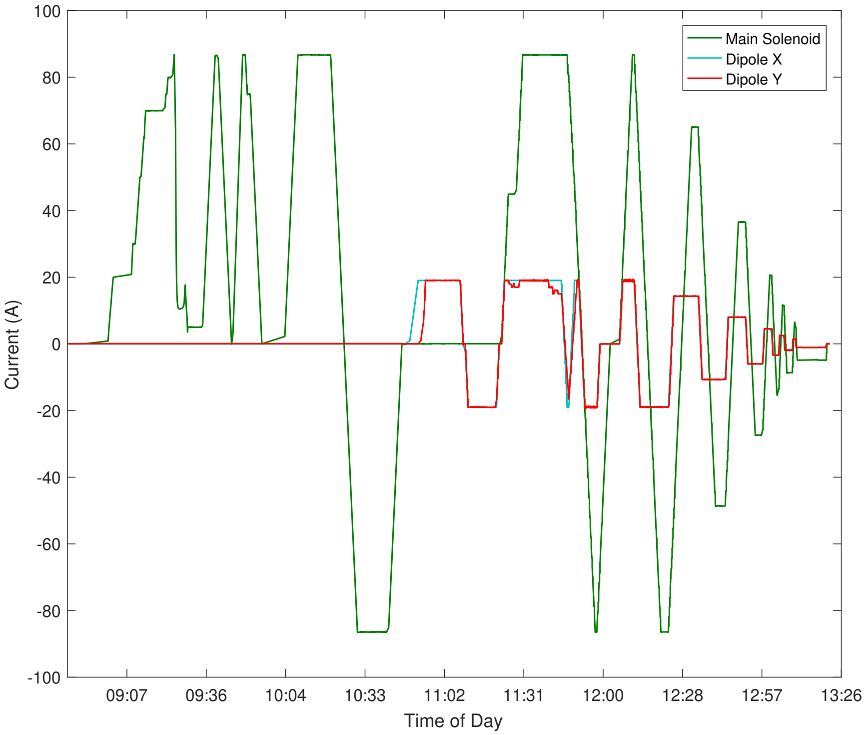

B.6 CM-2 Solenoid Package Test

CM-2 contains the first lot of 50 cm solenoid packages produced from a vendor; all of the cavities are shielded with A4K. The testing procedure for CM-2 was the same as that of CM-1. Figure B.5 shows some results from the CM-2 test. All 3 solenoid packages were tested without quenches. The stable and robust operation indicates that the vendor-produced solenoid packages do not affect the cavity performance.

Figure B.6 shows an example of the PID control for the He gas flow to cool the current leads as the solenoid is ramped up at 0.3 A/s. The PID control works very well.

B.7 Automatic Test Using CS-Studio Scan Files

CS-studio Scan System supports several commands and can easily automated operations in beam controlling. This inspires us to develop several scan files for solenoid package test, which

Figure B.5: Coil currents as a function of time for part of the solenoid tests in CM-2. The two adjacent cavities were turned on between 15:08 and 16:06.

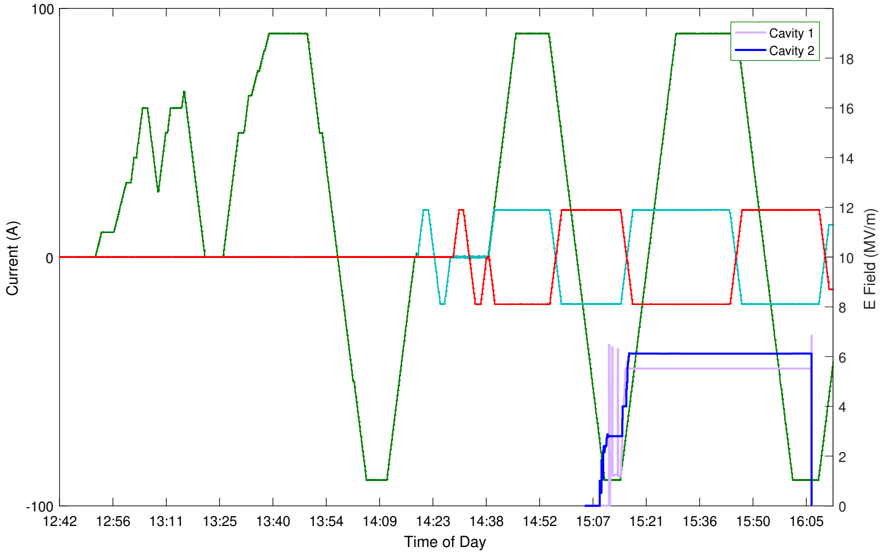

Figure B.6: Example of PID control while ramping the solenoid current at 0.3 A/s. The set point is a voltage drop of 30 mV.

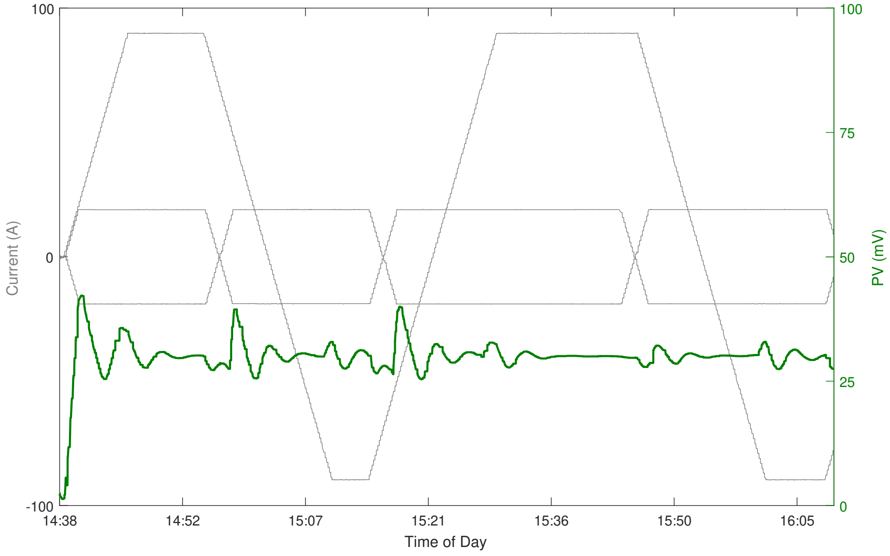

Table B.3: Dynamic heat load of CM-1 cavities at 2 K. Measurements were done at the nominal accelerating gradient of 5.6 MV/m (except for C#1, which was at 7 MV/m, having an initially miscalibrated field level).

Cavity	Dynamic heat load (W)	Shielding Material
C#1	6.2	Mu-metal
C#2	2.4	Mu-metal
C#3	2.5	Mu-metal
C#4	1.0	Mu-metal
C#5	2.4	A4K
C#6	2.5	A4K
C#7	2.4	A4K
C#8	2.6	A4K

Figure B.7: Example of CS-Studio scan system operation window

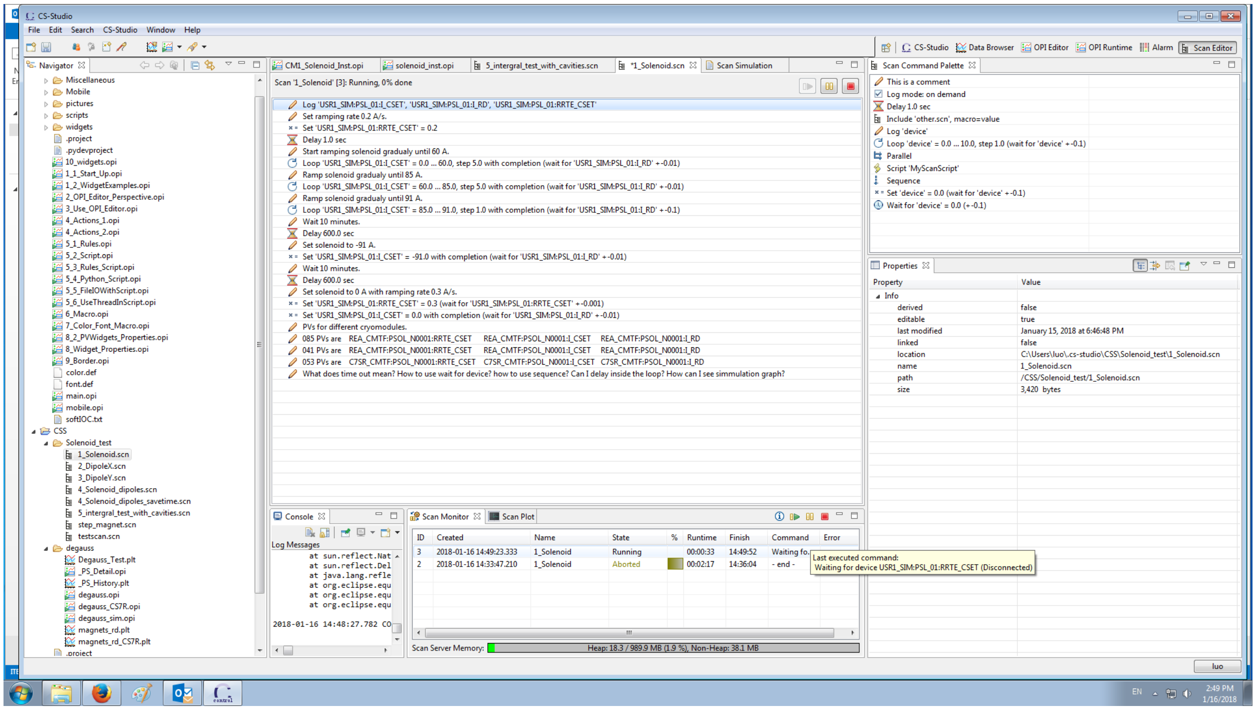

Scan '1_Solenoid' [3]: Running, 0% done

```
Log 'USR1_SIM:PSL_01:I_CSET', 'USR1_SIM:PSL_01:I_RD', 'USR1_SIM:PSL_01:RRTE_CSET'
Set ramping rate 0.2 A/s.
Set 'USR1_SIM:PSL_01:RRTE_CSET' = 0.2
Delay 1.0 sec
Start ramping solenoid gradualy until 60 A.
Loop 'USR1_SIM:PSL_01:I_CSET' = 0.0 ... 60.0, step 5.0 with completion (wait for 'USR1_SIM:PSL_01:I_RD' +-0.01)
Ramp solenoid gradualy until 85 A.
Loop 'USR1_SIM:PSL_01:I_CSET' = 60.0 ... 85.0, step 5.0 with completion (wait for 'USR1_SIM:PSL_01:I_RD' +-0.01)
Ramp solenoid gradualy until 91 A.
Loop 'USR1_SIM:PSL_01:I_CSET' = 85.0 ... 91.0, step 1.0 with completion (wait for 'USR1_SIM:PSL_01:I_RD' +-0.1)
Wait 10 minutes.
Delay 600.0 sec
Set solenoid to -91 A.
Set 'USR1_SIM:PSL_01:I_CSET' = -91.0 with completion (wait for 'USR1_SIM:PSL_01:I_RD' +-0.01)
Wait 10 minutes.
Delay 600.0 sec
Set solenoid to 0 A with ramping rate 0.3 A/s.
Set 'USR1_SIM:PSL_01:RRTE_CSET' = 0.3 (wait for 'USR1_SIM:PSL_01:RRTE_CSET' +-0.001)
Set 'USR1_SIM:PSL_01:I_CSET' = 0.0 with completion (wait for 'USR1_SIM:PSL_01:I_RD' +-0.01)
PVs for different cryomodules.
085 PVs are   REA_CMTF:PSOL_N0001:RRTE_CSET    REA_CMTF:PSOL_N0001:I_CSET    REA_CMTF:PSOL_N0001:I_RD
041 PVs are   REA_CMTF:PSOL_N0001:RRTE_CSET    REA_CMTF:PSOL_N0001:I_CSET    REA_CMTF:PSOL_N0001:I_RD
053 PVs are   C7SR_CMTF:PSOL_N0001:RRTE_CSET   C7SR_CMTF:PSOL_N0001:I_CSET   C7SR_CMTF:PSOL_N0001:I_RD
What does time out mean? How to use wait for device? how to use sequence? Can I delay inside the loop? How can I see simmulation graph?
```

```
This is a comment
Log mode: on demand
Delay 1.0 sec
Include 'other.scn', macro=value
Log 'device'
Loop 'device' = 0.0 ... 10.0, step 1.0 (wait for 'device' +-0.1)
Parallel
Script 'MyScanScript'
Sequence
Set 'device' = 0.0 (wait for 'device' +-0.1)
Wait for 'device' = 0.0 (+-0.1)
```

Property	Value
Info	
derived	false
editable	true
last modified	January 15, 2018 at 6:46:48 PM
linked	false
location	C:\Users\luo\.cs-studio\CSS\Solenoid_test\1_Solenoid.scn
name	1_Solenoid.scn
path	/CSS/Solenoid_test/1_Solenoid.scn
size	3,420 bytes

```
        at sun.reflect.Nat
        at sun.reflect.Del
        at java.lang.refle
        at org.eclipse.equ
        at org.eclipse.equ
        at org.eclipse.equ

2018-01-16 14:48:27.782 CO
```

ID	Created	Name	State	%	Runtime	Finish	Command	Error
3	2018-01-16 14:49:23.333	1_Solenoid	Running		00:00:33	14:49:52	Waiting fo.	
2	2018-01-16 14:33:47.210	1_Solenoid	Aborted		00:02:17	14:36:04	- end -	

Last executed command:
Waiting for device USR1_SIM:PSL_01:RRTE_CSET (Disconnected)

Scan Server Memory: Heap: 18.3 / 989.9 MB (1.9 %), Non-Heap: 38.1 MB

will save the testing time and avoid input errors. The easily aborting and editing properties also made it safe to use (Fig. B.7). We simply reproduce the procedures in the scan files we made. A example of integral test scan file is shown in Fig. B.8.

This process is the automatic version for the test steps talked before, PV values are preset in the scan files so that we can save time for input values every single time during the test.

Figure B.8: Integral test scan file, REA_CMTF:PSOL_N0001:I_CSET is the solenoid current setting, REA_CMTF:PSC1_N0001:I_CSET is the corrector 1 (dipole y) current setting, and the other is the REA_CMTF:PSC1_N0001:I_CSET is the corrector 2 (dipole x) current setting.

```
<commands>
  <config_log>
    <automatic>false</automatic>
  </config_log>
  <log>
    <devices>
      <device>REA_CMTF:PSOL_N0001:I_CSET</device>
      <device>REA_CMTF:PSOL_N0001:I_RD</device>
      <device>REA_CMTF:PSC1_N0001:I_CSET</device>
      <device>REA_CMTF:PSC1_N0001:I_RD</device>
      <device>REA_CMTF:PSC2_N0001:I_CSET</device>
      <device>REA_CMTF:PSC2_N0001:I_RD</device>
    </devices>
  </log>
  <comment>
    <text>Ramp solenoid and dipoles to maximum.</text>
  </comment>
  <set>
    <device>REA_CMTF:PSOL_N0001:I_CSET</device>
    <value>91.0</value>
    <wait>false</wait>
    <tolerance>0.4</tolerance>
  </set>
  <delay>
    <seconds>10.0</seconds>
  </delay>
  <set>
    <device>REA_CMTF:PSC1_N0001:I_CSET</device>
    <value>19.0</value>
    <wait>false</wait>
    <tolerance>0.2</tolerance>
  </set>
  <delay>
    <seconds>10.0</seconds>
  </delay>
  <set>
    <device>REA_CMTF:PSC2_N0001:I_CSET</device>
    <value>19.0</value>
    <readback>REA_CMTF:PSC2_N0001:I_RD</readback>
    <tolerance>0.2</tolerance>
  </set>
  <set>
    <device>REA_CMTF:PSOL_N0001:I_CSET</device>
    <value>91.0</value>
    <readback>REA_CMTF:PSOL_N0001:I_RD</readback>
    <tolerance>1.0</tolerance>
  </set>
  <delay>
    <seconds>300.0</seconds>
  </delay>
  <comment>
    <text>Ramp dipoles until negative maximum.</text>
  </comment>
  <set>
    <device>REA_CMTF:PSC1_N0001:I_CSET</device>
    <value>-19.0</value>
    <wait>false</wait>
    <tolerance>0.2</tolerance>
  </set>
  <delay>
    <seconds>10.0</seconds>
  </delay>
  <set>
    <device>REA_CMTF:PSC2_N0001:I_CSET</device>
    <value>-19.0</value>
    <readback>REA_CMTF:PSC2_N0001:I_RD</readback>
    <tolerance>0.2</tolerance>
  </set>
  <delay>
    <seconds>300.0</seconds>
  </delay>
  <set>
    <device>REA_CMTF:PSOL_N0001:I_CSET</device>
    <value>-91.0</value>
    <readback>REA_CMTF:PSOL_N0001:I_RD</readback>
    <tolerance>1.0</tolerance>
  </set>
  <comment>
    <text>Ramp dipoles until maximum.</text>
  </comment>
  <set>
    <device>REA_CMTF:PSC1_N0001:I_CSET</device>
    <value>19.0</value>
    <wait>false</wait>
    <tolerance>0.2</tolerance>
  </set>
  <delay>
    <seconds>10.0</seconds>
  </delay>
  <set>
    <device>REA_CMTF:PSC2_N0001:I_CSET</device>
    <value>19.0</value>
    <readback>REA_CMTF:PSC2_N0001:I_RD</readback>
    <tolerance>0.2</tolerance>
  </set>
  <delay>
    <seconds>300.0</seconds>
  </delay>
  <set>
    <device>REA_CMTF:PSC1_N0001:I_CSET</device>
    <value>-19.0</value>
    <wait>false</wait>
    <tolerance>0.2</tolerance>
  </set>
  <delay>
    <seconds>10.0</seconds>
  </delay>
  <set>
    <device>REA_CMTF:PSC2_N0001:I_CSET</device>
    <value>-19.0</value>
    <readback>REA_CMTF:PSC2_N0001:I_RD</readback>
    <tolerance>0.2</tolerance>
  </set>
  <delay>
    <seconds>30.0</seconds>
  </delay>
  <comment>
    <text>Ready to do degaussing.</text>
  </comment>
</commands>
```

B.8 Conclusion

We introduced FRIB cryomodule, include solenoid packages design and test procedures, and showed examples in the first two FRIB cryomdules. In the first cryomodule test, we verified that our in-house designed and fabricated solenoid packages meet FRIB specifications for field performance and stable operation. We found that mu-metal is a viable alternative to A4K for local magnetic shielding in FRIB cryomodules. Since the A4K magnetic shields for the FRIB $\beta = 0.085$ cryomodules have already been ordered, we will use mu-metal for other FRIB cryomodules ($\beta = 0.041, 0.290$, and 0.53), which will result in a substantial cost reduction. In the second cryomodule test, we successfully validated the performance and stable operation of vendor-produced solenoid packages.

APPENDIX C

STUDY FOR LOW FIELD Q SLOPE ISSUE IN FRIB

FRIB requires a 200 MeV per nucleon driver linac with a total of 332 superconducting radio-frequency (SRF) cavities of 4 different types: β = 0.041 quarter wave resonators (QWRs, 12 cavities), β = 0.085 QWRs (100 cavities), β = 0.29 half wave resonators (HWRs, 72 cavities) and β = 0.53 HWRs (148 cavities). The 2 K test of superconducting quater-wave resonator (QWR) of FRIB, especially the resonator with β = 0.085, was found to have a significant Q-factor decrease in the low field region (E_{acc} < 2 Mv/m), as shown in Fig. C.1. This appendix discussed the reason of this degradation and the method to study it.

Figure C.1: Q Vs. E_{acc} for an example of FRIB β = 0.085 QWR. Q has sharply dropping in E_{acc} < 2 Mv/m region for the 2 K test case.

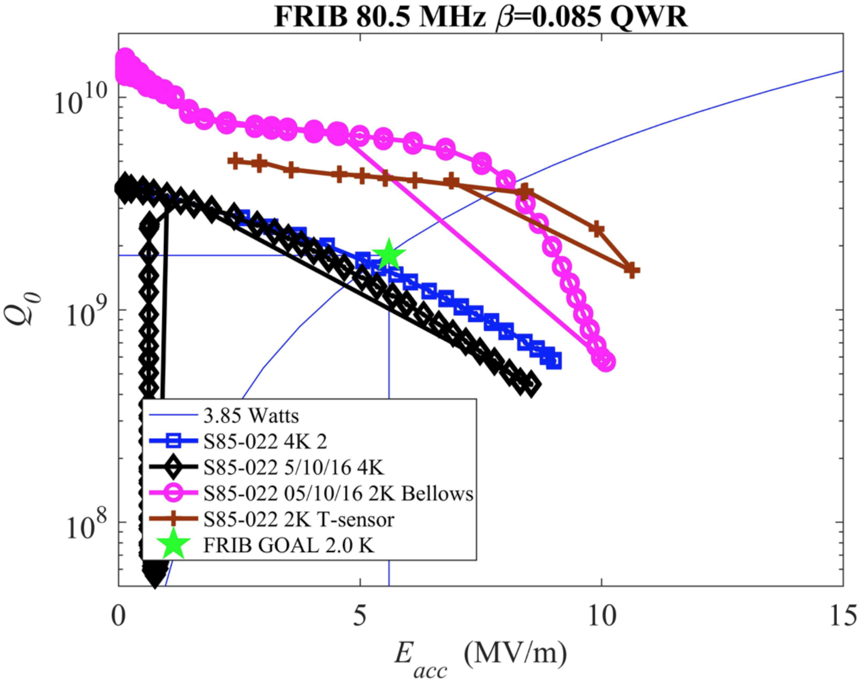

Figure C.2: R_S Vs. 1/T for for the same $\beta = 0.085$ QWR in Fig. C.1. There is a transit point of this result on 1/T = 0.31 (K^{-1}) region, which is around indium superconducting transit temperature T = 3.4 K.

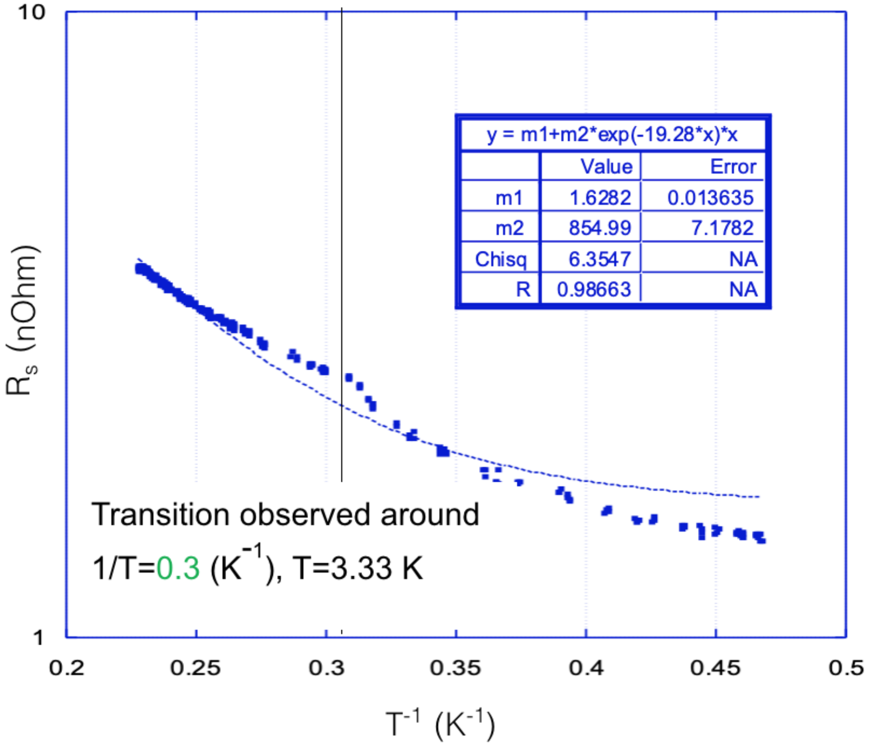

C.1 Transit Point

We noticed for some test results of the QWRs, the R_s Vs 1/T curve during decreasing temperature from 4 K test to 2 K test at E$_{acc}$ ~ 2 MV/m has a turning point located at ~ T = 3.4 K region (Fig. C.2), this matches the indium metal superconducting transit point.

Indium wire is used as sealing between the cavity body and the bottom flange on the FRIB QWRs. This structure was designed to be performed High Pressure water rinsing, which could increase the quality factor of the QWRs significantly.

The indium sealing made the cavity has two superconductor exposed to RF field, with transit temperature at 3.4 K for indium and 9.26 K for niobium. The T = 3.4 K located in the range of operation temperature 4 K and 2K, so the transit point of normal conducting In transit to superconductor In was monitored during the temperature decreasing process.

We noticed the T$_C$ for indium is not exact 3.4 K, this may due to indium exposed in small value

Figure C.3: FRIB β = 0.041 quarter wave resonators (QWRs), β = 0.085 QWRs, β = 0.29 half wave resonators HWRs and β = 0.53 HWRs. Both QWRs have bottom flanges that sealed with indium wire.

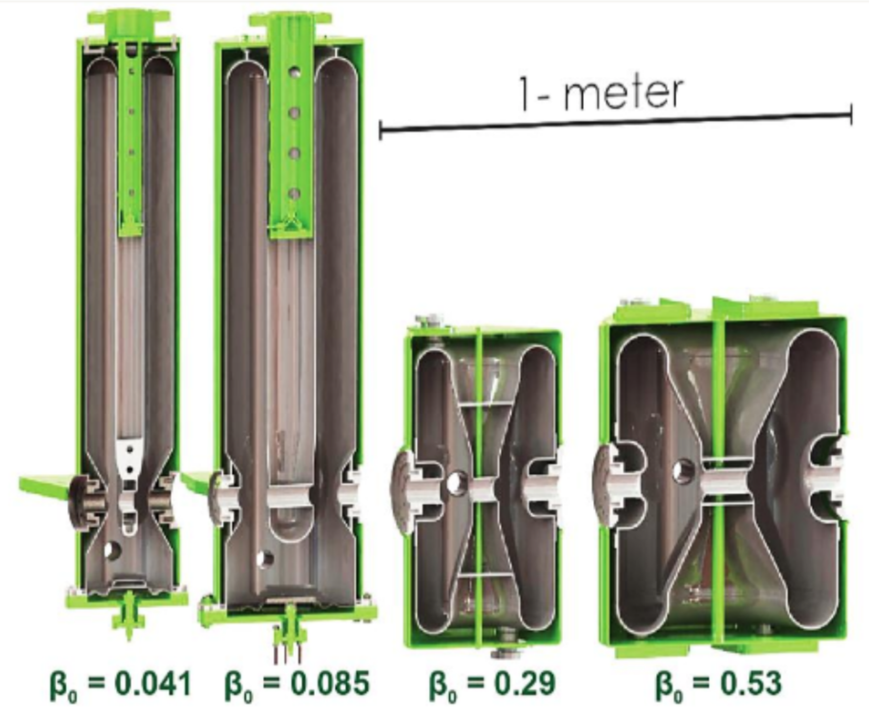

of magnetic field. Based on T$_C$ = 3.4 K, H$_C$(0) = 0.03 T, transit point at 1/T = 0.31 K^{-1} and T$_C$ relation with H$_C$(0):

$$H_C(T) \cong H_C(0) \cdot [1 - (\frac{T}{T_C})^2], \tag{C.1}$$

we can get $H_C(T) \cong 0.1\ H_C(0) \cong 3 \times 10^{-3}$ T.

On the meantime, the Nb is always superconductor during the whole test. This indicate that we can have two BCS superconductor equations for the cavity: for T > 3.4 K, In is normal conductor, and the resistance does not change with temperature, so the equation is:

$$R_S = R_0 + A_{Nb}\frac{\omega^2}{T}exp(-\frac{\Delta(0)_{Nb}}{k_B T}). \tag{C.2}$$

The R$_0$ includes the residue resistance of superconducting Nb and In normalconducting resistance. while for T ≤ 3.4, both In and Nb are superconductors, so the equation becomes:

$$R_S = R'_0 + A_{Nb}\frac{\omega^2}{T}exp(-\frac{\Delta(0)_{Nb}}{k_B T}) + A_{In}\frac{\omega^2}{T}exp(-\frac{\Delta(0)_{In}}{k_B T}), \tag{C.3}$$

where $\Delta(0)_{Nb}/k_B$ = 19.28 K, and $\Delta(0)_{In}/k_B$ = 6.19 K, and this R_0' includes both residue resistance for superconducting Nb and In. We can adopt these two equations, applying BCS fitting for the result data, and get some information that related to the low field Q drop problem.

C.2 BCS Fitting

We first separate the result data by the transit point,plot two graphs and do BCS fitting for the T > 3.4 K part (Fig. C.4, left), with the equation: m1+m2*exp(-19.28*x)*x (Eq.C.2, 1/T as x), and get m1 = 5.835, which is the R_0 in nΩ and m2 = 1237.7 is the $A_{Nb}\omega^2$ in Eq.C.2. In this case,

$$R_0 = R_{In,NC} + R_{Nb,res},$$

where $R_{In,NC}$ is the normal conducting resistance and $R_{Nb,res}$ is the Nb residue resistance, both resistances do not change with temperature.

Then we do Niobium and Indium BCS fitting for T < 3.4 K (Fig. C.4, right). Use the value we got for $A_{Nb}\omega^2$ = 1237.7 from the first fitting, we use the equation: m1'+1237.7 *exp(-19.28*x)*x+m2'*exp(-6.19*x)*x (Eq.C.3, 1/T as x) we get m1' = 3.776, which is the the R_0 in $n\Omega$ and m2' = 43.18 is $A_{In}\omega^2$ in Eq.C.3. In this case,

$$R_0' = R_{In,res} + R_{Nb,res} = R_{Cav,res},$$

is the sum of f both Nb and In's superconducting residue resistance. Compare with Eq. C.2 and Eq. C.2, we can get

$$R_0 - R_0' = R_{In,NC} - R_{In,res},$$

this agrees with the fact that the two part of graph is separated with indium T_C.

C.3 Statistic Result

During studying this low field Q drop issue of β = 0.085 QWRs, Dr. Zheng in cryomodule department found that some simple re-toque of the bottom flange can solve this problem. Thus we compare the before and after re-toque data of some QWRs, and get the average value shown in Tab. C.1.

Figure C.4: R_S Vs. 1/T for an example $\beta = 0.085$ QWR. Separate BCS fitting was done for T > 3.4 K (left figure) and T < 3.4 K (right figure) and the fitting result parameters are shown in the boxes on the figures.

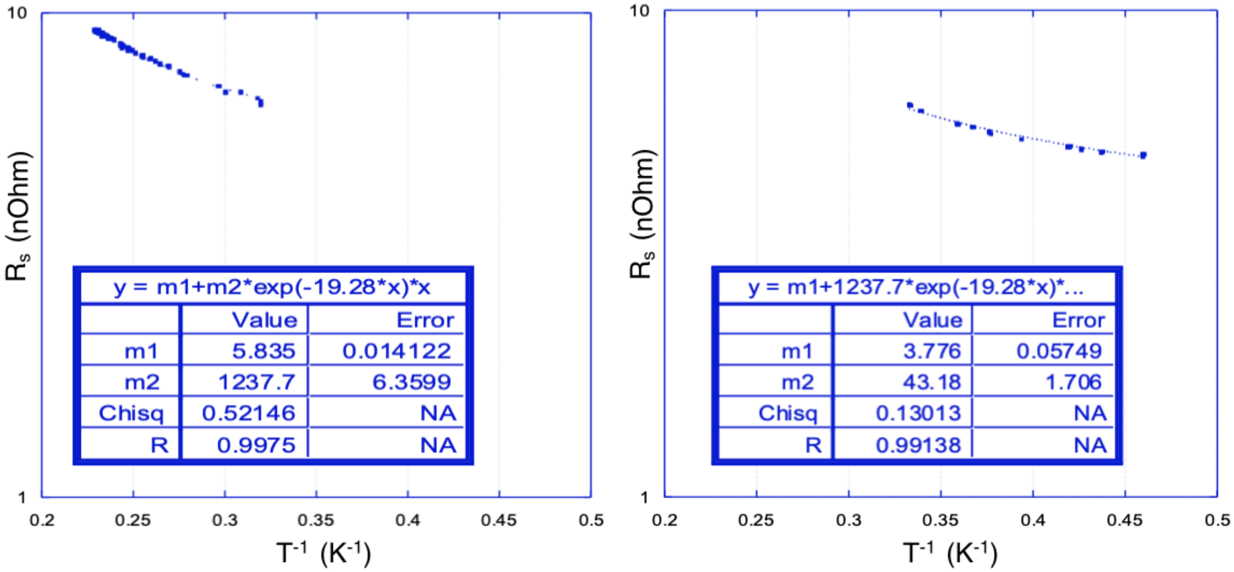

Table C.1: BCS fitting average result for 10 QWRs before Re-Toque and 10 QWRs after Re-Toque in FRIB. The $R_{res,cav}$ and $R_{In,NC}$- $R_{In,res}$ are from fitting, while $R_{In,2K}$ is directly from averaging the test data.

Cavity Status	$R_{res,cav}$	$R_{In,NC}$- $R_{In,res}$	$R_{In,2K}$
Before Re-Toque	4.75 $n\Omega$	2.13 $n\Omega$	0.95 $n\Omega$
After Re-Toque	2.83 $n\Omega$	1.98 $n\Omega$	0.84 $n\Omega$
Decrease	40.52%	7.20%	11.38%

The residue resistance of the cavity is dropped by 40.52% after the re-toque, which is much higher improvement than the other two parameters. Here “residue” means it does not change with temperature. The residual resistance is temperature independent and is related to many causes: surface imperfections and inclusions, residual dc magnetic field, condensed gases, etc...

C.4 Conclusion

Through statistical analysis of all the data of QWR vertical test, data fitting with BCS principle, it is found that the main reason for this phenomenon is that the residual resistance of indium wire used for sealing is too high in 2K superconductive state. The extra resistance may due to the oxide layer, re-toque process pressed the indium wire more, and breaks the oxide layer. This assumption agree with the fact that $\beta = 0.085$ QWRs have more serious Q drop, this is because the bottom flange of them are heavier than the $\beta = 0.085$ QWRs, so the gap between the cavity and bottom flange is larger, and indium wire has more un-broken oxide layer.

BIBLIOGRAPHY

BIBLIOGRAPHY

[1] *Nobel lectures*, Vol. Chemistry 1901-1921 (Elsevier Publishing Company, Amsterdam, 1966).

[2] J. D. Cockcroft and E. T. S. Walton, “Experiments with high velocity positive ions.(i) further developments in the method of obtaining high velocity positive ions”, in Proceedings of the royal society a, Vol. 136 (1932), pp. 619–630.

[3] R. J. van de Graaff, K. T. Compton, and L. C. van Atta, “The Electrostatic Production of High Voltage for Nuclear Investigations”, Physical Review **43**, 149–157 (1933).

[4] J. Xie, *Accelerators and technological innovation (chinese edition)*, edited by Y. Lu (Tsinghua University Press; Jinan University Press, Dec. 2000).

[5] G. Ising, “Prinzip einer methode zur herstellung von kanalstrahlen hoher voltzahl”, In: Arkiv för Matematik, Astronomi och Fysik., 1-4 **18** (1924).

[6] R. Wideröe, “Über ein neues prinzip zur herstellung hoher spannungen”, Archiv für Elektrotechnik **21**, 387–406 (1928).

[7] E. O. Lawrence and M. S. Livingston, “The production of high speed light ions without the use of high voltages”, Phys. Rev. **40**, 19–35 (1932).

[8] V. I. Veksler, “A new method of acceleration of relativistic particles”, Journal of physics **9**, 153–158 (1945).

[9] E. M. McMillan, “The synchrotron—a proposed high energy particle accelerator”, Phys. Rev. **68**, 143–144 (1945).

[10] T. P. Wangler, “Rf linear accelerators”, in, 2nd ed., Print ISBN:9783527406807 |Online ISBN:9783527623426 |DOI:10.1002/9783527623426 (John Wiley Sons, Ltd, Jan. 2010) Chap. 1, p. 11.

[11] V. Veksler, D. Efremov, A. Mints, M. Veisbein, F. Vodopyanov, M. Gashev, A. Zeidlits, P. Ivanov, A. Kolomensky, I. Malyshev, N. Monoszon, I. Nevyazhsky, V. Petukhov, M. Rabinovich, S. Rubchinsky, K. Sinelnikov, and A. Stolov, “The 10-gev proton synchrotron of the ussr academy of sciences”, Journal of Nuclear Energy (1954) **4**, 333–339 (1957).

[12] J. Chen, *Accelerator physics foundation(chinese edition)* (Peking University Press, Jan. 2000).

[13] D. W. Kerst and R. Serber, “Electronic orbits in the induction accelerator”, Phys. Rev. **60**, 53–58 (1941).

[14] E. D. Courant, M. S. Livingston, and H. S. Snyder, “The strong-focusing synchroton—a new high energy accelerator”, Phys. Rev. **88**, 1190–1196 (1952).

[15] W. Barletta, “Fundamentals of accelerator physics and technology with simulations and measurements lab”, in (U.S. Particle Accelerator School course materials, University of New Mexico, Albuquerque, NM 87131, USA, June 2009) Chap. Unit 11 - Lecture 18: Synchrotron Radiation - I.

[16] E. Cartlidge, “European xfel to shine as brightest, fastest x-ray source”, Science **354**, 22–23 (2016).

[17] $Lcls_{i}i|linaccoherentlightsource.$

[18] A. Abada, M. Abbrescia, S. S. AbdusSalam, I. Abdyukhanov, J. Abelleira Fernandez, A. Abramov, M. Aburaia, A. O. Acar, P. R. Adzic, P. Agrawal, J. A. Aguilar-Saavedra, J. J. Aguilera-Verdugo, M. Aiba, I. Aichinger, G. Aielli, A. Akay, A. Akhundov, H. Aksakal, J. L. Albacete, S. Albergo, A. Alekou, M. Aleksa, R. Aleksan, R. M. Alemany Fernandez, Y. Alexahin, R. G. Alıa, S. Alioli, N. Alipour Tehrani, B. C. Allanach, P. P. Allport, M. Altınlı, W. Altmannshofer, G. Ambrosio, D. Amorim, O. Amstutz, L. Anderlini, A. Andreazza, M. Andreini, A. Andriatis, C. Andris, A. Andronic, M. Angelucci, F. Antinori, S. A. Antipov, M. Antonelli, M. Antonello, P. Antonioli, S. Antusch, F. Anulli, L. Apolinário, G. Apollinari, A. Apollonio, D. Appelö, R. B. Appleby, A. Apyan, A. Apyan, A. Arbey, A. Arbuzov, G. Arduini, V. Arı, S. Arias, N. Armesto, R. Arnaldi, S. A. Arsenyev, M. Arzeo, S. Asai, E. Aslanides, R. W. Aßmann, D. Astapovych, M. Atanasov, S. Atieh, D. Attié, B. Auchmann, A. Audurier, S. Aull, S. Aumon, S. Aune, F. Avino, G. Avrillaud, G. Aydın, A. Azatov, G. Azuelos, P. Azzi, O. Azzolini, P. Azzurri, N. Bacchetta, E. Bacchiocchi, H. Bachacou, Y. W. Baek, V. Baglin, Y. Bai, S. Baird, M. J. Baker, M. J. Baldwin, A. H. Ball, A. Ballarino, S. Banerjee, D. P. Barber, D. Barducci, P. Barjhoux, D. Barna, G. G. Barnaföldi, M. J. Barnes, A. Barr, J. Barranco Garcıa, J. Barreiro Guimarães da Costa, W. Bartmann, V. Baryshevsky, E. Barzi, S. A. Bass, A. Bastianin, B. Baudouy, F. Bauer, M. Bauer, T. Baumgartner, I. Bautista-Guzmán, C. Bayındır, F. Beaudette, F. Bedeschi, M. Béguin, I. Bellafont, L. Bellagamba, N. Bellegarde, E. Belli, E. Bellingeri, F. Bellini, G. Bellomo, S. Belomestnykh, G. Bencivenni, M. Benedikt, G. Bernardi, J. Bernardi, C. Bernet, J. M. Bernhardt, C. Bernini, C. Berriaud, A. Bertarelli, S. Bertolucci, M. I. Besana, M. Besançon, O. Beznosov, P. Bhat, C. Bhat, M. E. Biagini, J. .-L. Biarrotte, A. Bibet Chevalier, E. R. Bielert, M. Biglietti, G. M. Bilei, B. Bilki, C. Biscari, F. Bishara, O. R. Blanco-Garcıa, F. R. Blánquez, F. Blekman, A. Blondel, J. Blümlein, T. Boccali, R. Boels, S. A. Bogacz, A. Bogomyagkov, O. Boine-Frankenheim, M. J. Boland, S. Bologna, O. Bolukbasi, M. Bomben, S. Bondarenko, M. Bonvini, E. Boos, B. Bordini, F. Bordry, G. Borghello, L. Borgonovi, S. Borowka, D. Bortoletto, D. Boscherini, M. Boscolo, S. Boselli, R. R. Bosley, F. Bossu, C. Botta, L. Bottura, R. Boughezal, D. Boutin, G. Bovone, I. BožovićJelisavić, A. Bozbey, C. Bozzi, D. Bozzini, V. Braccini, S. Braibant-Giacomelli, J. Bramante, P.

Braun-Munzinger, J. A. Briffa, D. Britzger, S. J. Brodsky, J. J. Brooke, R. Bruce, P. Brückman De Renstrom, E. Bruna, O. Brüning, O. Brunner, K. Brunner, P. Bruzzone, X. Buffat, E. Bulyak, F. Burkart, H. Burkhardt, J. .-P. Burnet, F. Butin, D. Buttazzo, A. Butterworth, M. Caccia, Y. Cai, B. Caiffi, V. Cairo, O. Cakir, R. Calaga, S. Calatroni, G. Calderini, G. Calderola, A. Caliskan, D. Calvet, M. Calviani, J. M. Camalich, P. Camarri, M. Campanelli, T. Camporesi, A. C. Canbay, A. Canepa, E. Cantergiani, D. Cantore-Cavalli, M. Capeans, R. Cardarelli, U. Cardella, A. Cardini, C. M. Carloni Calame, F. Carra, S. Carra, A. Carvalho, S. Casalbuoni, J. Casas, M. Cascella, P. Castelnovo, G. Castorina, G. Catalano, V. Cavasinni, E. Cazzato, E. Cennini, A. Cerri, F. Cerutti, J. Cervantes, I. Chaikovska, J. Chakrabortty, M. Chala, M. Chamizo-Llatas, H. Chanal, D. Chanal, S. Chance, A. Chancé, P. Charitos, J. Charles, T. K. Charles, S. Chattopadhyay, R. Chehab, S. V. Chekanov, N. Chen, A. Chernoded, V. Chetvertkova, L. Chevalier, G. Chiarelli, G. Chiarello, M. Chiesa, P. Chiggiato, J. T. Childers, A. Chmielińska, A. Cholakian, P. Chomaz, M. Chorowski, W. Chou, M. Chrzaszcz, E. Chyhyrynets, G. Cibinetto, A. K. Ciftci, R. Ciftci, R. Cimino, M. Ciuchini, P. J. Clark, Y. Coadou, M. Cobal, A. Coccaro, J. Cogan, E. Cogneras, F. Collamati, C. Colldelram, P. Collier, J. Collot, R. Contino, F. Conventi, and C. T. A. Cook, "He-lhc: the high-energy large hadron collider", The European Physical Journal Special Topics **228**, 1109–1382 (2019).

[19] M. S. Livingston, "High-energy accelerators", in ((New York: Interscience), 1954), p 151.

[20] T. Plettner, R. L. Byer, and R. H. Siemann, "The impact of einstein's theory of special relativity on particle accelerators", Journal of Physics B: Atomic, Molecular and Optical Physics **38**, S741–S752 (2005).

[21] K. Saito, "Ion accelerator technology lecture notes", 2017.

[22] H. Padamsee, "Applications and operations", in *Rf superconductivity: science, technology, and applications* (WILEY-VCH Verlag GmbH Co. KGaA, 2009) Chap. 11, p. 335.

[23] M. Kelly, "Overview of tem-class super- conducting cavities for proton and ion acceleration", in Proceedings of linac 2006, MO3002 (2006), p. 23.

[24] A. P. Banford and G. H. Stafford, "The feasibility of a superconducting proton linear accelerator", Journal of Nuclear Energy. Part C, Plasma Physics, Accelerators, Thermonuclear Research **3**, 287–290 (1961).

[25] H. Padamsee, "50 years of superconducting rf", in The roots of the lhc technology: cern centennial superconductivity symposium (2011).

[26] R. H. Pantell, G. Soncini, and H. E. Puthoff, "Stimulated photon-electron scattering", IEEE Journal of Quantum Electronics **QE 4**, 905–907 (1968).

[27] J. Madey, *Stimulated emission of radiation in periodically deflected electron beam*, 1974.

[28] J. M. Madey and H. A. Schwettman, "Free electron laser. final report 15 jul–8 oct 76", (1976).

[29] A. Butterworth, P. Brown, O. Brunner, E. Ciapala, H. Frischholz, G. Geschonke, E. Peschardt, and J. Sladen, "The lep2 superconducting rf system", Nuclear Inst Methods in Physics Research A **587**, 151–177 (2008).

[30] S. Noguchi, "Experience on the superconducting rf system in tristan", Part Accel **54** (1996).

[31] B. Dwersteg, A. Matheisen, W. D. Moller, D. Proch, D. Renken, and J. Sekutowicz, "Operating experience with superconducting cavities in the hera e-ring", Part Accel **54**, 301–314 (1996).

[32] L. S. Cardman, L. Harwood, and T. Jefferson, "The jlab 12 gev energy upgrade of cebaf for qcd and hadronic physics", in Ieee particle accelerator conference (2008).

[33] R. D. Mckeown, "The jefferson lab 12 gev upgrade", Journal of Physics Conference **312** (2011).

[34] J. D. Fuerst, K. W. Shepard, M. P. Kelly, S. M. Gerbick, and G. P. Zinkann, "Progress on cavity fabrication for the atlas energy upgrade", in Proceedings of 13th workshop on rf superconductivity, TUP75 (2007).

[35] *Argonne tandem linac accelerator system.*

[36] J. Wei, "The Very High Intensity Future", in Proceedings, 5th International Particle Accelerator Conference (IPAC 2014), Dresden, Germany, June 15-20, 2014 (2014), MOYBA01.

[37] J. Wei et al., "Advances of the FRIB project", Int. J. Mod. Phys. **E28**, 1930003 (2019).

[38] C. Wrede, "The facility for rare isotope beams", EPJ Web of Conferences **93**, 07001 (2015).

[39] W. Hartung, W. Chang, S.-H. Kim, D. Norton, J. Popielarski, J. Schwartz, K. Saito, C. Zhang, and T. Xu, "Performance of frib production quarter-wave and half-wave resonators in dewar certification tests", in 19th int. conf. on rf superconductivity, THP061 (2019).

[40] S. Calatroni, *Srf tutorial – part i*, indico.cern.ch/event/471931/contributions/, Europe/Zurich, Jan. 2016.

[41] M. Kelly, Rev. Accel. Sci. Technol. **5**, 185 (2012).

[42] Jackson and JohnDavid, *Classical electrodynamics. /-2d ed* (Wiley, 1975).

[43] S. Guo, *Classical electrodynamics. (chinese edition)* (Higher Education Press, 2008).

[44] C. Xie and K. Rao, *Electomagnetic fields and wave (chinese edition)* (Higher Education Press, 1999).

[45] H. Padamsee, J. Knobloch, and T. Hays, “Electrodynamics of normal and superconductors”, in (WILEY-VCH Verlag GmbH Co. KGaA, 2008) Chap. 4.

[46] P. K. Dirk van Delft, “The discovery of superconductivity”, Physics Today **63**, 38 (2010).

[47] W. Meissner and R. Ochsenfeld, “Ein neuer effekt bei eintritt der supraleitfähigkeit”, Naturwissenschaften **21**, 787–788 (1933).

[48] Y. Zhang, *Superconducting physics (chinese edition)* (University of Science and Technology of China Press, 1997).

[49] W. H. Keesom and A. V. Itterbeek, Proc. Amst **34**, 996 (1931).

[50] C. J. Gorter, “Theory of supraconductivity”, Nature **132**, 931–931 (1933).

[51] C. J. Gorter and H. Casimir, Phys. A **1**, 306 (1934).

[52] Y. J. Jo, J. Zhou, and Z. H. Sung, “Specific heat of nb3sn: the case for a single gap”, APL Materials **2** (2014).

[53] W. H. Keesom and J. D. Smedt, “Sur la diffraction des rayons x par des liquides (deuxième communication)”, Journal De Physique Et Le Radium **5**, 126–128 (1924).

[54] M. Wilkinson, N. Gingrich, and C. Shull, “The magnetic structure of mn2sb”, Journal of Physics and Chemistry of Solids **2**, 289–300 (1957).

[55] T. Mamyia, A. Oota, and Y. Masuda, “Thermal conductivity of superconducting niobium”, Solid State Communications **15**, 1689 (1974).

[56] K. Kraft, PhD thesis (Cornell University, 1983).

[57] K. Fossheim, “Alexei a. abrikosov: the magnetic structure of type ii superconductors”, Superconductivity Discoveries Discoverers (2013).

[58] A. A. Abrikosov, “Type ii superconductors and the vortex lattice”, Chemphyschem **5**, 924–929 (2004).

[59] W. B. Richardson, A. L. Pardhanani, G. F. Carey, and A. Ardelea, “Numerical effects in the simulation of ginzburg–landau models for superconductivity”, International Journal for Numerical Methods in Engineering **59**, 1251–1272 (2004).

[60] V. L. Ginzburg, “On superconductivity and superfluidity (what i have and have not managed to do), as well as on the ’physical minimum’ at the beginning of the 21 st century.”, Chemphyschem **76**, 930–945 (2004).

[61] L. D. Landau and E. M. Lifshitz, “Course of theoretical physics”, Fluid Mechanics **6** (1959).

[62] H. Padamsee, J. Knobloch, and T. Hays, “Superconductivity essentials”, in (WILEY-VCH Verlag GmbH Co. KGaA, 2008) Chap. 3, p. 71.

[63] C. D. Giorgio, D. D’Agostino, A. M. Cucolo, M. Iavarone, A. Scarfato, G. Karapetrov, S. A. Moore, M. Polichetti, D. Mancusi, S. Pace, V. Novosad, V. Yefremenko, and F. Bobba, “Superconducting vortex‚äêantivortex pairs: nucleation and confinement in magnetically coupled superconductor‚äêferromagnet hybrids”, in *Vortex dynamics and optical vortices*, edited by H. Perez-de-Tejada (IntechOpen, Rijeka, 2017) Chap. 3.

[64] W. S. Corak and C. B. Satterthwaite, “Atomic heats of normal and superconducting tin between 1.2° and 4.5°k”, Phys Rev **102**, 662–666 (1956).

[65] P. L. Richards and M. Tinkham, “Far-infrared energy gap measurements in bulk superconducting in, sn, hg, ta, v, pb, and nb”, Physical Review **119**, 575–590 (1960).

[66] Maxwell and Emanuel, “Isotope effect in the superconductivity of mercury”, Physical Review **78**, 477–477 (1950).

[67] Fr$\ddot{o}$hlich and H., “Theory of the superconducting state. i. the ground state at the absolute zero of temperature”, **79**, 845–856 (1950).

[68] D. C. Mattis and J. Bardeen, “Theory of the anomalous skin effect in normal and superconducting metals”, Physical Review **111**, 412–417 (1958).

[69] H. Padamsee, J. Knobloch, and T. Hays, “Maximum surface fields”, in (WILEY-VCH Verlag GmbH Co. KGaA, 2008) Chap. 5.

[70] S. Belomestnykh and A. Romanenko, “Uspas course: rf superconductivity for particle accelerators”, June 2017.

[71] K. Saito, “Ion accelerator technology lecture notes 17 slide 39”, Clean Technologies for SRF Cavities, Hydrogen Cure, and High gradient, 2017.

[72] K. Saito, “Development of electropolishing technology for superconducting cavities”, in Proceedings of the 2003 particle accelerator conference (KEK, 2003).

[73] K. Saito, “Q-drop at high gradient, pro- spect of higher q for cw, critical rf sc field”, in Proceedings of 11th workshop on rf superconductivity, THWG1 (2003).

[74] B. Visentin, “Low, medium, high field q-slopes change with surface treatments”, in Proceedings of the workshop on pushing the limits of rf superconductivity (CEA-Saclay, 2005), pp. 94–105.

[75] K. Saito, “Surface smoothness for high gradient niobium sc rf cavities”, in Proceedings of the 11th workshop on rf superconductivity, thp15 (KEK, 2003).

[76] K. Saito, “Cavity performance from frib”, in Ttc meeting at riken (June 2018).

[77] K. Saito, H. Inoue, E. Kako, T. Fujino, S. Noguchi, M. Ono, and T. Shishido, “Superiority of electropolishing over chemical polishing on high gradients”, in Proceedings of the 1997 workshop on rf superconductivity (KEK, 1997).

[78] L. Lilje, D. Reschke, K. Twarowski, P. Schmüser, D. Bloess, E. Haebel, E. Chiaveri, J.-M. Tessier, H. Preis, H. Wenninger, H. Safa, and J.-P. Charrier, “Electropolishing and in-situ baking of 1.3 ghz niobium cavities”, in Proceedings of the 1999 workshop on rf superconductivity (1999).

[79] K. Saito, E. Kako, T. Shishido, S. Noguchi, M. Ono, and Y. Yamazaki, “Long term air exposure effect on the electropolished surface of niobium superconducting rf cavity”, in Proceedings of the 1999 workshop on rf superconductivity, tup030 (1999).

[80] G. Ciovati, “Review of the frontier workshop and q-slope results”, in Proceedings of the 12th international workshop on rf superconductivity (TJNAF, 2005).

[81] H. Safa, “High field behavior of scrf cavities”, in The 10th workshop on rf superconductivity, ma008 (2001).

[82] G. Ciovati, “Effect of low-temperature baking on the radio-frequency properties of niobium superconducting cavities for particle accelerators”, Journal of Applied Physics **96**, 1591–1600 (2004).

[83] Halbritter and J., “Rf residual losses, surface impedance, and granularity in superconducting cuprates”, Journal of Applied Physics **68**, 6315–6326 (1990).

[84] S. Bousson, M. Fouaidy, T. Junquera, N. Hammoudi, and J. Lesrel, “Kapitza conductance and thermal conductivity of materials used for srf cavities fabrication”, Journal of Materials in Civil Engineering **16**, 8–14.

[85] R. Flaminio, J. Franc, C. Michel, N. Morgado, and B. Sassolas, “A study of coating mechanical and optical losses in view of reducing mirror thermal noise in gravitational wave detectors”, Classical Quantum Gravity **27**, 84030–84038(9) (2009).

[86] L. Cifarelli and L. Maritato, “Superconducting materials for high energy colliders: proceedings of the 38th workshop of the infn eloisatron project”, in Proceedings of the 38th workshop of the infn eloisatron project (2001), p. 74.

[87] K. Saito and P. Kneisel, “Temperature dependence of the surface resistance of niobium at 1300 mhz - comparison to bcs theory”, in Proceedings of the 1999 workshop on rf superconductivity, tup031 (1999).

[88] J. Knobloch, R. L. Geng, M. Liepey, and H. Padamsee, “High-field q slope in superconducting cavities due to magnetic field enhancement at grain boundaries”, in Proceedings of the 1999 workshop on rf superconductivity, tua004 (1999).

[89] C. Xu, M. J. Kelley, and C. E. Reece, “Analysis of high field non-linear losses on srf surfaces due to specific topographic roughness”, in Proceedings of ipac2012, WEEPPB011 (2012).

[90] J. Halbritter, “Degradation of superconcucting rf cavity performances by extrinsic properties”, in Proceedings of the 11th workshop on rf superconductivity (2003).

[91] A. Romanenko, G. Wu, L. D. Cooley, and G. Ciovati, “Post-baking losses in electropolished niobium cavities: cutout studies”, in Proceedings of srf2011, THPO008 (2011).

[92] C. Benvenuti, S. Calatroni, I. Campisi, P. Darriulat, C. Durand, M. Peck, R. Russo, and A.-M. Valente, “Magnetic flux trapping in superconducting niobium”, in Proceedings of the 1997 workshop on rf superconductivity, srf97b05 (1997).

[93] H. Padamsee, “High-field q-slope and quench field”, in *Rf superconductivity: science, technology, and applications* (WILEY-VCH Verlag GmbH Co. KGaA, 2009) Chap. 5, p. 129.

[94] K. Saito.

[95] H. Padamsee, J. Knobloch, and T. Hays, “Cavity fabrication and preparation”, in *Rf superconductivity for accelerators* (WILEY-VCH Verlag GmbH Co. KGaA, 2008) Chap. 6, p. 108.

[96] Z. G. Zong, J. Gao, J. Zhai, Q. J. Xu, L. Liu, L. Zhang, K. Saito, and F. Furuta, “Performance comparison of the single-cell large grain cavities treated by ep and cp”, in Proceedings of pac09 (IHEP, 2009).

[97] W. Singer, “Status of the single cell cavity r&d at desy”, in Ttc meeting at fnal (Apr. 2007).

[98] F. Furuta, “High gradient behaviors of large grain ichiro single cell cavity by chemical polishing”, in Proceedings of ipac’10, WEPE004 (2010).

[99] G. Eremeev and H. Padamsee, "A comparison of large grain and fine grain cavities using thermometry", in Proceedings of epac 2006, MOPCH176 (2006).

[100] P. Kneisel, G. Myneni, G. Ciovati, J. Sekutowicz, and T. Carneiro, "Preliminary results from single crystal and very large crystal niobium cavities", in Proceedings of 2005 particle accelerator conference (TJNAF, 2005).

[101] P. Kneisel, G. Myneni, G. Ciovati, J. Sekutowicz, and T. Carneiroo, "Performance of large grain and single crystal niobium cavities", in Proceedings of the 12th international workshop on rf superconductivity (Jefferson Lab, 2005).

[102] W. Singer, "Experiences with multi-cell large grain superconducting rf cavities", in Ttc meeting at fnal (Apr. 2007).

[103] G. R. Myneni, "Recent progress lg/sc nb", in Ttc meeting at fnal (Jefferson Lab, Apr. 2007).

[104] *Mit course: thermodynamics and kinetics of materials lecture 3*, 2006.

[105] W. Gerhard, R. Boyer, and E. Collings, *Materials properties handbook: titanium alloys* (ASM International, 1993).

[106] K. Saito, "Ion accelerator technology lecture notes 18 slide 16", Performance degradation-free coldmass assembly and advanced cavity fabrication technologies for cost reduction, 2017.

[107] H. Kitamura, Y. Kijima, Y. Murai, K. Saito, E. Kako, T. Shishido, M. Ono, and S. Noguchi, "Effect of n2 gas exposure on the l-band superconducting cavity", in Proceedings of the 1999 workshop on rf superconductivity, tup034 (1999).

[108] T. Higuchi, "Development of hydrogen-free ep and hydrogen absorption phenomena", PhD thesis (The Graduate University for Advanced Studies, 2002).

[109] A. Grassellino, "New breakthroughs and future directions in srf technology research", in Ipac 2017 (2017).

[110] A. Grassellino, A. Romanenko, Y. Trenikhina, M. Checchin, M. Martinello, O. Melnychuk, S. Chandrasekaran, D. Sergatskov, S. Posen, A. Crawford, et al., "Unprecedented quality factors at accelerating gradients up to 45 mvm- 1 in niobium superconducting resonators via low temperature nitrogen infusion", Superconductor Science and Technology **30**, 094004 (2017).

[111] T. Higuchi, "Development of hydrogen-free ep and hydrogen absorption phenomena", in Proceedings of the 11th workshop on rf superconductivity (Nomura Plating Co., 2003).

[112] A. D. Palczewski, C. E. Reece, M. Kelley, and J. Tuggle, “Investigation of nitrogen absorption and nitride growth on srf cavity grade rrr niobium as a function of furnace temperature”, in Proceedings of linac2016, THOP02 (2016).

[113] K. Saito, “Ion accelerator technology lecture notes 16 slide 17”, SRF Surface Preparation Technologies, 2017.

[114] J. Tuggle, A. Palczewski, C. Reece, F. Stevie, and M. Kelley, “Investigation of low-level nitrogen in niobium by secondary ion mass spectrometry”, in Proceedings of linac2016 (Virginia Polytechnic Institute and State University, 2016).

[115] A. Romanenko, “Breakthrough technology for very high quality factors in srf cavities”, in Proceedings of linac2014, TUIOC02 (2014).

[116] R. Wedenig, T. Niinikoski, P. Berglund, J. Kyynäräinena, and I. Suni, “Superconducting nbn microstrip detectors rd 39 collaboration”, in (1999).

[117] D. Bloess, “Chemistry and surface treatment”, in Proceedings of srf workshop 1984, SRF84-23 (1984).

[118] C. Antoine, A. Aspart, J. P. Charrier, H. Safa, and B. Visentin, “Alternative approaches for surface treatment of nb superconducting cavities”, in Proceedings of the 1999 workshop on rf superconductivity, tup031 (1999).

[119] Wikipedia contributors, *Surface roughness — Wikipedia, the free encyclopedia*, [Online; accessed 13-May-2019], 2019.

[120] K. Suzuki, M. Kajino, K. Ogawa, T. Asano, M. Ogino, H. Aihara, F. Shimizu, M. Onishi, and Y. Suzuki, *Brightening chemical polishing solution for hardened steel article*, 1993.

[121] K. Suzuki, M. Kajino, K. Ogawa, T. Asano, M. Ogino, H. Aihara, F. Shimizu, M. Onishi, and Y. Suzuki, “Brightening chemical polishing solution for hardened steel article and method of chemically polishing said article in the solution”, (1995).

[122] P. Shigolev, *Electrolytic and chemical polishing of metals*, edited by D. Gong, 1st ed. (Science Press, 1961).

[123] R. Erdmann, “Über chemisches polieren”, Metalloberfläche **5**, B4–B6 (1953).

[124] R. Lattey and H. Neunzig, “Entwicklungen auf dem gebiet des chemischen glänzens von aluminium”, Metalloberfläche **9**, A97–A103 (1955).

[125] H. Fischer and L. Koch, “Oberflächenabtragung beim chemischen und anodischen polieren von aluminium”, Metall **6**, 491–496 (1952).

[126] H. Spähn, “Das chemische polieren”, Metalloberfläche **5**, B17–B26 (1953).

[127] X. Guo, X. Xiao, X. Yi, and P. Zhong, “Study on chemical polishing and passivation of copper and copper alloy”, Surface Technology **30**, 000035–39 (2001).

[128] J. Klausner, G. Throncroft, and R. Mei, “Bubble forces and detachment models”, Multiphase Science and Technology **13**, 35–76 (2001).

[129] M. Lebon, J. Sebilleau, and C. Colin, “Dynamics of growth and detachment of an isolated bubble on an inclined surface”, Phys. Rev. Fluids **3**, 073602 (2018).

[130] A. Villari et al., “On the Acceleration of Rare Isotope Beams in the Reaccelerator (ReA3) at the National Superconducting Cyclotron Laboratory at MSU”, in Proc. of linear accelerator conference (linac’16), east lansing, mi, usa, 25-30 september 2016, Linear Accelerator Conference 28, https://doi.org/10.18429/JACoW-LINAC2016-TUOP04 (May 2017), pp. 390–393.

[131] Z. Zheng, J. Popielarski, K. Saito, and T. Xu, “Cost Reduction for FRIB Magnetic Shielding”, in Proc. of linear accelerator conference (linac’16), east lansing, mi, usa, 25-30 september 2016, Linear Accelerator Conference 28, https://doi.org/10.18429/JACoW-LINAC2016-THPRC023 (May 2017), pp. 818–820.

[132] K. Saito, N. Bultman, E. Burkhardt, F. Casagrande, S. Chandrasekaran, S. Chouhan, C. Compton, J. C. K. Elliott, and A. Facco, “Superconducting rf development for frib at msu”, in Proceedings of linac2014, THIOA02 (2014).